Investigation of Near-bed Transport Dynamics of Microplastics in Open-channel Flows

by

Zijian Yu

A thesis submitted in partial fulfillment of the requirements for the degree of

Doctor of Philosophy

in

Water Resources Engineering

Department of Civil and Environmental Engineering
University of Alberta

Abstract

Microplastics (MPs), defined as plastic particles smaller than 5 mm, are widespread in aquatic environments. However, their transport mechanisms in flow remain underexplored despite being critical for understanding their environmental transport and fate. This thesis addresses this gap by investigating near-bed MP transport processes, from initial transport stages (settling and incipient motion) to ongoing transport dynamics (continuous and intermittent movements).

For MP settling, no generalized formula exists for the drag coefficient (C_d) that accounts for variations in MP physical properties (shape, size, and density). In this thesis, 1,343 MP settling data were collected from the literature. A new equation for C_d was developed using the dimensionless particle diameter (d_*) and two shape descriptors, yielding an absolute error of 15.2%, significantly lower than that of existing equations (42.5-72.8%).

The incipient motion threshold of MPs was next examined. MPs can either be exposed to flow, making them more prone to movement, or shielded by bed particles, requiring higher flow conditions for mobilization. For exposed MPs, the effects of bed roughness and MP properties on the critical shear stress (τ_c) were experimentally investigated. A new explicit equation for the critical movability number (Λ_c) was proposed, incorporating d^* and a new dimensionless parameter related to MP physical properties, resulting in a smaller absolute error (12.3%) compared to a previous equation (55.6%). For hidden MPs, a power law relationship was identified between τ_c and the density and size of MPs, reducing error by 40% compared to a previous equation. To quantify sheltering effects, parameters for hiddenness (ΔZ), exposure (ΔH), and longitudinal exposure (ΔX) were introduced, leading to a semi-empirical method for predicting critical flow velocity (U_c), which reduced errors by 70% compared to previous methods for sediments.

MP transport can be continuous or intermittent, depending on the flow conditions relative to the incipient motion threshold. Using particle tracking velocimetry, this thesis explored both movement types, focusing on streamwise transport. For continuous movements, the streamwise velocity of MPs (v_x) follows a normal distribution. An empirical equation for v_x was proposed, resulting in a low relative error of 5.2% compared to the experimental data. The continuous MP movements are super-diffusive, with particle inertia identified as the primary source of this anomalous diffusion. For MP intermittent movements, streamwise hop length (L_x) and hop duration (T_{tr}) follow exponential distributions, and v_x exhibits a truncated Gaussian distribution. Approximately 60% of L_x corresponds to long hops, characterized by $L_x \propto T_{tr}$. By applying a Lagrangian framework to describe v_x and autocorrelation, it was shown that the preference for long hops is related to particle inertia, a fundamental characteristic of millimeter-sized MP transport.

Preface

This thesis is an original work by Zijian Yu under the supervision of Dr. William Wenming Zhang and Dr. Mark Loewen. It is presented in a paper format and consists of seven chapters.

Chapter 1 is a general introduction to the background, scope, and objectives of this study.

Chapters 2 to 6 are the main contents of this thesis.

Chapter 2 was published as:

- Yu, Z., Yang, G., & Zhang, W. (2022). A new model for the terminal settling velocity of microplastics. *Marine Pollution Bulletin*, *176*, 113449.

Chapter 3 was published as:

- Yu, Z., Yao, W., Loewen, M., Li, X., & Zhang, W. (2022). Incipient motion of exposed microplastics in an open-channel flow. *Environmental Science & Technology*, *56*(20), 14498-14506.

- Yu, Z., Yao, W., Loewen, M., Li, X., & Zhang W. (2023). Correction to "incipient motion of exposed microplastics in an open-channel flow". *Environmental Science & Technology*, *57*(51), 21927-21927.

Chapter 4 was published as:

- Yu, Z., Loewen, M., Guo, S., Guo, Z., & Zhang, W. (2023). An investigation of the sheltering effects on the mobilization of microplastics in open-channel flow. *Environmental Science & Technology*, *57*(30), 11259-11266.

Chapter 5 has been submitted as a journal manuscript:

- Yu, Z., Loewen, M., Zhou, Y., Guo, Z., Baki, A., & Zhang, W. (2024). Continuous Near-bed Movements of Microplastics in Open Channel Flows: Statistical Analysis. *Environmental Science & Technology*, Under Review.

Chapter 6 is currently being prepared as a journal manuscript.

Chapter 7 contains the general conclusions of this thesis, and provides suggestions for future research on this topic.

I was responsible for the experimental design, data collection, and analysis as well as the manuscript composition. Dr. William Wenming Zhang and Dr. Mark Loewen were the supervisory authors and were directly involved with the concept formation, data analysis, and manuscript composition.

I also have the following publications during my PhD:

- Yang, G., Yu, Z., Baki, A., Yao, W., Ross, M., Chi, W., & Zhang, W. (2023). Settling behaviors of microplastic disks in water. *Marine Pollution Bulletin*, *188*, 114657.

- Yu, Z., Loewen, M., & Zhang, W., Microplastic continuous motion: effects of hydrodynamic conditions and particle properties. The 3rd International Symposium on Sustainable Urban Drainage, Jiashan, Zhejiang, China, 19-22 October, 2023.

- Yu, Z. & Zhang, W. The statistical description of microplastic discontinuous motions in open channel flow. Proceedings of the 40th IAHR World Congress, Vienna, Austria, 21-25 August, 2023.

- Qian, S., Qiao, X., Zhang, W., Yu, Z., Dong, S., & Feng, J. (2024). Machine learning-based prediction for settling velocity of microplastics with various shapes. *Water Research*, *249*, 121001.

- Yang, G., Yu, Z., Peng, X., Zhou, Y., Baki, A., & Zhang, W. (2024). Settling behaviors of microplastic disks in acceleration fall. *Marine Pollution Bulletin*, *202*, 116296.

Existence is absurd.

Acknowledgments

I would like to express my deepest gratitude to my supervisor, Dr. Wenming Zhang, for providing me with the invaluable opportunity to pursue my doctoral degree. His unwavering support, guidance, and insightful advice have been instrumental throughout my research journey. Dr. Zhang's enthusiasm for research and thoughtful insights have been a constant source of inspiration. I am profoundly thankful for his patience and mentorship every step of the way.

I also extend my sincere thanks to my co-supervisor, Dr. Mark Loewen, for his invaluable contributions to my academic and personal growth. Dr. Loewen's dedication to research excellence and his deep understanding of the field have been immensely beneficial to my work. I am deeply grateful for his patience, mentorship, and the numerous discussions that have broadened my perspective and understanding.

Additionally, I am deeply appreciative of the financial support from the China Scholarship Council (CSC) and the Department of Civil and Environmental Engineering. Their funding was crucial in enabling me to pursue my PhD studies. I would like to extend a special thank you to Perry Fedun for his invaluable technical support in the laboratory setups. His dedicated assistance was essential for the smooth progression of my experiments.

Finally, my heartfelt gratitude goes to my parents for their unwavering support and encouragement, which provided me with the courage and motivation to persevere. I also want to express my love and appreciation to my girlfriend, Dr. Qin. Your love and support have been a pillar of strength for me.

Table of Contents

List of Tables

List of Figures

1. General introduction

1.1. Research background

Plastics entered the stage of industrial production in the mid-20th century (Bergmann et al., 2022). Since then, annual worldwide plastic production has surged, reaching over 400 megatonnes in 2019, and is expected to reach 500 megatonnes by 2025 (Sutkar et al., 2023; Vidal et al., 2024). This immense production, coupled with a recycling rate of only one-third, has resulted in significant global plastic pollution (Shen & Worrell, 2024).

A key aspect of plastic pollution is the breakdown of large plastic items into smaller fragments through various physical, chemical, and biological processes such as mechanical degradation, biodegradation, thermal actions, and photodegradation (Sutkar et al., 2023). These small plastic particles, typically less than 5 mm in size, are known as microplastics (MPs) (Wu et al., 2019). MPs have been identified as a significant environmental pollutant, making microplastic (MP) pollution a major global concern (Galloway et al., 2017).

Over the past decade, the threats posed by MPs in aquatic environments have become increasingly evident. For example, studies have documented their pervasive presence in various water bodies, from lakes to the remote Arctic Ocean, emphasizing the significant temporal and spatial scale of MP pollution (Bergmann et al., 2022; Nava et al., 2023; Yang et al., 2021; Zhang, 2017). Moreover, the detrimental effects of MPs on aquatic biota are concerning (Smith et al., 2018). Due to their small particle size, MPs can be easily ingested by marine filter feeders, leading to adverse physiological reactions such as blockages or mechanical damage to digestive organs (Botterell et al., 2019). Furthermore, the hydrophobic nature and large surface-to-volume ratio of MPs enable

them to carry, transfer, and accumulate harmful chemicals within the biological community and food web (Avio et al., 2015). These identified threats highlight the urgent need for effective strategies to mitigate and manage MP pollution in aquatic environments.

Most research on MPs in water bodies has primarily focused on their abundance, sampling techniques, biochemical consequences, and corresponding removal methods (Chubarenko et al., 2016; Van Melkebeke et al., 2020). However, this focus has overshadowed the study of MP transport processes in open channel flow. Open channel flow, which includes rivers and streams, is a major pathway for MPs, playing a critical role in their widespread distribution in aquatic environments (Mennekes & Nowack, 2023; Strokal et al., 2023). Gaining a deeper understanding of how MPs are transported in these flows is essential for developing predictive models of their temporal and spatial distribution, as well as for creating effective, site-specific removal strategies (Critchell & Lambrechts, 2016). Therefore, understanding the mechanisms and specific parameters that govern the transport and fate of MPs in open-channel flows is of both practical and significant importance.

The transport of MPs can involve particles that are buoyant ($\rho_p < 1$ g/cm^3), neutrally buoyant ($\rho_p \approx 1$ g/cm^3), and negatively buoyant MPs ($\rho_p > 1$ g/cm^3), depending on their density (ρ_p) relative to the surrounding fluid (ρ). Previous studies (Ballent et al., 2013; Ballent et al., 2012) have highlighted the need to investigate the transport mechanisms of negatively buoyant MPs. These negatively buoyant MPs tend to settle and accumulate in the beds of rivers, lakes, reservoirs, wetlands, and oceans (Schell et al., 2020; Yang et al., 2021). Once being mobilized, negatively buoyant MPs can contribute to widespread pollution. However, challenges in benthic sampling have limited studies on the abundance of negatively buoyant MPs, leading to an underestimation

of their presence and the importance of understanding near-bed transport mechanisms (Ballent et al., 2013). To date, research on the near-bed transport mechanisms of MPs remains limited.

The near-bed transport process of MPs could be conceptualized to include various representative transport behaviors, such as settling, initiation of mobilization, continuous movement, and intermittent movement with alternating states of resting and motion. Specifically, denser MPs may first experience a settling process and then be deposited on the beds of water bodies under weak hydrodynamic conditions. In a simplified scenario where a spherical MP particle settles in a static fluid, the particle reaches a state where gravity and buoyancy are balanced by the drag force. The settling velocity at this state, known as the terminal settling velocity, is a key parameter in characterizing the transport and fate of MPs in water bodies (Khatmullina & Isachenko, 2017).

Deposited MPs may be retained on the beds of water bodies, like riverbeds, which can serve as temporary or permanent sinks for MPs (Drummond et al., 2022). If the flow intensity exceeds a certain threshold, deposited MPs tend to initiate their mobilization, known as incipient motion (Bai et al., 2013). The concept of incipient motion is well-defined in sediment transport research and remains crucial in the study of MP transport. Investigating incipient motion in the context of MPs is essential for seeking answers to questions such as how long MPs tend to stay in one place and the conditions under which they begin to move. It is also worth noting that MPs vary in size and shape, as do bed materials. In some cases, MP particles are smaller than the bed particles and thus they are sheltered from the flow. In these situations, MPs are expected to require a higher flow threshold for their incipient motion. Therefore, investigating flow thresholds for MP incipient motion may require a clear distinction between cases where MPs are sheltered and those where MPs are more exposed.

After being mobilized, MPs begin their transport, exhibiting different behaviors depending on the flow intensity. At flow intensities near the threshold of incipient motion, MPs tend to move intermittently rather than continuously, alternating between periods of rest and motion (Campagnol et al., 2015). Under stronger hydrodynamic conditions, MPs move continuously. An investigation of continuous or intermittent movements of MPs is necessary for comprehending their transport mechanisms, including their diffusive behavior, initial deposition in streambeds, and predicting preferential accumulation zones.

1.2. Knowledge gaps, hypothesis, and research objectives

Several knowledge gaps related to the aforementioned representative transport behaviors of MPs have been identified, along with corresponding objectives. They include:

Gap 1: No generalized formula has been proposed for the drag coefficient and terminal settling velocity for MPs of different shapes and materials.

Objective 1: A reliable universal model to predict the drag coefficient and terminal settling velocity of MPs will be developed, based on an analysis of previous MP settling data collected from laboratory experiments and fieldwork.

Gap 2: The previous formula of dimensionless shear velocity for the incipient motions of exposed MPs does not consider the shapes of the MPs and it is only tested for PS, PA, PVC, and PET. Additionally, the critical incipient flow velocity for exposed MPs has not been reported.

Objective 2: The impact of MP properties on the critical flow velocity will be examined. Moreover, a new estimation method for the threshold of dimensionless shear stress will be developed, which will be valid for exposed MPs with various sizes, shapes, and densities.

Gap 3: Critical flow conditions for incipient motions of hidden MPs on rough beds have not been investigated.

Objective 3: A new empirical prediction method for the critical shear stress of hidden MPs will be proposed. Furthermore, a semi-empirical estimation method for the critical flow velocity will be introduced, where the sheltering effects will be described explicitly.

Gap 4: No studies have been reported on MP continuous movements yet.

Objective 4: A new prediction method for ensemble mean streamwise MP velocity will be proposed. Moreover, the potential impacts of MP properties and flow conditions on the variation of the standard deviation of MP velocity will be discussed. The diffusive regime during MP continuous movements will be identified.

Gap 5: No studies have been reported on intermittent movements of MPs.

Objective 5: The potential impacts of MP properties and flow conditions on key kinematic variables during MP intermittent movements, such as hop length, hop duration, and MP velocity, will be revealed.

1.3. Thesis outline

This thesis is organized into seven chapters and written as paper-based. Chapters 2-6 explore key aspects of near-bed MP transport, from the onset of the transport process including settling (Chapter 2) and incipient motion (Chapters 3 and 4) to their sustained behaviors including continuous (Chapter 5) and intermittent movements (Chapter 6). The detailed outline of this thesis is as follows:

Chapter 2 presents a literature review of existing formulas for predicting the terminal settling velocity of MPs. Based on the published MP settling data, a new explicit model is proposed for the drag coefficient and settling velocity.

Chapter 3 systematically investigates the effects of bed roughness and MP properties (shapes, sizes, and densities) on the critical flow velocity and shear velocity required to initiate the movement of exposed MPs through a series of flume experiments. A new estimation method for the critical shear velocity is proposed.

Chapter 4 addresses the challenges in predicting the mobilization threshold of MPs due to sheltering effects from bed materials. It proposes a new formula for the critical shear stress and develops a semi-empirical method for determining the critical flow velocity, incorporating explicit measures of sheltering effects.

Chapter 5 explores the near-bed transport characteristics of MPs in rough bed flows using particle tracking velocimetry. A revised empirical formula to estimate the ensemble mean streamwise MP velocity is proposed, and the diffusive regime associated with continuous MP movements is identified.

Chapter 6 examines the intermittent transport characteristics of MPs in open channel flows through a series of tracking experiments under flow conditions near the critical flow thresholds of MP mobilization. Key kinematic variables, such as MP velocity, hop length, and hop duration, are systematically investigated.

Chapter 7 provides general conclusions and briefly discusses future directions of research regarding the MP transport mechanism.

2. A new model for the terminal settling velocity of microplastics[1]

2.1. Introduction

Microplastic particles (MPs) cause marine and freshwater habitat deterioration (Acampora et al., 2016) and have drawn wide attention globally (Isachenko, 2020). Due to their small particle sizes (< 5 mm), MPs can be easily ingested by aquatic organisms and cause negative physiological reactions (Botterell et al., 2019). Moreover, harmful chemicals such as persistent organic pollutants or metals attached to the surface of MPs can be accumulated or transferred into the food chains (Avio et al., 2015). Most existing MP research focuses on the abundance, biological, and chemical consequences of MPs (Zhang, 2017), while the physical properties of MPs including hydrodynamic behaviors have been much less studied.

About half of plastics (and thus MPs) are denser than freshwater (Morét-Ferguson et al., 2010). The settling process is the main movement of negatively buoyant MPs, and the terminal settling velocity is a key parameter to characterize MP transport and fate in water bodies (Khatmullina & Isachenko, 2017). Laboratory experiments on MP settling (Ballent et al., 2012; Khatmullina & Isachenko, 2017; Kowalski et al., 2016) suggest that the sizes and shapes of MPs can affect the particle Reynolds number (Re_p) and the drag coefficient (C_d), and hence affect the particle terminal settling velocity. For instance, the proportion of settlement of MPs with a size of about 5 μm is low (18-25%) in rivers, indicating most of these MPs will be transported by rivers to downstream oceans; while millimeter-sized MPs are easy to deposit in rivers (Besseling et al., 2017). Studies have also shown that: the more irregular the MP shape or the smaller the particle size, the smaller

[1] The content of this chapter has been published as: Yu, Z., Yang, G., & Zhang, W. (2022). A new model for the terminal settling velocity of microplastics. *Marine Pollution Bulletin*, *176*, 113449.

the terminal settling velocity (Chubarenko et al., 2016; Khatmullina & Isachenko, 2017; Kowalski et al., 2016).

In natural water bodies, it is challenging to study the transport of MPs since they are not as visible as large, floating macro-plastics, which necessitates the development of a reliable settling model of MPs. To obtain the terminal settling velocity, the gravity and buoyancy acting on a particle falling in a still fluid must be balanced by the drag force, for which the drag coefficient (C_d) is important. Semi-empirical or empirical formulas on C_d have been proposed for MPs (Chubarenko et al., 2016; Khatmullina & Isachenko, 2017; Song et al., 2017). Given MPs and sediment particles are similar in geometry, studies have shown that the C_d formula for sediments might apply to MPs, but only to spherical and cylindrical MPs (Chubarenko et al., 2016; Khatmullina & Isachenko, 2017) due to the great differences in densities, sizes and shapes between MPs and sediments as well as among MPs. Thus, it is essential to further advance the knowledge of predicting C_d and terminal settling velocity for MPs of various shapes, sizes, and densities.

Formulas of C_d for non-MP, non-spherical particles have been developed, which lay the foundation for MPs. Yet, these formulas are valid only for certain shapes of particles, e.g., cylinder (Gabitto & Tsouris, 2008) and cube (Song et al., 2017), and are limited for particles of irregular shapes and different materials. In addition, existing studies introduced different shape factors to quantify the influence of particle shapes; however, there are no universal or widely accepted shape descriptors. For instance, shapes can be described as sphericity (Φ) (Hölzer & Sommerfeld, 2008), flatness index (Kowalski et al., 2016), or power roundness (Waldschläger & Schüttrumpf, 2019a). As a result, the results from different studies can be hardly compared. Representative shape descriptors need to be selected to generalize the effect of shapes on C_d and the terminal settling velocity for MPs.

To explore the above-mentioned knowledge gaps, a new and more reliable formula for predicting C_d was built in this study for MPs of different shapes (spherical and non-spherical), different materials, and settling in different ambient fluids. This formula was then used to build a model to better predict the terminal settling velocity of MPs. This study is useful to comprehend the transport and fate of MPs in aquatic environments.

2.2. Literature review

For a particle weighted m settling at a velocity of w_s in a static fluid, the movement can be expressed as follows:

$$m\frac{\mathrm{d}w_s}{\mathrm{d}t} = \frac{m}{\rho_p}\left(\rho_p - \rho_f\right)g - C_d A_p \rho_f \frac{w_s^2}{2} \tag{2-1}$$

where ρ_p and ρ_f are the densities of the particle and fluid, respectively; g is the gravitational acceleration; C_d is the drag coefficient; A_p is the projected area of the particle in the settling direction. When $\frac{\mathrm{d}w_s}{\mathrm{d}t} = 0$, the terminal settling velocity of the volume-equivalent sphere can be derived from Eq. (2-1) as:

$$w_s = \sqrt{\frac{4\left(\rho_p - \rho_f\right)g d_n}{3\rho_f C_d}} \tag{2-2}$$

where d_n ($= \sqrt[3]{6V/\pi}$) is the diameter of the volume equivalent sphere and V is the particle volume.

From Eq. (2-2), to predict w_s, the evaluation of C_d is essential. Previous studies (Brown & Lawler, 2003; Cheng, 2009; Clift & Gauvin, 1971; Haider & Levenspiel, 1989) established the relationships between C_d and the particle Reynolds number Re_p, where Re_p is defined as:

$$Re_p = \frac{\rho_f w_s d_n}{\mu} \tag{2-3}$$

where μ is the fluid dynamic viscosity. These $C_d \sim Re_p$ relationships and their application ranges are summarized in Table A-1 in Appendix A.

Clift and Gauvin (1971) proposed the drag law for C_d of spherical particles ($C_{d,s}$), which covers three regimes (laminar regime with $Re_p \leqslant 1$; transitional regime with $1 \leqslant Re_p < 10^3$; and turbulent regime with $10^3 \leqslant Re_p < 2\times10^5$):

$$C_{d,s} = \frac{24}{Re_p} + \frac{24}{Re_p}\left(0.15Re_p^{0.687}\right) + \frac{0.42}{1+\frac{42500}{Re_p^{1.16}}} \tag{2-4}$$

Song et al. (2008) proposed a quasi-theoretical model for C_d of sediment particles:

$$C_d = \left[\left(\frac{\sqrt{3}A}{2d_*^{3/2}}\right)^{2/n} + B^{1/n}\right]^n \tag{2-5}$$

where A (= 32.2), B (= 1.17), and n (= 1.75) are constants. d_* is the dimensionless particle diameter:

$$d_* = \left[\frac{\left(\rho_p - \rho_f\right)g}{\rho_f \nu^2}\right]^{1/3} d_n \tag{2-6}$$

where ν is the fluid kinematic viscosity. Chubarenko et al. (2016) showed that Eqs. (2-5) and (2-6) can be also applied for smooth spherical MPs. Within the same range of Re_p ($< 1 \sim 2\times10^5$) as Song et al. (2008), Cheng (2009) proposed a simple $C_d \sim d_*$ formula for spherical particles:

$$C_d = \frac{432}{d_*^3}\left(1+0.022d_*^3\right)^{0.54} + 0.47\left[1-\exp\left(-0.15d_*^{0.45}\right)\right] \quad (2\text{-}7)$$

which showed a better performance than other studies (Cheng, 1997; Guo, 2002; Ranieri, 2008).

Based on the studies on multiphase flow (Dellino et al., 2005; Haider & Levenspiel, 1989), it is known that for any given Re_p, the C_d values of irregular particles are greater than those of spherical particles. Therefore, to predict the terminal settling velocity of non-spherical particles, Chien (1994) introduced sphericity (Φ) to describe their difference compared to perfect spheres (Φ = 1). The sphericity is defined as A_{sph}/A_s, where A_s is the surface area of the real particle and $A_{sph} = 4\pi\left(d_n/2\right)^2$ is the surface area of the volume-equivalent sphere.

However, the sphericity Φ itself is difficult to represent highly irregular particles. For instance, a piece of MP fish line may share the same Φ value as an MP pellet, while they have different settling properties (Khatmullina & Isachenko, 2017). Previous studies introduced another shape descriptor to describe the effect of particle shapes together with Φ. For instance, for non-MP particles with high densities (2,680, 4,450, 7,960 kg/m^3), Song et al. (2017) introduced a dimensionless parameter (S) in their C_d formula:

$$C_d = \frac{500}{d_*^3\left(\phi^{0.98}S^{0.48}\right)}\left(1+0.017d_*^3\right)^{0.6} \quad (2\text{-}8)$$

where $S = S_e/S_p$, S_e is the surface area of the equivalent sphere and S_p is the projected area of the particle in the settling direction. The Corey's shape factor (*CSF*) is another commonly used shape descriptor for irregular, angular particles (Khatmullina & Isachenko, 2017). *CSF* is defined as

$c/(ab)^{1/2}$, where a, b, and c are the lengths of the longest, intermediate, and shortest sides of a particle, respectively. The range of CSF is 0 - 1, where 0 is for a disk and 1 is for a cube or a sphere.

Waldschläger and Schüttrumpf (2019a) proposed C_d expressions for MP pellets and fragments as well as for fibers:

$$\begin{cases} C_d(pellets\ \&\ fragments) = \left(\dfrac{3}{CSF\sqrt[3]{Re_p}} \right) \\ C_d(fibers) = \left(\dfrac{4.7}{\sqrt{Re_p}} + \sqrt{CSF} \right) \end{cases} \tag{2-9}$$

For calcareous sand particles with CSF = 0.11 to 0.98 and Re_p = 0.3 to 454.3, Alcerreca et al. (2012) proposed a $C_d \sim d_*$ relationship:

$$C_d = \frac{4}{3} \frac{d_*^3}{\left(\sqrt{22+1.13 d_*^2} - 4.67 \right)^3} \tag{2-10}$$

Moreover, formulas for directly calculating w_s of MPs without using C_d, have been reported (Francalanci et al., 2021; Wang et al., 2021). Francalanci et al. (2021) proposed a formula for predicting w_s of MPs characterized by different shapes:

$$w_s = \frac{a^{1.5} CSF^{0.68} b^{0.5} \dfrac{\rho_p - \rho_f}{\rho_f} \dfrac{g}{v}}{18 a^{-0.38} \left(\dfrac{a^2+b^2+c^2}{3} \right)^{0.19} + \left(0.2781 CSF^{-0.1602} d_g^{\,3} \dfrac{\rho_s - \rho_f}{\rho_f} \dfrac{g}{v^2} \right)^{0.4942 CSF^{-0.059}}} \tag{2-11}$$

where $d_g = (CSF)^{0.34}(ab)^{0.5}$. Eq. (2-11) can be applied to all regimes of Re_p. Wang et al. (2021) proposed a model that predicts w_s of MPs based on the shape, density, and particle size as well as fluid density:

$$w_s = 1.0434\left(\frac{\rho_p - \rho_f}{\rho_f} g\right)^{0.495} \frac{d_n^{0.777} CSF^{0.710}}{v^{0.124}} \quad (2\text{-}12)$$

Eq. (2-12) is valid for MPs with shapes like a near-sphere or polygonal ellipsoid. Fragmented and fiber-shaped MPs were not considered in their experiment.

2.3. Methodology

2.3.1. Data collection

All the available laboratory experimental data (1,343) on MP terminal settling velocity reported in the literature from 2016 to 2021 were collected as raw data for this study. Nine types of MP materials have been reported, with $(\rho_p - \rho_f)/\rho_f$ = 0.02 - 0.56. The reported MPs have various shapes (cylinder, disk, pellet, fiber, fragment, and film) with wide ranges of *CSF* (0.01 -1.00) and Φ (0.06 -1.00). Table A-2 in Appendix A provides a detailed summary of these raw data.

From the original dataset, 644 data points were filtered out (see Table A-2), with 699 data points remaining for developing the new C_d formula and the terminal settling velocity model in this study. The filtering was mainly because these data points did not provide or have enough information to calculate the shape descriptors (Φ and *CSF*) of MPs. After the filtering, the Φ and *CSF* values ranged from 0.01 to 1.00, and Re_p ranged from 1 to 300, covering the majority range of Re_p of existing MP studies.

The C_d values were not directly provided in two of the collected studies (Khatmullina & Isachenko, 2017; Kowalski et al., 2016). From the measured data of w_s, it is possible to calculate the experimental values of C_d via rearranging Eq. (2-2):

$$C_d = \frac{4gd_n\left(\rho_s - \rho_f\right)}{3\rho_f w_s^2} \tag{2-13}$$

2.3.2. Terminal settling velocity model

Eq. (2-9) contains the implicit relationship between C_d and the terminal settling velocity (w_s) of MPs because Re_p is a function of w_s [Eq. (2-3)]. To solve for w_s, an iteration procedure is required (see Figure A-1 in Appendix A for the iteration process), and this type of model is the so-called implicit model (Song et al., 2017). Due to the much lower efficiency of using implicit models (Cheng, 2009; Song et al., 2017), an explicit model was proposed in this study to compute w_s by using the $C_d \sim d_*$ relationship.

According to Dioguardi and Mele (2015), for spherical particles, $C_dRe_p^2$ was calculated by combing Eqs. (2-2), (2-3), and (2-13):

$$C_d Re_p^{\ 2} = \frac{4gd_n^3\rho_f\left(\rho_p - \rho_f\right)}{3\mu^2} \tag{2-14}$$

From Eq. (2-14), $C_dRe_p^2$ is independent of w_s. To apply Eq. (2-14) to non-spherical MP particles, particle shapes need to be considered. Dioguardi and Mele (2015) found that $C_dRe_p^2/C_{d,s}$ and Re_p have a power-law relationship, with the consideration of sphericity (Φ):

$$Re_p = m\left(\frac{C_d}{C_{d,s}} Re_p^{\,2} \phi^{Re_p^{\,l}}\right)^n \tag{2-15}$$

where m, l, and n are constants.

Previous studies (Cheng, 2009; Song et al., 2017) have shown that C_d can also be expressed as a function of d_* and varies with d_* in a similar pattern as the C_d - Re_p relationship. With this consideration, Eq. (2-15) can be expressed in the form of $C_d = function\ (d_*, C_{d,s}, \Phi)$. Following this form and introducing the other shape descriptor CSF, the new drag law for spherical and non-spherical MPs was proposed:

$$C_d = \frac{C_{d,s}}{(d_*^{\beta_1} \phi^{d_*^{\beta_2}} CSF^{d_*^{\beta_3}})^{\beta_4}} \tag{2-16}$$

where β_1, β_2, β_3, and β_4 are constants obtained by fitting with the experimental data of MPs collected from the literature. The numerator, $C_{d,s}$, in Eq. (2-16) can be calculated directly from Eq. (2-7).

With C_d computed from Eq. (2-16) for a given d_*, w_s can be obtained from the following equation (Cheng, 2009; Francalanci et al., 2021; Song et al., 2017).

$$w_s = \left(\upsilon g \frac{\rho_s - \rho_f}{\rho_f}\right)^{1/3} \sqrt{\frac{4d_*}{3C_d}} \tag{2-17}$$

2.3.3. Model performance evaluation

The dataset of the calculated $C_{d,calc}$ was compared with that of measured ones, $C_{d,meas}$, by using the absolute value of relative error ($\left| Err\ \% \right|$):

$$|Err\%| = \frac{\sum_{i=1}^{N} \frac{\left|C_{d,calc,i} - C_{d,meas,i}\right|}{C_{d,meas,i}}}{N} \times 100 \tag{2-18}$$

and by using the root-mean-square error (*RMSE*):

$$RMSE = \sqrt{\frac{\sum_{i=1}^{N} \left(\frac{C_{d,calc,i} - C_{d,meas,i}}{C_{d,meas,i}}\right)^2}{N}} \times 100 \tag{2-19}$$

where N is the number of the total data points.

To assess the prediction ability on the terminal settling velocity of the explicit model, $|Err\ \%|$ and *RMSE* were calculated similarly from the measured values ($w_{s,meas}$) and the calculated ones ($w_{s,calc}$).

2.4. Results and discussion

2.4.1. Impact and significance of MP shapes on C_d

The majority of the existing MP data are in the transitional regime ($1 \leq Re_p < 10^3$), as shown in Figure 2-1. Comparison between the experimental $C_d \sim Re_p$ for MPs and the formulas for spherical particles [Eqs. (2-4), (2-5), and (2-7)] suggest that the formulas significantly underestimate (by up to 95%) C_d values for 95 % of the irregular MPs in the transitional regime. For the turbulent regime ($10^3 < Re_p < 10^5$), the limited data points shown in the figure were from spherical MPs, and therefore they agree well with the drag law. The root cause for the poor prediction of the spherical drag law is the formulas do not take particle shapes and densities into account, which can be dominant factors for MP settling in the transitional regime (Saxby et al., 2018).

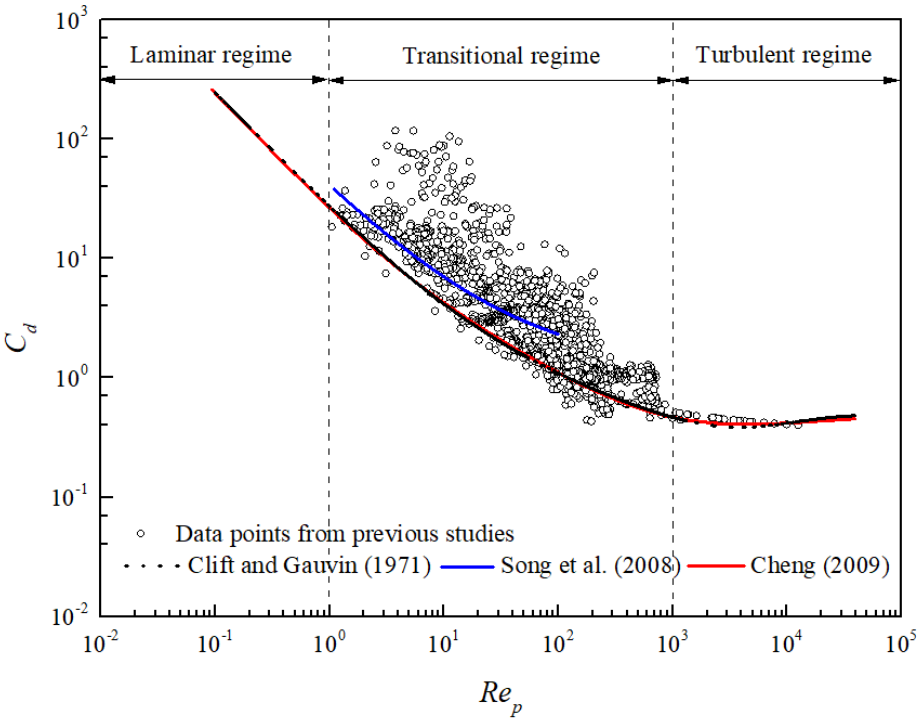

Figure 2-1 Comparison of C_d versus Re_p for MPs of different shapes and types (densities), against the drag laws for spherical particles of Clift and Gauvin (1971), Song et al. (2008), and Cheng (2009). The dots represent all the data points of MPs collected from the seven studies listed in Table A-2.

To illustrate the shape effect of MPs on C_d, the experimental data in water bodies of different salinities are compiled in Figure 2-2 for various MP sphericities (Φ). The experimental data points fall into distinct groups according to their sphericities. For comparison purposes, each group was fitted by linear regression ($R^2 > 0.75$ for 90% of cases). It is clear that MPs with larger sphericity (closer to spherical shape) have lower C_d for the same Re_p. For example, Figure 2-2 (a) shows that in the transitional regime, for the same Re_p, the C_d value of pellets (Φ =1) is smaller than that of particles with Φ = 0.36. Similar observations have been reported for other particles, e.g., volcanic ashes (Saxby et al., 2018) and pumices (Dellino et al., 2005). Figure 2-2 also shows that for MPs with the same Re_p and Φ, the impact of different salinities on the C_d value of MPs is limited (see

Figure A-2 in Appendix A), despite that the impact on the w_s value cannot be ignored (Kowalski et al., 2016).

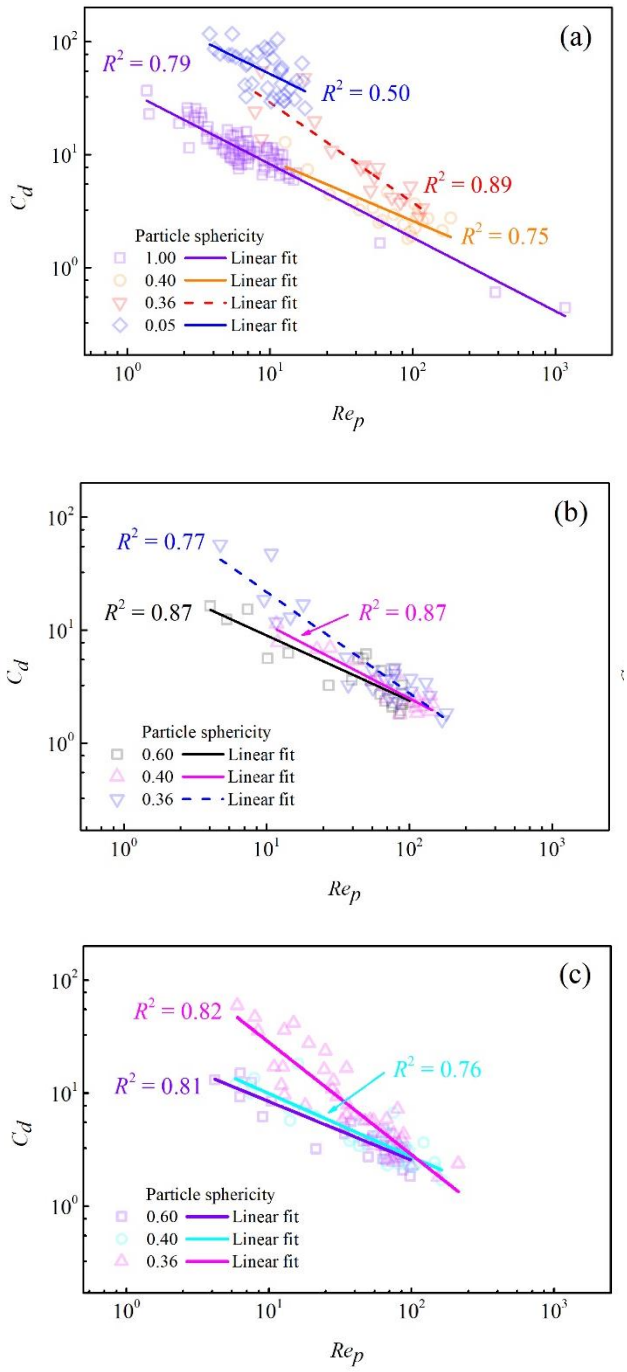

Figure 2-2 Impact of particle sphericity on the C_d versus Re_p relationship for MPs in ambient fluids with the salinities of (a) 0 ppt (parts per thousand), (b) 15 ppt, and (c) 36 ppt. The colored dots are the data from the seven studies listed in Table A-2 (Appendix A). The colored lines represent the best linear fits of each group of MPs categorized by sphericities.

Similarly, to examine the impact of the other important shape descriptor *CSF*, all the collected data points of C_d versus Re_p are grouped as per *CSF* values in Figure 2-3. Generally, it demonstrates a clear, negative relationship between *CSF* and C_d for the same Re_p. For instance, for Re_p = 10, C_d decreases from 14.57 to 6.75 as *CSF* increases from 0.36 to 1.00. This is attributed to that a larger *CSF* value typically means a smaller cross-sectional area perpendicular to the transport path and a weaker flow separation, leading to a decrease in C_d value.

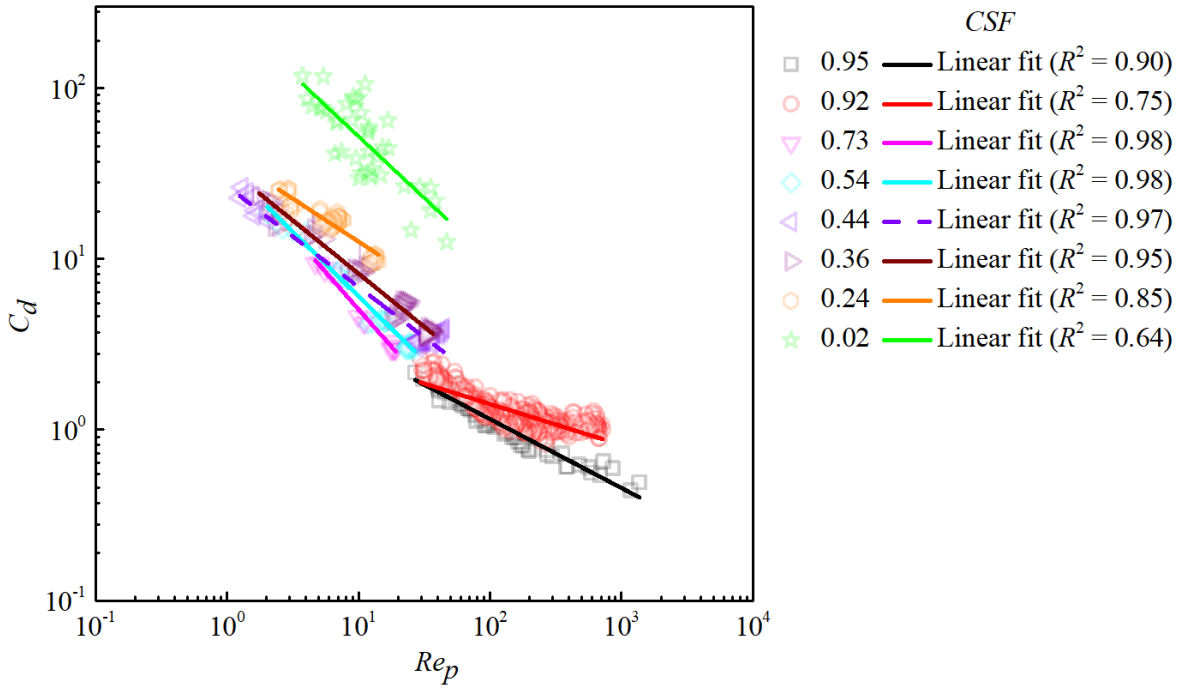

Figure 2-3 Impact of particle *CSF* on the C_d versus Re_p relationship for MPs with Re_p = 1 - 10^3. The colored lines represent the best fitted linear line for each group of MPs.

To analyze the significance of the influencing factors of Φ and *CSF*, the relationship of $C_dRe_p^2$ ~ Re_p was plotted (see Figure A-3 in Appendix A). The $C_dRe_p^2$ ~ Re_p relationship is expected to be linear for sediments and pumices (Dellino et al., 2005; Dioguardi & Mele, 2015; Zhu et al., 2017). Figure A-3 shows that the data points of MPs are well fitted by a linear line, and the correlation

coefficient R^2 is high (0.86). Note that the regression covers all the 1,343 raw data points (Table A-2 in Appendix A).

Through linear regression, statistics indicators including the *P*-value and variance inflation factor (*VIF*), were obtained from SPSS Statistics 22.0 and are listed in Table A-3 in Appendix A. *VIF* quantifies the variances degree of how the predictors are inflated and the strength of correlation between the predictors. If $VIF > 5$ (Akinwande et al., 2015), two or more predictors are correlated (multicollinearity) and at least one of them is redundant. To reduce the collinearity, one or more predictors should be eliminated. In this study, for Φ and *CSF*, the *P*-values are both < 0.05 and the *VIF* values are both < 5 (Table A-3 in Appendix A), indicating that each predictor has a great significance in the $C_dRe_p^2 \sim Re_p$ relationship and both variables should be considered. Hence, *CSF* and Φ can describe the shapes of MPs from different aspects.

2.4.2. Performance of the new C_d formula for MPs

The fitted values of β_1, β_2, β_3, and β_4 in the new C_d formula [Eq. (2-16)] and their 95% confidential intervals are given in Table 2-1. The formula has a good performance in predicting C_d and the adjusted coefficient of determination, R^2, is 0.93. The accuracies of the new C_d formula and existing C_d formulas for non-spherical particles (Alcerreca et al., 2013; Chubarenko et al., 2016; Song et al., 2017; Song et al., 2008; Waldschläger & Schüttrumpf, 2019a) are compared in Table 2-2. The new formula has $|Err\%| = 15.2\%$ and $RMSE = 17.3\%$ against the experimental data, both of which are much lower compared to the existing formulas that have $|Err\%| = 42.5 - 72.8\%$ and $RMSE = 49.0 - 105.8\%$. This demonstrates the advantage of the new C_d formula, compared to the existing formulas.

Table 2-1 Fitted values for β_1 - β_4 and their lower and upper 95% confidence intervals for the new C_d formula

Parameter	Value	Lower 95% confidence interval	Upper 95% confidence interval
β_1	-0.25	-0.36	-0.13
β_2	0.03	-0.34	0.40
β_3	0.33	0.16	0.49
β_4	0.25	0.12	0.37

Table 2-2 Accuracies of the existing and new C_d formulas against the experimental data

Formula	Eq. of C_d	$\|Err\ \%\|$	*RMSE* (%)
Song et al. (2008) & Chubarenko et al. (2016)	(2-5)	48.3	52.9
Alcerreca et al. (2012)	(2-10)	42.5	49.0
Song et al. (2017)	(2-8)	54.5	105.8
Waldschlager & Schüttrumpf (2019a)	(2-9)	72.8	74.2
This study	(2-16)	15.2	17.3

For further comparison, the values of $\left|Err\%\right|$ and *RMSE* of all the formulas are plotted in Figure 2-4 specifically for MPs grouped by materials and shapes. The new C_d formula has the lowest values of $\left|Err\%\right|$ and *RMSE* in almost all (11 out of 12) the groups of MPs, and low values for one group (PS pellet). This suggests the wider application range of the new C_d formula for different MP materials and shapes, compared to the other four existing formulas.

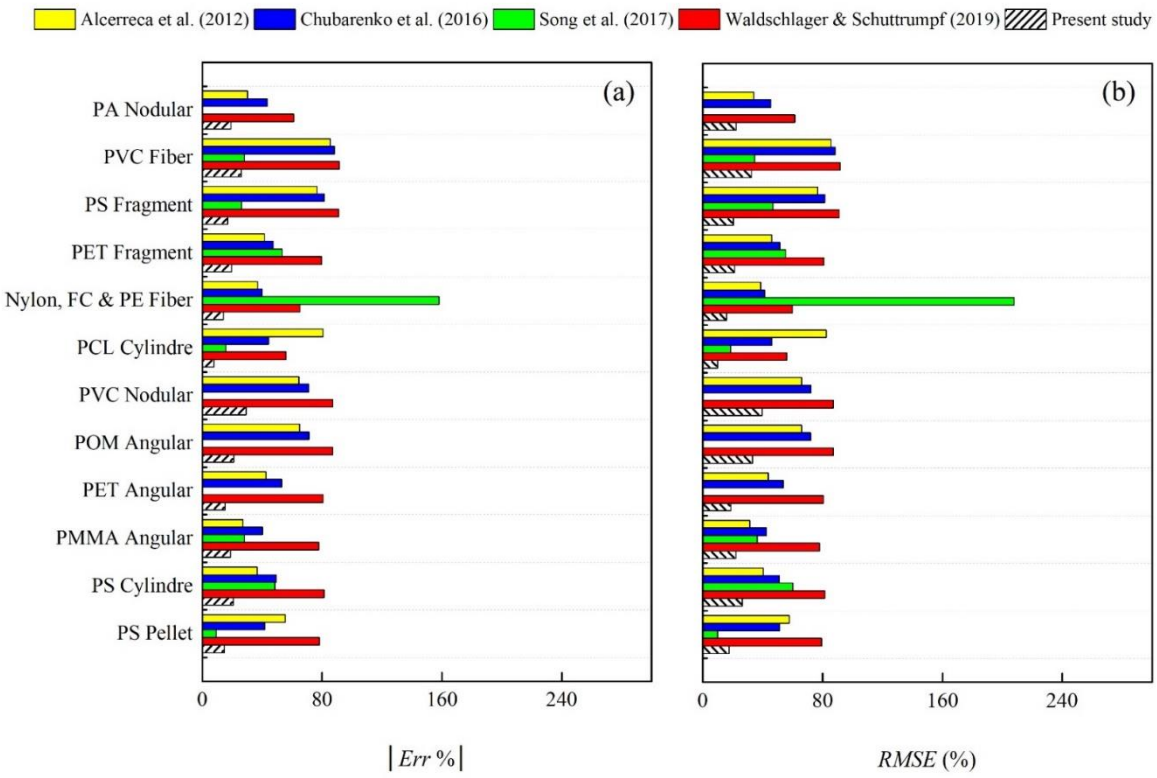

Figure 2-4 Absolute relative error ($|Err\%|$) and root-mean-square error (*RMSE*) of C_d for MPs of different materials and shapes. The comparisons were made against the experimental C_d values from the studies listed in Table A-2. PA - polyamide; PVC - polyvinyl chloride; PS - polystyrene; PET - polyethylene terephthalate; FC – fluorocarbon; PE –polyethylene; PCL - polycaprolactone; POM – polyoxymethylene; PMMA – polymethyl methacrylate.

Despite the new formula having the lowest error levels, the C_d value predicted from Eq. (2-16) still fluctuates at around 15% ($|Err\%| = 15.2\%$). Possible reasons include instrumental error, measurement error, and uncertainties that cannot be avoided in any laboratory experiment. Another possible reason is that given the fact that 30% of the data are for highly irregular MPs such as fish lines and fibers (Khatmullina & Isachenko, 2017; Van Melkebeke et al., 2020), their secondary movements including rotation or tumbling (Khatmullina & Isachenko, 2017) could affect their falling trajectory and thus increase the variations of w_s and C_d.

The new C_d formula suggests that both Φ and CSF are important, and they cover each other's deficiency in describing the shapes of MPs. Previous studies also proposed other shape descriptors such as X (circularity), Ψ (the ratio between Φ and X) (Dellino et al., 2005; Dioguardi & Mele, 2015; Dioguardi et al., 2018), S (Song et al., 2017), Cailleux's Flatness Index ($=\frac{a+b}{2c}$) or Krumbein's Sphericity Index ($=\left(\frac{bc}{a^2}\right)^{1/3}$) (Kowalski et al., 2016). These descriptors are not included in the new C_d formula, because each of them is suitable for particles with specific characteristics, e.g., X is suitable for particles with sharp corners (Wang et al., 2018). Moreover, some shape descriptors, like Cailleux's Flatness Index and Ψ, could be obtained indirectly from CSF and Φ with different approximations (Dioguardi et al., 2018). Hence, for future research related to MP shapes, both CSF and Φ are suggested to be used for comparison among different studies.

2.4.3. Performance of the terminal settling velocity model for MPs

The present terminal settling velocity (w_s) model is based on the new C_d formula, Eq. (2-16), and the explicit equation of w_s, Eq. (2-17). The modeling results ($w_{s,calc}$) are plotted against the experimental data ($w_{s,meas}$) in Figure 2-5, together with three existing explicit models for w_s (Francalanci et al., 2021; Song et al., 2017; Wang et al., 2021) for comparison purpose. The present model (Figure 2-5d) has a better prediction on w_s than the other three models (Figure 2-5a-c), because the value of the correlation coefficient R^2 is the highest (0.99). Moreover, the fitted line of the $w_{s,calc} \sim w_{s,meas}$ relationship has a slope of 1.01, which is closer to 1.00 compared to those (0.79-1.50) from the other three models. Furthermore, the data scatteredness is small in the present model. Song et al. (2017)'s model also has a good performance (Figure 2-5a), but the range of w_s is only limited to 0 - 6 cm/s and the data points are much smaller (only 315 vs. 699 in Figure 2-5d), mainly because of the limited application range of Φ and Re_p in that model.

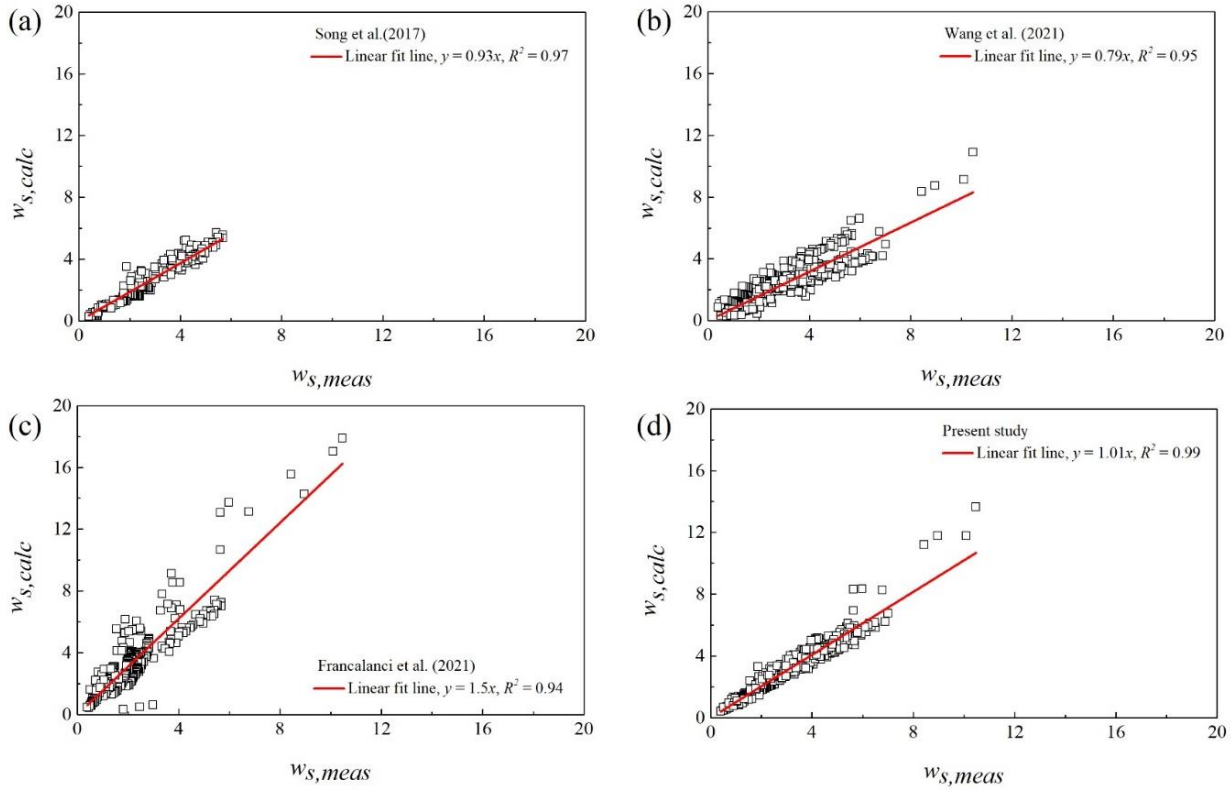

Figure 2-5 Plot of $w_{s,meas}$ obtained from experimental data versus $w_{s,calc}$ calculated from the models of (a) Song et al. (2017); (b) Wang et al. (2021); (c) Francalanci et al. (2021); and (d) this study.

The comparison results of $|Err\%|$ and *RMSE* for all the models are summarized in Table 2-3. The present w_s model offers the best fit to the experimental measurement data, with the lowest $|Err\%|$ = 8.8% and *RMSE* = 11.4%. For the other three models, $|Err\%|$ ranges from 15.4% to 77.2%, and *RMSE* ranges from 21.0% to 84.9%.

Table 2-3 Accuracies of the existing and proposed models for predicting the terminal settling velocity (w_s) against the experimental data

Model	**Eq. of w_s**	**$\|Err$ %$\|$**	***RMSE* (%)**
Song et al. (2017)	(2-8) & (2-17)	15.4	21.0
Wang et al. (2021)	(2-12)	20.1	28.3
Francalanci et al. (2021)	(2-11)	77.2	84.9
This study	(2-16) & (2-17)	8.8	11.4

Figure 2-6 further compares all the w_s models for MPs grouped by materials and shapes. The present model has the lowest values of $|Err\%|$ and *RMSE* for almost all (10 out of 12) the groups of MPs, and low values for the remaining two groups (PS pellet and PS fragment for $|Err\%|$; PS pellet and PVC nodular for *RMSE*). Thus, it can be concluded that the present w_s model can predict well the terminal settling velocity for MPs of different materials and shapes in the transitional regime.

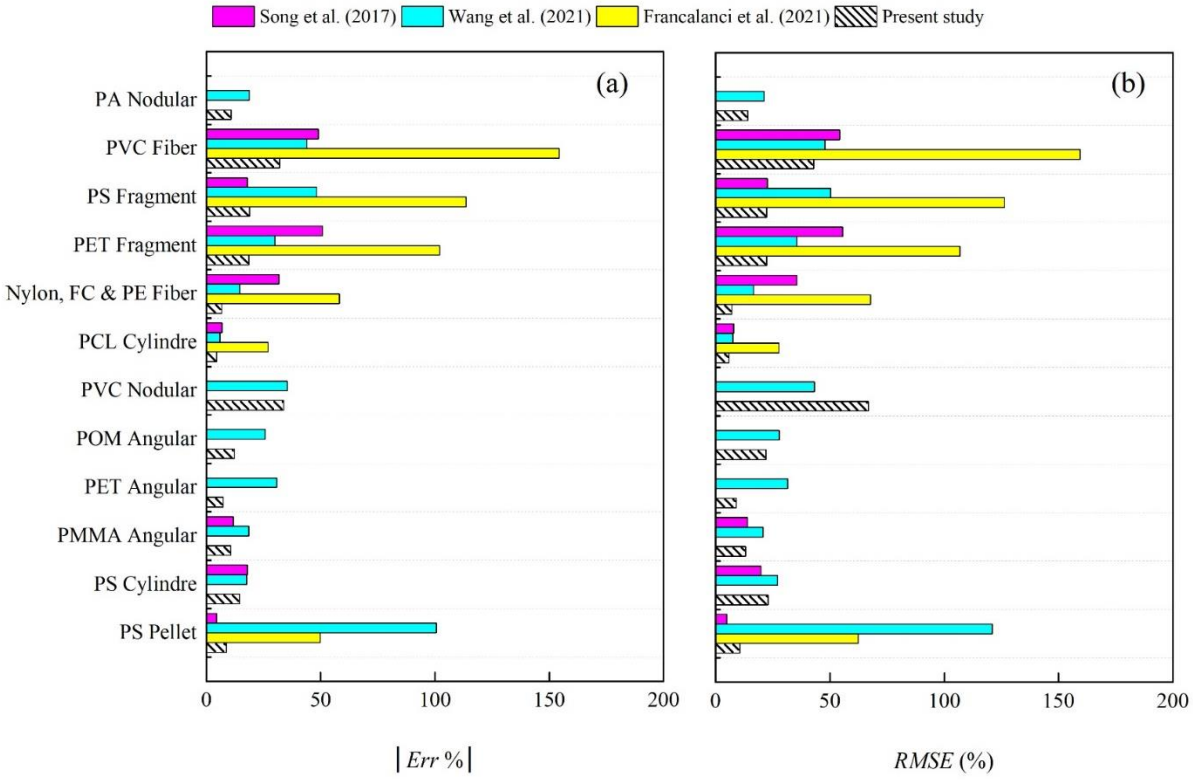

Figure 2-6 Absolute relative error ($|Err\%|$) and root-mean-square error (*RMSE*) of w_s for MPs of different materials and shapes, using the formulas in Table 2-3. The comparisons were made against the experimental w_s values from the studies listed in Table A-2.

2.4.4. Limitations of the m*odel*

The first limitation of the present model is that it currently only focuses on the transitional regime (Re_p = 1 - 300). In the laminar regime (Re_p < 1), so far only one study on micrometer MPs (Kaiser et al., 2019) has been reported where w_s is small. For the turbulent regime ($Re_p > 10^3$), similarly, only one study (Khatmullina & Isachenko, 2017) with limited data points for spherical MPs has been reported (Figure 2-1). More experimental data points are needed to expand the present model to the laminar and turbulent regimes.

Besides, the present model only considers the settling of single particles. The flow disturbance produced by neighboring particles (Uhlmann & Doychev, 2014) is neglected. Hence, the model is applied to the case where the concentration of MPs is small enough to neglect such neighboring/swarm effects. Since no MP studies have provided the concentration threshold, further research should be conducted concerning this topic. Moreover, this model does not include the impact of ambient water turbulence on the settling of MPs. In fact, limited studies have been reported in this area. Wang et al. (2021) found that the average w_s of MPs in isotropic turbulence considerably reduced compared to that in a quiescent fluid; and under the isotropic turbulence condition itself, w_s can be suppressed or enhanced depending on turbulence intensity. More work should be done to quantify the effect of ambient turbulence on the w_s of MPs.

2.5. Conclusions

Settling of MPs in oceans and freshwater is important for studying the transport and fate of MPs and assessing their environmental or ecological impacts. However, existing formulas on the drag coefficient (C_d) and models for the terminal settling velocity (w_s) are not able to accurately predict them due to the various shapes, sizes, and materials of MPs. In this study, a new C_d formula [Eq.

(2-16)] and an explicit w_s model [Eqs. (2-16) and (2-17)] for MPs were proposed based on the experimental data reported in 2016 - 2021 (1,343 raw data and 699 filtered data). The main conclusions are as follows:

1. Particle sphericity (Φ) and Corey's shape factor (*CSF*) are two important shape descriptors that each has an important impact on C_d of MPs. The two parameters are suggested to be used together to reflect the particle shape impact.

2. The new C_d formula introduces the dimensionless particle diameter (d_*), Φ, and *CSF* and modifies the drag law for spherical particles. The new formula shows better accuracy than the four existing formulas, with $|Err\%| = 15.2\%$ and $RMSE = 17.3\%$, smaller than $|Err\%| = 42.5$ - 72.8% and $RMSE = 49.0$ - 105.8% of the existing formulas.

3. The present explicit w_s model also shows better accuracy than the three existing explicit models. The present model's $|Err\%| = 8.8\%$ and $RMSE = 11.4\%$, both are lower than $|Err\%| = 15.4$ - 77.2% and $RMSE = 21.0$ - 84.9% of the three existing models.

4. The present C_d formula and w_s model can be applied to the transitional regime ($Re_p = 1$ - 300), in which most of the existing MP data lie. More experiments are needed for the laminar regime ($Re_p < 1$) and turbulent regime ($Re_p > 10^3$) to expand the current formula and model to these regimes.

3. The incipient motion of exposed microplastics in open-channel flow[2]

3.1. Introduction

Recent studies have shown that microplastic (MP) pollution is ubiquitous in aquatic environments (Ballent et al., 2013; Ballent et al., 2012). The abundance, adverse impacts, and removal of microplastics (MPs, $\lesssim$ 5 mm) have been or are being investigated extensively (Schell et al., 2020; Yang et al., 2021). However, studies of the transport of MPs in freshwater and oceans, especially the incipient motion (the initiation of movement) of MPs, are quite limited (Waldschläger et al., 2022). To further understand the transport and fate of MPs and guide their pollution control (Wu et al., 2019), it is important to understand the mechanism of incipient motion for MPs.

Previous studies on MP dynamics mainly focused on rising and settling processes (Khatmullina & Isachenko, 2017; Kowalski et al., 2016; Morét-Ferguson et al., 2010). Since half of all plastics are denser than seawater (Morét-Ferguson et al., 2010), the terminal settling velocity, w_s, is a key parameter to characterize the migration of MPs in water bodies (Kowalski et al., 2016). Studies have found that the density, shape, and particle size of MPs have substantial impacts on w_s (Kowalski et al., 2016). After MPs settle to the riverbed or seafloor, stream-wise transport starts with particle incipient motions under the action of currents. So far, only two studies have examined the threshold of MP incipient motion (Ballent et al., 2013; Waldschläger & Schüttrumpf, 2019b). The minimum flow shear stress required to move a single particle, defined as the critical shear

[2] The content of this chapter has been published as: Yu, Z., Yao, W., Loewen, M., Li, X., & Zhang, W. (2022). Incipient motion of exposed microplastics in an open-channel flow. *Environmental Science & Technology*, *56*(20), 14498-14506.

stress τ_c, has been extensively used for sediment incipient motion (Dey, 2014). The two studies on MP incipient motion also used this indicator. For example, Ballent et al. (2013) reported that when $\tau_c = 0.025$ N/m^2, 50% of the MP pellets with particle density $\rho_p = 1055 \pm 36$ kg/m^{-3} began to move in experiments. In nature, when τ_c is small, sediments can start sliding or rolling; but as the flow velocity increases, the behavior of the advected sediments may change and they travel in a series of low hopping motions known as saltation (Hubert & Kalman, 2003). Waldschläger and Schüttrumpf (2019b) considered sliding, rolling, or saltation or MPs and experimentally investigated the τ_c values of 14 types of MPs with various shapes (cylinder; semi-cylinder; poly-cylinder; angular; pellet; lenticular), densities (1008 - 1368 kg/m^3), and sizes (0.75 - 5.04 mm) on sediment beds of different roughness (k_s = 0.5, 1.0, 1.5, and 3 mm). An equation was then developed to calculate τ_c, which is, to the authors' best knowledge, so far, the only equation in the literature for MP incipient motion:

$$\Theta_c = 0.5588\Theta_c^* \left[\frac{D_n}{D_{50}} \right]^{-0.503} \tag{3-1}$$

where Θ_c (= τ_c / [(ρ_p-ρ)gD_n]) is the critical Shields parameter for MPs (Dey, 2014); ρ is ambient fluid density; D_n is the nominal diameter which is the diameter of the volume equivalent sphere; D_{50} is the median grain size of the sediment bed; Θ_c^* is the critical Shields parameter of the sediment bed. Note that Eq. (3-1) is only valid for rough beds and has a coefficient of determination, $R^2 = 0.74$.

The knowledge gap on MP incipient motion, firstly, is that only four types of MPs: Polystyrene (PS), Polyamide (PA), Polyvinyl chloride (PVC), and Polyethylene terephthalate (PET) were discussed (Waldschläger & Schüttrumpf, 2019b). Other MP types commonly detected in the rivers,

like acrylonitrile-butadiene-styrene (ABS) (Kabir et al., 2022), polycarbonate (PC) (Duan et al., 2020), polymethyl methacrylate (PMMA) (Kabir et al., 2022), and polyoxymethylene (POM) (Zhu et al., 2019), have not been reported. The application range of the current prediction equation for MP incipient motion [Eq. (3-1)] needs further testing for different types of MPs.

In addition, the shapes of the MPs particles were not considered in the current prediction equation [Eq. (3-1)], which are, however, expected to have an important impact on τ_c (Waldschläger & Schüttrumpf, 2019b) and Θ_c. Moreover, it is well-known from sediment studies that the saltation of particles has a different mechanism (Dey & Ali, 2017; Wu & Chou, 2003) from rolling or sliding and requires higher shear stress. In the cases of MPs, particles may slide or roll before saltation occurs (Dey & Ali, 2017; Wu & Chou, 2003). Since Eq. (3-1) was obtained by fitting the experimental data for MP in all 3 motion modes (sliding, rolling, or saltation), it may overestimate τ_c and Θ_c of MPs in the mode of sliding or rolling.

In addition to τ_c and its dimensionless form Θ_c, the critical incipient flow velocity, U_i, is another critical flow parameter. Sediment transport studies have quantified U_i, especially for cases where the flow is modified by bed features such as dunes or aquatic vegetation (Aguirre-Pe et al., 2003; Bong et al., 2016). To the best of the authors' knowledge, U_i values for MPs have not been reported.

In this study, experiments were conducted to determine both U_i and τ_c for 19 types of MPs of various sizes, densities, and shapes. Two different bed roughness conditions (smooth and rough beds) were examined. A new equation was proposed to estimate the threshold of incipient motion of MPs with rolling and sliding as the mechanisms.

3.2. Experimental setup and methodology

MPs and non-cohesive sediment particles have similar geometric characteristics, and therefore principles from the incipient motion of sediment have been applied to MPs (Enders et al., 2019; Waldschläger & Schüttrumpf, 2019b). The critical Shields parameter Θ_c^* for sediment depends on the shear Reynolds number $Re_* = U_* D_n/\nu$, where U_* is the shear velocity, and ν is the kinematic viscosity of ambient flow. For given fluid and sediment parameters, trial and error procedures or iterations have to be applied to determine the critical bed shear velocity via the classic Shields Diagram (Cao et al., 2006).

To avoid these iteration processes, the dimensionless grain diameter d_* (= $[(\rho_p-\rho)g/\rho\nu^2]^{1/3} D_n$), was introduced and an analytical formula for Θ_c^* was proposed (Paphitis, 2001), which is valid for $0.01 < Re_* < 10^4$:

$$\Theta_c^* = \frac{0.273}{1+1.2d_*} + 0.046\left(1-0.576e^{-0.02d_*}\right) \tag{3-2}$$

Cao et al. (2006) developed the following explicit formula of Θ_c^* for natural sediment:

$$\Theta_c^* = \begin{cases} 0.1414 d_*^{-0.3459}, & d_* < 3.52 \\ \dfrac{\left[1+\left(0.0223 d_*^{3/2}\right)^{2.8358}\right]^{0.3542}}{3.0946 d_*^{1.0153}}, & 3.52 \le d_* \le 43.09 \\ 0.045, & d_* > 43.09 \end{cases} \tag{3-3}$$

The critical movability number, Λ_c (= U_*/w_s), has also been widely used as an alternative to the Shields parameter for sediment. Paphitis (2001) developed an analytical formula describing Λ_c as a function of Re_*, which is valid for $0.1 < d_* < 10^5$:

$$\Lambda_c = \frac{0.75}{Re_*} + 14\mathrm{e}^{-2Re_*} + 0.01\ln Re_* + 0.115 \tag{3-4}$$

Since Re_* can be replaced via d_* ($= \left[\frac{Re_*^2}{\Theta_c^*}\right]^{1/3}$) according to Yang et al. (2019), a Λ_c - d_* relationship can be established to calculate Λ_c explicitly.

Beheshti and Ataie-Ashtiani (2008) found that: Λ_c is more suitable for determining the threshold of motion compared with Θ_c^*. Their formula for Λ_c (valid for $0.4 < d_* < 10^3$) is:

$$\Lambda_c = \begin{cases} 9.6674 d_*^{-1.57}, & d_* \le 10 \\ 0.4738 d_*^{-0.226}, & d_* > 10 \end{cases} \tag{3-5}$$

Simoes (2014) improved the Λ_c - d_* relationship proposed by Beheshti and Ataie-Ashtiani (2008) by using comprehensive experimental data for sediments to derive a new empirical formula (valid for $0.1 < d_* < 10^5$):

$$\Lambda_c = 0.215 + \frac{6.79}{d_*^{1.70}} - 0.0750\mathrm{e}^{-2.62\times10^{-3} d_*} \tag{3-6}$$

Simoes (2014) also proposed that Θ_c^* has the following relationship with Λ_c:

$$\Theta_c^* = \frac{4}{3C_\mathrm{d}} \Lambda_c^{\,2} \tag{3-7}$$

where C_d is the drag coefficient of sediment.

Moreover, in studies for sediments, the incipient flow velocity was often used in analyzing the sediment incipient motions, which can be expressed in a dimensionless form as the densiometric

Froude number F^* (Aguirre-Pe et al., 2003; Bong et al., 2016). F^* is defined as the ratio of flow inertia to the particle submerged weight:

$$F^* = \frac{U_i}{\sqrt{gD_n \frac{\rho_p - \rho}{\rho}}} \tag{3-8}$$

3.3. Experimental methods

MPs of seven materials were selected based on previous studies on MP abundance in aquatic environments (Waldschläger & Schüttrumpf, 2019b; Zhang, 2017), including ABS, PA, PC, PET, PMMA, POM, and PVC. The MPs were uniform in size for each type with particle masses = 0.01 - 0.09 g, particle densities ρ_p = 1.040 - 1.410 g/cm^3, and nominal diameters, D_n = 2.5 - 5.3 mm. A detailed summary of the MP particle information is in Table 3-1. The selected MPs have various shapes including cylinder, semi-cylinder, poly-cylinder, angular, pellet, and lenticular (Figure 3-1a). To consider the shape effects of MPs, Corey's shape factor (*CSF*) defined as $c/(ab)^{1/2}$, was calculated, where a, b, and c are the lengths of the longest, intermediate, and shortest sides of a particle, respectively (Waldschläger & Schüttrumpf, 2019a).

Table 3-1 Properties of MPs tested in this study.

Material	**Shape**	D_n **(mm, ± 0.1)**	ρ_p **(g/cm^3, ± 0.01)**	***CSF***	$n = [gD_n(\rho_p-\rho)/\rho]^{0.5}$ **(m/s)**
PA	Cylinder	3.2	1.203	0.66	0.78
PA	Semi-cylinder	2.6	1.203	0.47	0.77
PET	Cylinder	2.8	1.407	0.74	0.80
PET	Poly-cylinder	3.5	1.407	0.65	0.81
PET	Semi-cylinder	2.4	1.407	0.64	0.79
PVC	Cylinder	4.2	1.249	0.89	0.79
PVC	Semi-cylinder	3.4	1.249	0.57	0.79

PVC	Angular	3.5	1.249	0.92	0.79
PVC	Pellet	3.9	1.249	0.98	0.79
PVC	Lenticular	3.6	1.249	0.80	0.79
PMMA	Cylinder	3.2	1.196	0.76	0.78
PMMA	Poly-cylinder	4.1	1.196	0.70	0.79
PMMA	Semi-cylinder	2.5	1.196	0.68	0.77
POM	Cylinder	5.1*	1.390	0.69	0.82
POM	Semi-cylinder	3.6	1.390	0.70	0.81
PC	Cylinder	5.2*	1.050	0.86	0.74
PC	Semi-cylinder	4.4	1.050	0.58	0.74
ABS	Cylinder	5.3*	1.040	0.76	0.73
ABS	Semi-cylinder	4.3	1.040	0.73	0.73

*Values of D_n can be rounded to 5 mm and they are still treated as MPs in this study.

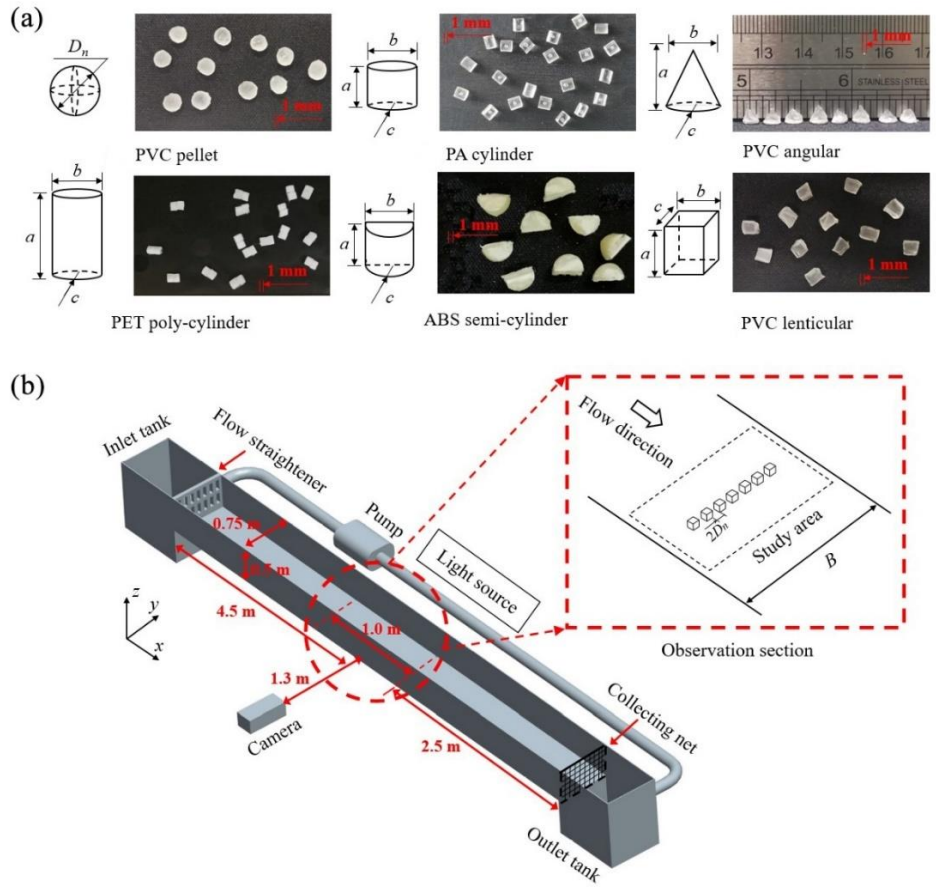

Figure 3-1 The shapes of MPs used in this study (a) and the sketch of the experimental setup (b).

The settling velocities of the various MPs were determined experimentally and then used in the calculation of the critical movability number Λ_c. Settling velocity was measured in an acrylic glass column tank with a cross-section of 20 × 20 cm and a height of 120 cm. The procedure described by Ballent et al. (2013) was used in this study. To avoid the effects of surface bubbles, the MP particle was then placed 2 cm below the water surface in the tank center and allowed to fall freely. The particle reached the terminal settling velocity at ~15 cm. From this position, a stopwatch was used to measure the time that the particle took to fall 90 cm. The experiments were repeated at least 3 times for each type of MPs. The terminal settling velocities w_s for different types of MPs were calculated as the ratio of settling distance to time.

The MP incipient motion experiments were carried out in a 7.50 m-long, 0.75 m-wide, and 0.50 m-deep glass recirculating flume with a slope of 0.002 (Figure 3-1b). The pump was controlled by a variable frequency drive with a maximum discharge of 150 L/s and a resolution of 1.31 L/s. Flow rates were measured with a magnetic flow meter. The flow depth was kept constant at h = 43.5 cm in this study. The water passed through a flow straightener at the upstream end to produce a uniform velocity distribution. The experimental section had a length of 1.0 m and was 4.0 m downstream of the flow straightener (Figure 3-1b). Results from preliminary experiments showed that flow was fully developed within the experimental section. The incipient motion velocity, U_i, of individual MPs was determined by using the technique described by Rabinovich and Kalman (2009). U_i was defined as the ambient cross-sectional averaged flow velocity U under which 50% of the particles were in motion. First, 20 - 25 particles were placed at rest on the bed with a spacing of $2D_n$ at x = 4.5 m from the flume entrance in the study area (Figure 3-1b) and a distance of 0.18 - 0.28 m from the flume side walls. The spacing between particles was set to minimize particle-particle interactions during their initial mobilization. The discharge, Q, was increased by

controlling the output voltage of the variable frequency drive using a specially developed computer program. The output voltage was increased stepwise (0.1 V) corresponding to an increase of U of 0.5 cm/s. The values of Q were recorded from the moment at which any of the MPs started to move by either rolling or sliding until all MPs left the controlled area (Figure 3-1b). Each trial was repeated at least 5-7 times and recorded by a digital camera (10 fps, Sony DSC-HX200V). The number of moving particles under different discharges was counted by viewing the videos. Each trial provided a single measurement of the incipient velocity U for a particular MP type, and these values were averaged over the number of repeated trials to provide mean values, U_i.

The experiments were conducted both on a smooth bed and a rough bed with bed roughness height k_s = 0.5 mm. The experiments were first conducted directly on the flume bottom (glass) to simulate the case where MPs move on a smooth bed. Then, uniform simulated sediments (glass beads) with a nominal diameter of 0.5 mm were placed on the flume bottom and covered the entire study area to represent a rough bed case. The Manning's roughness coefficients for the smooth and rough beds, based on the bed materials, are estimated to be 0.009 and 0.016, respectively. The movement mode of particle incipient motion was related to the ratio of particle size to bed roughness height, D_n/k_s (Ancey et al., 2002). The selected minimum D_n/k_s (= 5) in this study was higher than 2 to ensure that MPs primarily move in the mode of sliding or rolling (Ancey et al., 2002). When $D_n/k_s >$ 1, the sheltering effects of the bed grains that act to shield the movements of MPs from the flow are low (Waldschläger & Schüttrumpf, 2019b), and MPs are exposed to the ambient flow. That is, the impacts of sheltering effects on MP incipient motions were not included in this study.

To obtain the critical bed shear stress, the ambient velocity data were collected at the flow rate at which incipient MP motion was detected. The instantaneous stream-wise velocity $u(t)$, the lateral velocity $v(t)$, and the vertical velocity $w(t)$ were measured with a Nortek Vectrino Acoustic

Doppler Velocimeter (ADV). The raw data were de-spiked using the method of Goring and Nikora (2002). $u(t)$, $v(t)$, and $w(t)$ with correlations < 85% and a signal-to-noise ratio (SNR) < 25 dB were removed. A MATLAB code was used to extract the time-averaged velocities (u, v, and w) and the fluctuating components (u', v', and w'). The critical bed shear stress τ_c was calculated from the velocity data using the 3-D turbulence kinetic energy (TKE) method, which has been widely used on a rough bed (Thompson et al., 2003; Wang et al., 2016):

$$\tau_c = \rho U_*^2 = 0.5C\rho(\overline{u'}^2 + \overline{v'}^2 + \overline{w'}^2) \tag{3-9}$$

where U_* is the shear velocity and C = 0.19. Results from pre-experiments showed that lateral distributions of velocity and shear stress of the experimental section were uniform for each case (Figure B-1 in Appendix B). The critical shear stresses computed from Eq. (3-9) were used to calculate the critical Shields parameter Θ_c and the critical movability number Λ_c for MPs with Eqs. (3-1) and (3-7). Statistical analysis of the experimental data was conducted in SPSS Statistics 22.0.

3.4. Results and discussion

3.4.1. The incipient flow velocity

Figure 3-2 shows the incipient velocity U_i increases approximately linearly with n (= $[gD_n(\rho_p-\rho)/\rho]^{0.5}$) for the different types of MPs. Since the ratio of U_i to n represents F^* according to Eq. (3-8), the value of F^* varies from 0.096 to 0.24 based on Figure 3-2. Overall, the increasing trend of U_i with n indicates that more kinetic energy is required to move a heavier and/or larger MP particle. For an individual MP material, however, it may not be the case. For example, for MPs of ABS, PC, and PA, U_i increases as n decreases. In these cases, the shape effect of MPs described by *CSF* should be considered.

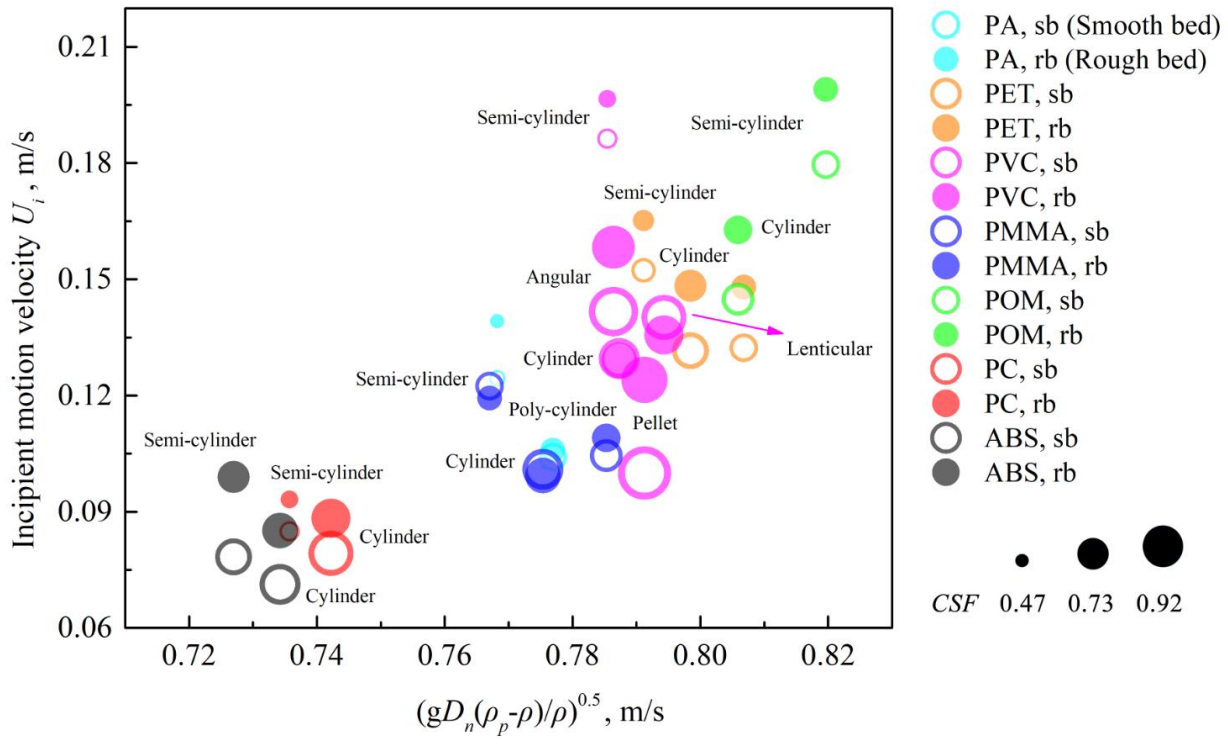

Figure 3-2 The incipient motion U_i as a function of n (= $[gD_n(\rho_p-\rho)/\rho]^{0.5}$). The larger size of a data point indicates a higher *CSF* value of MPs.

An analysis of variance was performed to examine whether the differences in the U_i values measured from the repetitive trials caused by the impact of particle shapes were statistically significant while keeping k_s and n the same. Table B-1 in Appendix B lists the *P*-values of U_i of MPs with different *CSF*. The analysis showed that the differences were significant at the 5% level (i.e., *P-value* < 0.05) except for the PC particles on the rough bed. This indicates that changes in the MP shape or *CSF* cause statistically significant changes in U_i.

For further comparison, in Figure 3-2, the value of *CSF* is indicated by the size of the data point and the larger size represents a higher *CSF* value. For the same MP material, semi-cylindrical particles with low *CSF* values have the highest U_i, while particles with high *CSF* values (like a cylinder or pellet) tend to have the lowest U_i. For instance, for PC particles, the semi-cylindrical

particles (*CSF* = 0.58) had a significantly larger U_i (*P-value* = 0.02) than the larger cylindrical particles (*CSF* = 0.86). The reason for this is that non-spherical particles have larger contact areas on the bed and particles start their motion by sliding, while the near-spherically-shaped particles tend to start their motion by rolling which requires less energy provided by flow (Choi & Kwak, 2001).

Moreover, the mean value of U_i for all smooth bed cases is slightly lower than that for the rough bed cases, 0.11 m/s versus 0.14 m/s. The difference in U_i on different beds is statistically significant (*P-value* = 0.045 < 0.05) and the impacts of bed roughness k_s on U_i cannot be ignored. On average, values of U_i for ABS particles are most sensitive to changes in bed roughness; while PMMA particles are least sensitive, although the two types of MPs have similar values of *n* and *CSF* (Table 3-1). The mean value of U_i for ABS particles is most influenced by the increase of k_s, which increases by 23%; PMMA particles take the least impact of k_s, increasing by only 0.09%.

3.4.2. Critical shear stress

Though U_i is easy to be determined for a given Q and cross-section area, it only provides an approximate estimate of the threshold condition for MP incipient motion, in which U_* and τ_c play key roles (Dey, 2014). Figure 3-3 presents the mean values of critical shear stress τ_c for the MPs in this study. From the left to the right of the x-axis of Figure 3-3, the mean value of *n* increases; the value of *CSF* decreases for the same MP material (i.e., more irregularly shaped particles). Particle properties such as ρ_p, D_n, and *CSF*, as well as bed roughness, show a combined effect on the magnitude of τ_c in Figure 3-3. Since the increase in $u*$ and thus the increase in τ_c generally represent the increase of flow velocity (Dey, 2014), τ_c and *n* also show a similar positive

relationship as U_i and n. For example, the POM cylinder with n = 0.82 m/s has higher τ_c (0.72 vs. 0.16 N/m^2) than the PC cylinder with n = 0.74 m/s.

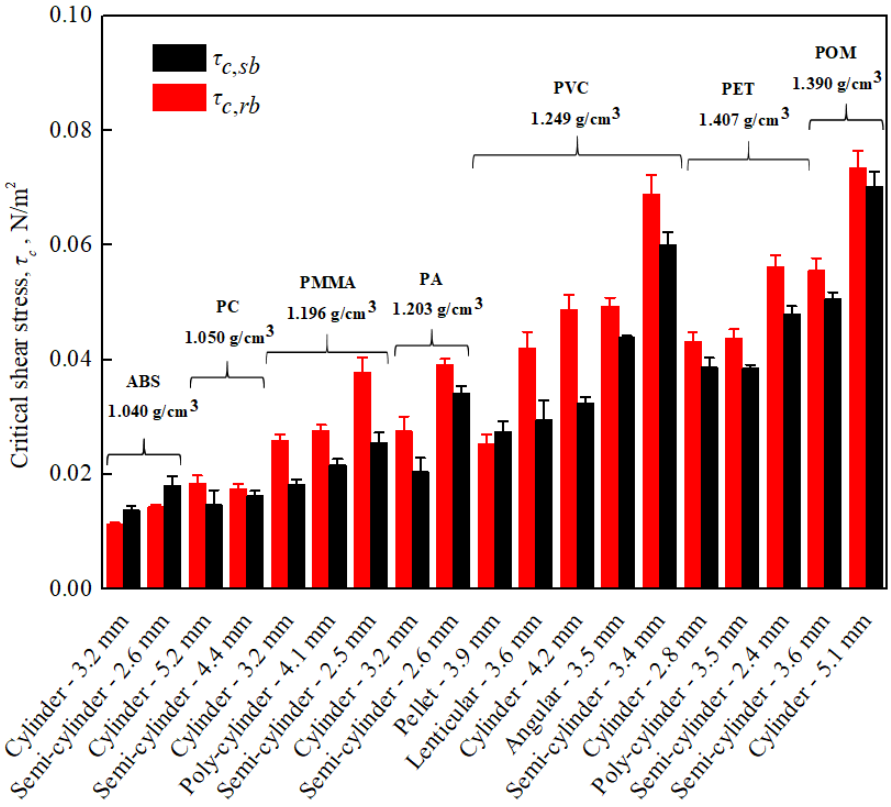

Figure 3-3 The experimentally determined critical shear stresses for MP incipient motion, sorted by MP types, shapes, and D_n. $\tau_{c,sb}$, and $\tau_{c,rb}$ represent the critical shear stress measured on the smooth bed and rough bed, respectively.

Figure 3-3 shows that τ_c consistently increases as *CSF* decreases for each type of MPs. For example, for PVC angular and semi-cylinder particles with similar sizes (D_n = 3.5 vs. 3.4 mm), their *CSF* values are 0.92 and 0.57, and τ_c values are 0.45 and 0.63 N/m^2. According to Waldschläger and Schüttrumpf (2019b), *CSF* has an impact on the drag force F_d, which is one of the main forces governing the incipient motion of MPs and hence affects τ_c. For example, PVC angular particles

with a high *CSF* (= 0.92) require smaller F_d, to initiate motion while PVC semi-cylinder with *CSF* = 0.57 has larger F_d because it has a larger surface contact and shear resistance with the bed.

Moreover, generally, larger critical shear stresses for MPs occurred on the rough bed (red bars) compared to on the smooth bed (black bars). The mean value of τ_c (0.039 N/m^2) for rough bed cases was 18% higher than that for smooth bed cases (0.033 N/m^2). The reason for this is likely that a rough bed causes deflections of the flow near the bed and increases the form drag (Buffington & Montgomery, 1997). The increase of form drag over roughness elements contributes to the increase of surface shear stress (Cheng & Castro, 2002) and thus increases τ_c required for incipient motion.

3.4.3. Threshold for MP incipient motion

Figure 3-4 presents the critical Shields parameter Θ_c values of MPs measured in this study and Waldschläger and Schüttrumpf (2019b). Note that only the data measured on similar bed roughness conditions in Waldschläger and Schüttrumpf (2019b) are included. The two widely-used Θ_c - d_* equations for sediments (Cao et al., 2006; Paphitis, 2001) are also shown in Figure 3-4 for comparison purposes, and the data points that fall above the Θ_c - d_* equation curves indicate that particles would start to move from the static state on the bed (and vice versa). According to Ancey et al. (2002), when $\Theta_c < 0.01$, exposed particles started their motions mainly by rolling or sliding rather than saltation. In Figure 3-4, 95% of Θ_c values are smaller than 0.01, meaning that MPs used in this study and the selected cases of Waldschläger and Schüttrumpf (2019b) started their motions predominantly by rolling and/or sliding. The appearance of rolling and/or sliding of MPs was further confirmed by the recorded videos.

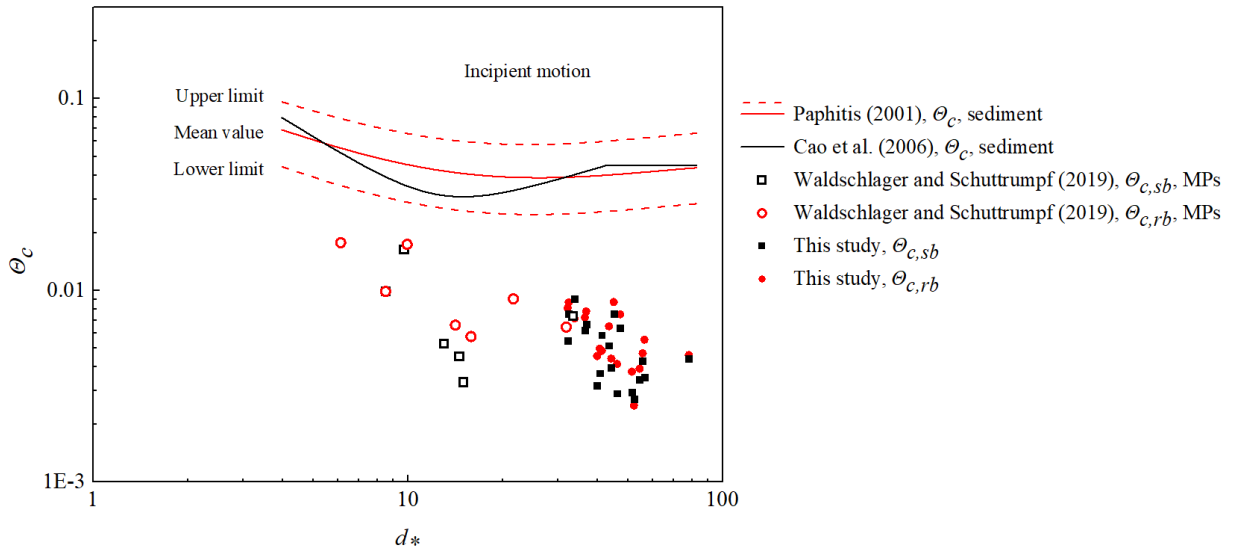

Figure 3-4 Comparison of the measured Θ_c - d_* data points for MPs reported in this study and Waldschläger and Schüttrumpf (2019b) with the classic relationships for sediment.

Figure 3-4 shows that the Θ_c - d_* relationships for natural sediment dramatically overestimate the Θ_c values required to induce incipient motion of MPs. On the other hand, Θ_c may not be the appropriate parameter for predicting the incipient motion of MPs. The reason is that both Θ_c and d_* do not include the impact of particle geometry on the critical shear stress. According to previous studies (Francalanci et al., 2021; Khatmullina & Isachenko, 2017; Yu, Yang, & Zhang, 2022), the MP settling velocity, w_s, is affected by MP particle properties like shape, density, and size. Therefore, as discussed previously, another dimensionless parameter Λ_c, the movability number (Simoes, 2014) that is dependent on U_* and w_s, is proposed in this study as a potentially more suitable parameter for predicting the incipient motion of MPs.

In Figure 3-5, the measured Λ_c - d_* data points for MPs reported in this study and Waldschläger and Schüttrumpf (2019b) are compared with three classic relationships for natural sediment. Note that the Λ_c values for MPs in Waldschläger and Schüttrumpf (2019b) were estimated by using the MP settling velocities that were obtained from Eqs. 10 and 14 in the study of Waldschläger and

Schüttrumpf (2019a). Similarly, as shown in Figure 3-4, all of the classic Λ_c - d_* relationships for sediment overestimate the values of Λ_c for MPs. From Figure 3-4 and Figure 3-5, it is clear that the incipient motion formulas developed for sediment particles are not suitable for MPs, due to the great differences in their physical properties (density and shape).

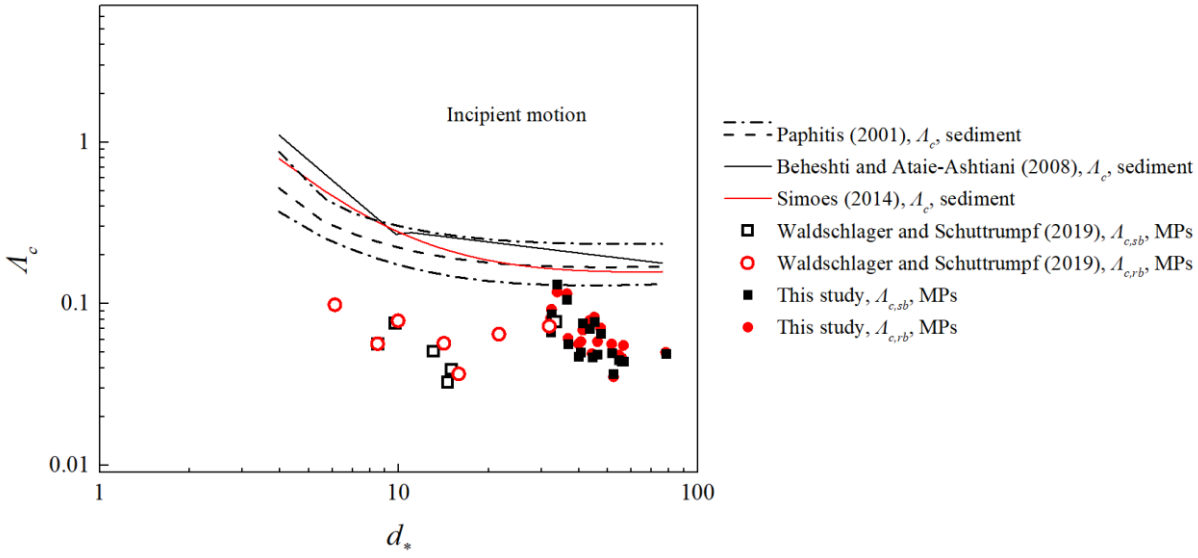

Figure 3-5 Comparison of the measured Λ_c - d_* data points for MPs reported in this study and Waldschläger and Schüttrumpf (2019b) with the classic relationships for sediment.

Compared to the Θ_c data scatteredness (0.002 - 0.02) in Figure 3-4, the Λ_c data scatteredness (0.03 - 0.015) is smaller in Figure 3-5. The sediment study of Simoes (2014) showed that with more measurement data added to Shields' diagram, the band of Θ_c - d_* was expanded which would reduce the prediction accuracy of Θ_c (Simoes, 2014). In the case of MPs, it can be seen that adding the data points of Waldschläger and Schüttrumpf (2019b) substantially increases the data scatteredness of Θ_c in Figure 3-4, but it has no impact on the data scatteredness of Λ_c in Figure 3-5. The comparisons of Figure 3-4 and Figure 3-5 further confirm that Λ_c is potentially a more suitable parameter than Θ_c for MP incipient motion.

Table B-2 (see Appendix B) shows the statistical analysis of the multiple linear regression between Λ_c and MP properties (D_n, CSF, and $(\rho_p - \rho)/\rho$). It appears that all three MP properties are highly statistically significant ($P < 0.05$). The variance inflation factor (VIF) values are 1.1 - 1.5, which are < 4, meaning all these factors contribute independently to the determination of Λ_c (Akinwande et al., 2015). To reflect the combined effect of these factors, a new dimensionless particle parameter, $m = [(\rho_p-\rho)/\rho](D_n/h)\cdot CSF$, was introduced in this study.

In Figure 3-6, Λ_c is plotted versus m and the data points appear to have a strong nonlinear correlation. Hence, a nonlinear least-squares method was used to derive a new relationship between Λ_c and m specifically for MPs:

$$\Lambda_c = \beta_1 \ln(m) + \beta_2 \tag{3-10}$$

where β_1 and β_2 are constants obtained by fitting with the experimental MP data from this study and Waldschläger and Schüttrumpf (2019b). The fitted values of β_1 and β_2 and their 95% confidence intervals are given in Table B-3 (see Appendix B). The benefit of Eq. (3-10) is that it allows for the explicit determination of Λ_c using m, which is solely determined by the ambient fluid and MP properties.

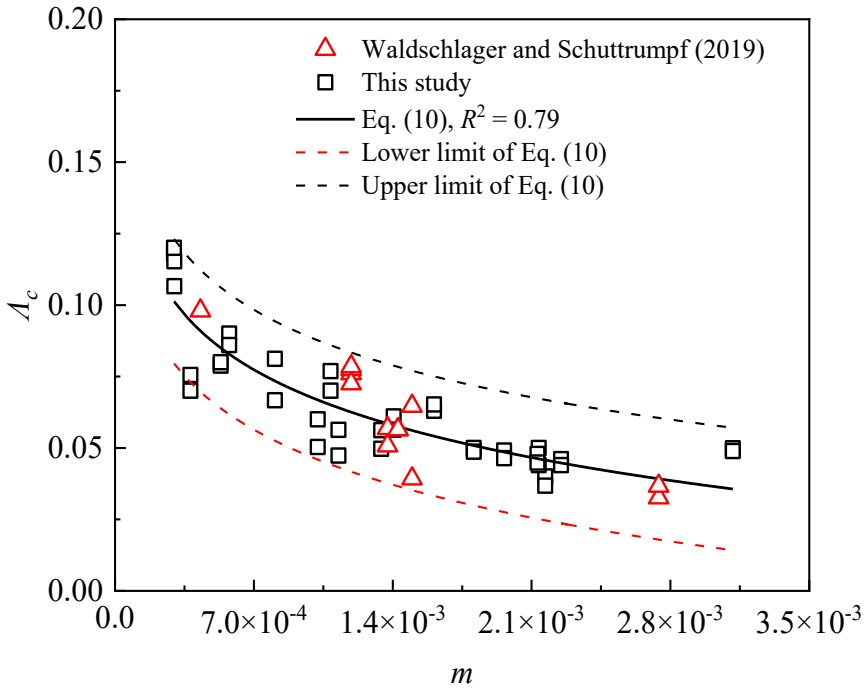

Figure 3-6 Λ_c as a function of m for MPs. The solid line denotes Eq. (3-10). The dashed lines indicate the upper and lower limit of the 95% confidence interval of Eq. (3-10).

The coefficient of determination of Eq. (3-10) is $R^2 = 0.78$, the absolute relative error $|Err\%| = 12.33\%$, and the relative root mean squared error, $RRMSE = 15.94\%$, indicating that this new equation is reasonably accurate. The accuracy of predicting Λ_c using Eq. (3-10) was compared with the existing formula [Eqs. (3-1) and (3-7)] for MPs. The existing formulas gave $|Err\%| = 55.61\%$ and $RRMSE = 56.98\%$, which are approximately five times the errors of using Eq. (3-10). This demonstrates the advantage of the new Λ_c formula, compared to the existing formula.

Figure 3-7 shows the further comparison of measured $\Lambda_{c,meas}$ and calculated $\Lambda_{c,clac}$ between the new formula [Eq. (3-10)] and the existing formula. In Figure 3-7, the slope between the measured and calculated Λ_c values is close to unity (0.97, Figure 3-7b) for the new formula, while it is 0.43 (Figure 3-7a) from the existing formula. This indicates that the proposed new formula is more robust for a wider range of applications for MPs. Moreover, the new formula has a higher R^2 (0.78,

Figure 3-7b) than that of the existing formulas (0.29, Figure 3-7a), which means the new formula has a higher precision in predicting Λ_c. Based on the results above, the new formula [Eq.(3-10)] is recommended for future use to calculate Λ_c and thus the critical shear stress for incipient motion of MPs with different shapes, densities, and sizes on both smooth and rough beds.

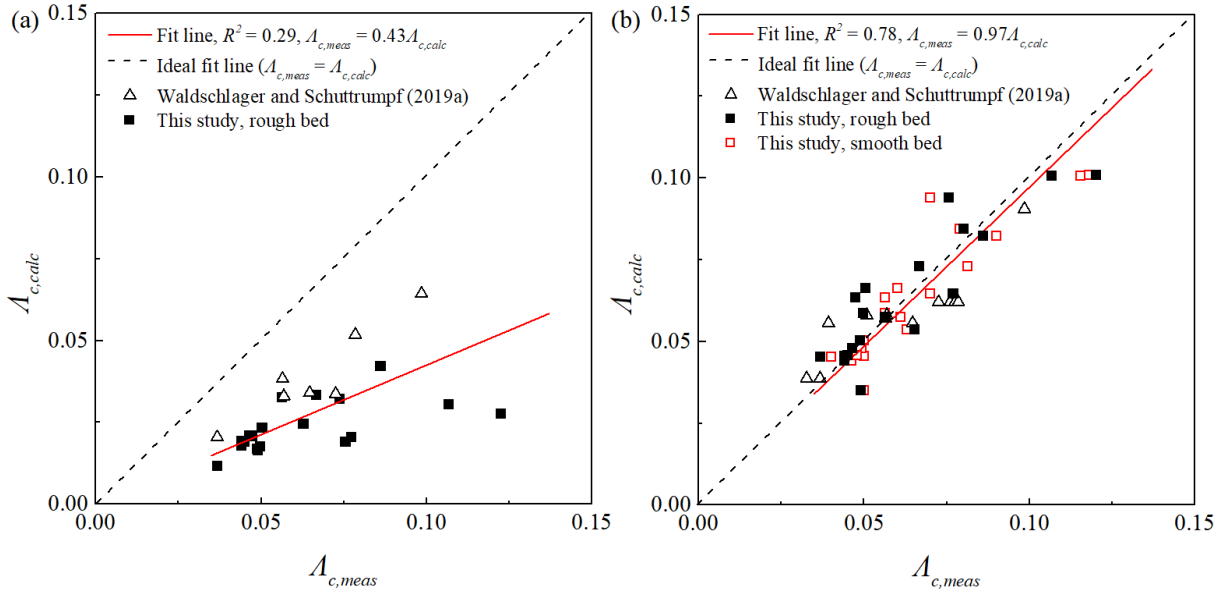

Figure 3-7 Comparison of the experimental data of Λ_c with those calculated with (a) the formula of combining Waldschläger and Schüttrumpf (2019b) [Eq. (3-1)] with Simoes (2014) [Eq. (3-7)] and (b) the formula from this study [Eq. (3-10)].

Many questions still need to be answered in future research. For example, the proposed criterion for MP incipient motion is applicable for cases with high ratios of particle size to roughness height ($D_n/k_s > 2$) and the millimeter-sized MPs with $CSF > 0.47$. That is, this study only considered the cases where the sheltering effect of the bed roughness element is small, and thus MPs only move in the form of rolling and/or sliding. For the cases with non-uniform beds and bed armoring with small D_n/k_s values, the sheltering effects cannot be neglected and are worthy of future research.

Moreover, to find a general expression of U_i, the relative position between particles and bed rough elements is required (Aguirre-Pe et al., 2003; Bong et al., 2016), which needs further research.

4. An investigation of the sheltering effects on the mobilization of microplastics in open-channel flow[3]

4.1. Introduction

Microplastics (MPs, < 5 mm) are being actively and widely studied because of their persistence and adverse effects on the health of aquatic environments (Harris, 2020; Yang et al., 2021). Rivers, serving as a primary route for microplastic (MP) transport, caused widespread MP pollution in marine, coastal, and estuarine environments (Tramoy et al., 2020). Understanding MP transport in rivers can help us better understand and predict MP distributions and transport pathways, which will facilitate more effective planning and implementation of cleanup operations, mitigating MP pollution (Critchell & Lambrechts, 2016). Previous MP studies have mainly focused on spatial and temporal distribution patterns (Harris, 2020; He et al., 2021; Yang et al., 2021), whereas the process of MP transport in rivers has received less attention.

After entering a river, MPs can either float on the water surface, suspend in the water column, or sink into riverbeds, depending on their densities. For MPs with densities $\rho_p > 1$ g/cm^3, the riverbed will act as a sink and if there is an increase in river flow rate, the deposited MPs may be remobilized, expanding the distribution of MP pollution (Liro et al., 2020). Therefore, an in-depth investigation of the critical hydrodynamic conditions of MP mobilization is imperative (He et al., 2021). The critical hydrodynamic conditions of MP mobilization can be defined using either the critical depth-averaged flow velocity (U_c) or the critical shear stress (τ_c). Previous studies have shown that both

[3] The content of this chapter has been published as: Yu, Z., Loewen, M., Guo, S., Guo, Z., & Zhang, W. (2023). An investigation of the sheltering effects on the mobilization of microplastics in open-channel flow. *Environmental Science & Technology*, *57*(30), 11259-11266.

τ_c and U_c depend on the equivalent bed-grain roughness (k_s) (Waldschläger & Schüttrumpf, 2019b). It has been observed that MPs deposited on a rough bed require a higher value of τ_c or U_c to be mobilized compared to those on a smooth bed ($k_s \approx 0$) because they experienced "sheltering effects" due to the surrounding bed grains (McCarron et al., 2019; Waldschläger & Schüttrumpf, 2019b).

Our previous study investigated both τ_c and U_c values and proposed a formula for determining τ_c for MPs but the sheltering effects were not considered (chapter 3). Waldschläger and Schüttrumpf (2019b) observed that, when the nominal diameter D_n of MPs (i.e., the diameter of the volume equivalent sphere) is larger than the median size of the bed grains (D_{50}), MPs tend to move earlier than the bed grains due to their higher exposure. They proposed an empirical dimensionless formula for τ_c as a power function of the ratio of D_n/D_{50}. Their formula is valid for rough beds with D_{50} = 0.5, 1.0, 1.5, and 3 mm, but as they discussed it substantially underestimated values of τ_c for polystyrene (PS) pellets.

Apart from τ_c, it is also worthwhile to investigate the possibility of utilizing U_c to determine the flow threshold for MP mobilization while considering the sheltering effects. The formula proposed by Waldschläger and Schüttrumpf (2019b) for estimating τ_c does not include a factor that explicitly quantifies the sheltering effects. In sediment studies, various factors such as particle packing angle and hiddenness have been commonly used to represent the sheltering effects (Wu & Chou, 2003; Xu et al., 2008). These factors were used in force and moment analyses of a particle in a pre-defined position to predict the critical depth-averaged flow velocity for sediments, $U_{c,s}$ (Wu & Chou, 2003; Xu et al., 2008). Similar factors applied to sediments may work for negatively buoyant MPs, given their similarities to certain degrees in terms of physical properties and transport mechanisms (Waldschläger et al., 2022). Incorporating these factors in the development of a

method for estimating U_c could provide an alternative understanding of the sheltering effects, rather than relying solely on empirical relationships. Moreover, given that U_c is easier to measure compared to τ_c, it is considered more advantageous for engineering applications.

In this study, flume experiments were conducted to measure τ_c and U_c of MPs moving on rough beds with different D_{50} values compared with the previous study (Waldschläger & Schüttrumpf, 2019b). Polyamide (PA), polyvinyl chloride (PVC), and polyethylene terephthalate (PET) with different sizes and shapes were selected for testing, which have been commonly found in riverbeds (Boskovic et al., 2022; Kabir et al., 2022; Maheswaran et al., 2022). A new formula for estimating τ_c accounting for the sheltering effects was proposed, and the prediction accuracy was estimated by comparing it with the previous formula for predicting τ_c (Waldschläger & Schüttrumpf, 2019b). To better describe the sheltering effects, three factors from previous studies of sediments were introduced and used to perform a moment analysis on MPs. Assuming rolling is the dominant movement form for the initiation of motion (Bravo et al., 2018), a new semi-empirical method for U_c of MPs was also proposed. The proposed method for estimating U_c was verified by comparing it with the experimental data, and its performance was also compared to existing methods for predicting U_c of sediments (Bai et al., 2013; Baker, 1980).

4.2. Theoretical background

Different-sized sediment particles interact with flow in distinct ways, and only specific sizes of sediment particles are transported from a riverbed by flow (McCarron et al., 2019). Studies on mixed-size sediments (Wilcock, 1988; Wilcock, 1993) suggest that the ratio of the critical shear stress for sediments of a specific size fraction i, $\tau_{cs,i}$, to the critical shear stress of the median size

fraction (i.e., sizes ≤ D_{50}), $\tau_{cs,50}$, can be expressed as a power law function of the ratio of sediment sizes as follows:

$$\frac{\tau_{cs,i}}{\tau_{cs,50}} = \left(\frac{D_i}{D_{50}} \right)^a \tag{4-1}$$

The determination of exponent a is sensitive to the experimental dataset, and a may be a constant or a function of D_{50} (McCarron et al., 2019).

Eq. 4-1 can be expressed in the dimensionless form (Wilcock, 1988; Wilcock, 1993):

$$\frac{\Theta_{c,i}}{\Theta_{c,50}} \equiv \frac{\tau_{cs,i} \big/ (\rho_s - \rho) g D_i}{\tau_{cs,50} \big/ (\rho_s - \rho) g D_{50}} = \frac{\tau_{cs,i}}{\tau_{cs,50}} \frac{D_{50}}{D_i} = \left(\frac{D_i}{D_{50}} \right)^a \tag{4-2}$$

where ρ is the density of the ambient fluid; ρ_s is the density of sediments; $\Theta_{c,i}$ and $\Theta_{c,50}$ are the critical Shields parameters of i and median sediment size fraction, respectively (Wilcock, 1988; Wilcock, 1993). Based on Eq. 4-2, Waldschläger and Schüttrumpf (2019b) proposed the following formula for uniform MPs moving on a sediment bed:

$$\frac{\Theta_c}{\Theta_{c,50}} \equiv \frac{\tau_c \big/ (\rho_p - \rho) g D_n}{\tau_{cs,50} \big/ (\rho_s - \rho) g D_{50}} = 0.5588 \left(\frac{D_n}{D_{50}} \right)^{-0.503} \tag{4-3}$$

where Θ_c is the critical Shields parameters of the uniform MPs.

To calculate the critical shear stress τ_c of the uniform MPs, Eq. 4-3 can be rewritten as:

$$\frac{\tau_c}{\tau_{cs,50}} = 0.5588 \frac{(\rho_p - \rho)}{(\rho_s - \rho)} \left(\frac{D_n}{D_{50}} \right)^{0.497} \tag{4-4}$$

The formula for calculating $\tau_{cs,50}$ was provided in Waldschläger and Schüttrumpf (2019b).

Particle packing angle θ is one of the commonly used factors to represent the degree of hiddenness for sediments, also known as the friction angle. It is defined as the angle between the line crossing the centers of the surface particle and sub-surface particle and the vertical line crossing the center of the surface particle (Baker, 1980; Marsh et al., 2004), as illustrated in Figure 4-1a. The particle packing angle θ may vary from 0° to 90°, and higher values of θ indicate that a particle on the bed is hidden to a greater degree (Figure 4-1a). For different packing angles, Baker (1980) derived a formula for sediment particles to predict the critical flow velocity, which is referred to as the near-bed velocity, u_b:

$$u_b^2 = \frac{4}{3} \frac{\sin(\theta - \varepsilon)(\rho_p - \rho) g D_i}{\rho (C_L \sin\theta + C_D \cos\theta)} \tag{4-5}$$

where ε is the bed slope; C_D is the drag coefficient from terminal settling velocity measurements (Marsh et al., 2004); and C_L is the lift coefficient (Marsh et al., 2004). The near-bed velocity u_b can be converted to a critical depth-averaged flow velocity for sediments, $U_{c,s}$, using:

$$U_{c,s} = u_b \frac{\log\left(12.27 \frac{h}{y_0} \right)}{\log\left(30.2 \frac{D_i / 2}{y_0} \right)} \tag{4-6}$$

where h is the flow depth; $y_0 = D_{50}/\chi$ is the effective roughness parameter (Marsh et al., 2004) and χ is the correction factor for D_{50}, as given in Rao and Kumar (2009).

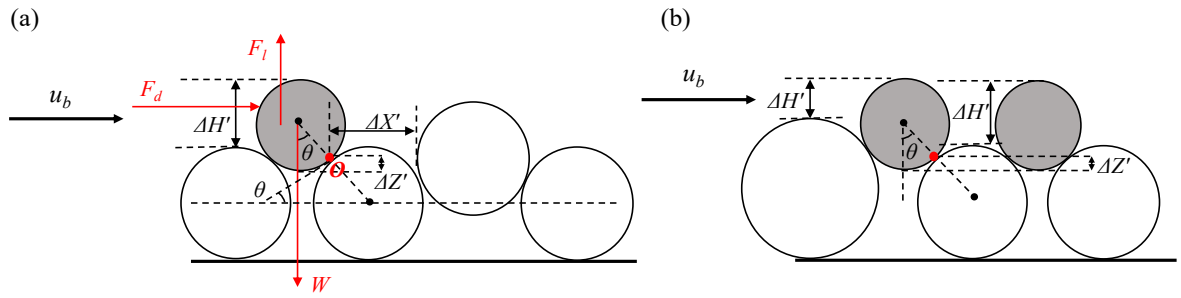

Figure 4-1 Schematic diagram of the characteristics of hidden MPs (gray) with uniform size (a) and non-uniform size bed grains (b). Bed grains are denoted by white circles.

The vertical distance between the lowest point of the particle and its contact point O with the immediate downstream neighbor is defined as $\Delta Z'$, as shown in Figure 4-1 (Bai et al., 2013). It can be seen that $\Delta Z'$ quantifies how much of the particle is sitting below the contact point O or how much of the particle is sheltered from the flow. Bai et al. (2013) incorporated $\Delta Z'$ in an empirical formula for sediments to predict $U_{c,s}$, as follows:

$$U_{c,s} = 0.715\left(\frac{h}{D_i}\right)^{1/\left(4+\lg\frac{h}{D_i}\right)} \sqrt{\frac{\frac{4}{3}gD_i\frac{\rho_p-\rho}{\rho}\sqrt{\Delta Z'\left(D_i-\Delta Z'\right)}}{C_D\left(\frac{2}{3}D_i-\Delta Z'\right)+C_L\left[\frac{1}{6}D_i+\sqrt{\Delta Z'\left(D_i-\Delta Z'\right)}\right]}} \tag{4-7}$$

However, if the bed is formed by multiple layers or non-uniform particles, as shown in Figure 4-1b, for the same magnitude of $\Delta Z'$, the upstream particle (grey) is more sheltered from the flow compared to the downstream particle. Therefore, $\Delta Z'$ does not fully reflect the sheltering effects, and the exposure height $\Delta H'$ needs to be introduced (Kirchner et al., 1990; Xu et al., 2008). $\Delta H'$ is defined as the vertical distance between the highest point of a particle and the top of the immediate upstream underlying particle (Kirchner et al., 1990; Xu et al., 2008), as shown in Figure 4-1. $\Delta H'$ quantifies how much of the particle is exposed to the flow in the vertical direction.

Bai et al. (2013) found that the mobilization of a sediment particle can be influenced by the adjacent downstream surface particle while the influence of the upstream particle could be neglected. Specifically, as the flow passes a hidden particle, a backflow can be created due to the downstream particle if the streamwise gap $\Delta X'$ is $\leq 0.5D_i$, which affects the forces acting on the hidden particle. $\Delta X'$ is defined as the longitudinal distance between the contact point O and the upstream edge of the downstream surface particle, as shown in Figure 4-1a, and reflects the degree of exposure in the streamwise direction.

Based on these previous sediment transport studies (Bai et al., 2013; Dey & Ali, 2017; Xu et al., 2008), the three distances ($\Delta Z'$, $\Delta H'$, and $\Delta X'$) were selected to quantify the effect of the degree of hiddenness and exposure of MPs. $\Delta Z'$, $\Delta H'$, and $\Delta X'$ can be made dimensionless by dividing by D_n, and they are defined as the hiddenness (ΔZ), exposure (ΔH), and longitudinal exposure (ΔX) (He & Han, 1982). Note that ΔZ, ΔH, and ΔX have commonly been found to follow normal distributions in sediment studies (Bai et al., 2013; He & Han, 1982).

4.3. Materials and methods

4.3.1. Materials and measurement of ΔH', ΔZ', and ΔX'

MP particles made of PA, PVC, and PET were selected for testing in this study. Images of each type of MPs are presented in Figure 4-2. The MPs were uniform in size and the nominal diameters, D_n, of PA, PVC, and PET were 3.2, 4.2, and 2.8 mm, respectively. The densities of PA, PVC, and PET range from 1.20 to 1.41 g/cm^3, determined using the titration method (Yang et al., 2023). The shape of MPs was quantified using Corey's shape factor (CSF), defined as $c/(ab)^{1/2}$, where a, b, and c represent the lengths of the longest, intermediate, and shortest sides of a particle, respectively.

The *CSF* ranged from 0.66 to 0.89 for PA, PVC, and PET. Detailed information on the selected MPs is provided in Table 4-1.

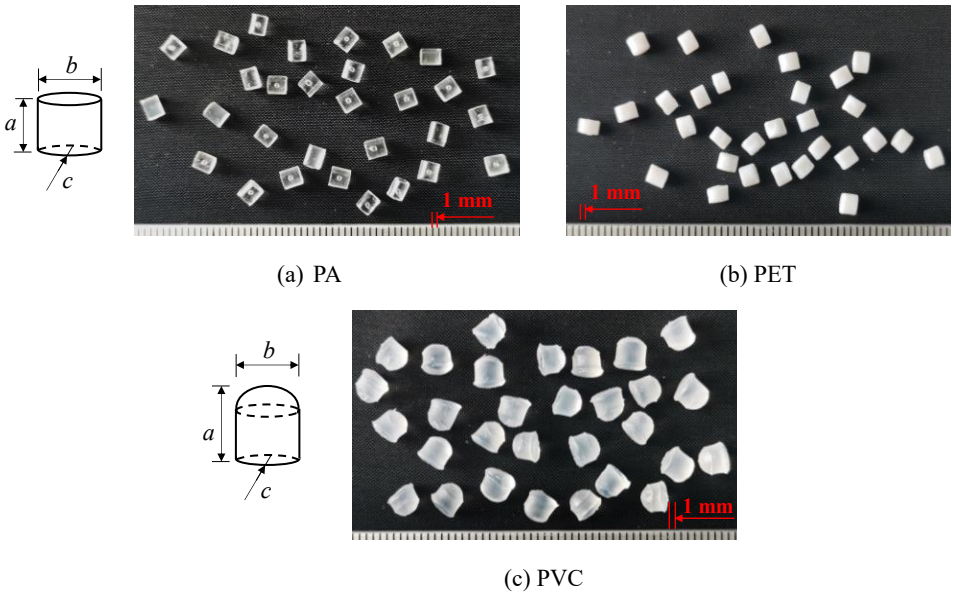

(a) PA (b) PET

(c) PVC

Figure 4-2 Photos of MPs used in the experiments: PA (a); PET (b); and PVC (c).

Table 4-1 Summary of the selected MP properties, flow thresholds, and bed characteristics. I and II represent the bed grain sizes of 2.5 and 5.0 mm, respectively.

Case	D_n (mm, ± 0.3)	ρ_p (g/cm^3, ± 0.01)	*CSF*	D_{50} (mm)	τ_c (N/m^2)	U_c (cm/s)	k_s^+
PA-I	3.2	1.20	0.66	2.5 ± 0.1	0.12 ± 0.03	19.22 ± 1.02	27
PVC-I	4.2	1.25	0.89	2.5 ± 0.1	0.11 ± 0.03	18.57 ± 1.70	26
PET-I	2.8	1.41	0.74	2.5 ± 0.1	0.15 ± 0.03	23.82 ± 1.25	31
PA-II	3.2	1.20	0.66	5.0 ± 0.2	0.22 ± 0.05	24.82 ± 0.97	74
PVC-II	4.2	1.25	0.89	5.0 ± 0.2	0.21 ± 0.06	24.11 ± 2.17	72
PET-II	2.8	1.41	0.74	5.0 ± 0.2	0.35 ± 0.06	32.62 ± 1.62	94

A simple method for estimating $\Delta H'$, $\Delta Z'$, and $\Delta X'$ was developed based on a previously reported method of determining $\Delta H'$ and θ for sediments (Kirchner et al., 1990; Yang et al., 2009). The

method is designed to simulate cases where MPs are mixed into the bed sediments while others are deposited randomly on top of the riverbed. A small quantity of each of the three types of MPs was thoroughly mixed into a container of either 2.5 ± 0.1 or 5.0 ± 0.2 mm glass beads of density 2.57 g/cm^3, to create six different mixtures. The average MP abundance in each mixture was 300 particles/kg, which falls within the MP abundance range of 0-500 particles/kg detected in riverbeds and is close to the average (Boskovic et al., 2022; Harris, 2020; Kabir et al., 2022; Maheswaran et al., 2022; Yang et al., 2021; Zhang et al., 2020).

One kilogram of the selected MPs-glass beads mixture was poured into a transparent acrylic box (1000 × 9 × 500 mm) using a beaker (Figure 4-3a). Care was taken to ensure that the surface of the mixture in the box was approximately flat. If no MPs were visible on top of the bed, the box was emptied, and the aforementioned steps were repeated until at least one particle was observed on the bed. A digital camera (Sony DSC-HX200V) was placed 10 cm away from the box's side, and the lens' center was kept at the same level as the mixture surface. Digital images of MPs deposited on the surface were taken as shown in Figure 4-3b. The photos were imported into *Image J* to measure $\Delta H'$, $\Delta Z'$, and $\Delta X'$ (Schneider et al., 2012). After the first image was taken, the box was emptied, and the above steps were repeated approximately 90 times for all six mixtures resulting in 1101, 1101, and 737 measurements of $\Delta H'$, $\Delta Z'$, and $\Delta X'$, respectively.

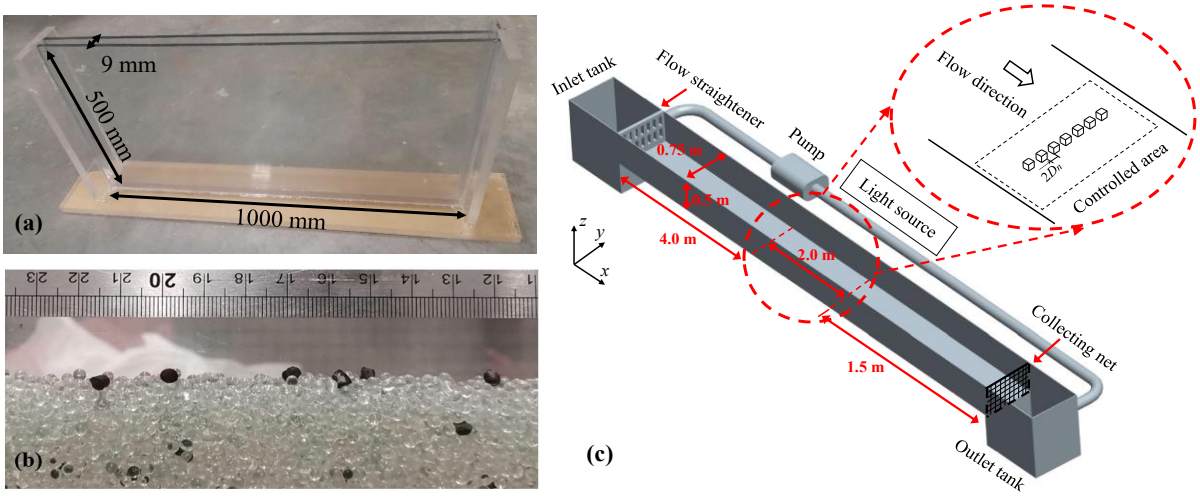

Figure 4-3 Photos of the experimental setup for measuring $\Delta H'$, $\Delta Z'$, and $\Delta X'$ (a), an example of the PVC-I mixture (b), and the sketch of the flume (c).

Statistical analyses were performed using SPSS 22.0 on ΔH, ΔZ, and ΔX. The analysis of variance (one-way ANOVA) for the same size of bed grains and the paired t-tests for the same MP material, were used to test the significance of differences in mean values to study the impacts of MP materials on the probability density functions (PDFs) of ΔH, ΔZ, and ΔX. The PDFs were obtained using Origin 9.0.

4.3.2. Measurement of critical flow velocities and shear velocities of MPs

The critical flow velocities and shear velocities of three types of MP particles (PA, PVC, and PET) were measured over two rough beds consisting of glass beads with D_{50} = 2.5 or 5.0 mm, i.e., in a total of six experimental cases (Table 4-1). The rough beds were created by gluing glass beads with a cyanoacrylate-based adhesive onto a 2 mm-thick, 0.75 m-wide, and 2 m-long stainless-steel base plate. Care was taken to ensure that the bed surface was approximately flat. The experiments were conducted in a 7.50 m-long, 0.75 m-wide, and 0.50 m-deep recirculating flume with a slope of 0.2%, featuring glass sidewalls and a bottom to facilitate visualization (Figure 4-3c). The flow

was generated by a pump equipped with a variable frequency drive with a maximum flow rate of 150 L/s and a resolution of 1.31 L/s. Flow rates were measured with a magnetic flow meter. The flow depth was kept constant at $h = 30.0 \pm 0.5$ cm using an adjustable tailgate. At the upstream end of the flume, the water passed through a flow straightener to reduce lateral velocities and make the velocity distribution more uniform. The experimental section was 2.0 m long and located 4.0 m downstream of the flume entrance.

The critical depth-averaged velocity U_c was measured using the method described in chapter 3. First, 20 to 25 particles were placed at rest on the bed of the experimental section with a spacing of $2D_n$ and located 0.18 to 0.28 m from the flume side walls. The flow rate was gradually increased using the variable frequency drive of the pump. As the flow rate increased, the initiation of MP motion was recorded with a digital camera (60 fps, Sony DSCHX200V). The critical depth-averaged velocity U_c was defined as the value when 50% of the particles moved away from the controlled area (chapter 3). Measurements of U_c for a particular type of MPs were repeated 5 to 7 times and the values were averaged.

Velocity measurements were conducted with a Nortek Vectrino Acoustic Doppler Velocimeter (ADV). The time series of all three velocity components were recorded at 0.1 of the total water depth above the bed at the midpoint of the experimental section (Biron et al., 2004). Previous measurements showed that the bed shear stress did not vary significantly laterally ± 22.5 cm from the channel centerline (chapter 3). The measurement period at each measurement point was 300 s, and the sampling frequency was 100 Hz. Velocity data were filtered out when the correlation was lower than 85% and the signal-to-noise ratio was lower than 25 dB (Goring & Nikora, 2002). At the critical depth-averaged velocity, the critical bed shear stress τ_c was calculated from the velocity

data using the 3-D turbulent kinetic energy method, which has been widely used on rough beds (Wang et al., 2016):

$$\tau_c = 0.5C\rho(\overline{u'^2} + \overline{v'^2} + \overline{w'^2}) \quad (4\text{-}8)$$

where u', v', and w' are the streamwise, lateral, and vertical velocity fluctuation components, respectively; C is a proportionality constant assumed to be 0.19 (Wang et al., 2016); and the overbar denotes a time-average over the 300 s measurement duration. The critical shear velocity u_{*c} was then calculated as $(\tau_c/\rho)^{0.5}$.

Values of the roughness Reynolds number, defined as $k_s^+ = u_{*c}k_s/\nu$, where ν is the kinematic viscosity of water, and k_s was assumed to be D_{50} for uniform bed grains (Marsh et al., 2004), are presented in Table 4-1. The bed constructed with 2.5 mm glass beads can be characterized as transitionally rough because k_s^+ ranged from 26 to 31 which is below the fully rough limit of 70. However, flows over the bed with 5.0 mm glass beads were hydraulically rough because k_s^+ ranged from 72-94.

4.4. Results and discussion

4.4.1. Estimation of the critical shear stress of MPs

Figure 4-4a presents the relationship between $\tau_c/\tau_{cs,50}$ and D_n/D_{50} for mobilizations of MPs on rough beds, using data obtained from this study and previous ones (Waldschläger & Schüttrumpf, 2019b; Yu, Yao, et al., 2022). The plot generally confirms the existence of a power law relationship between $\tau_c/\tau_{cs,50}$ and D_n/D_{50} (black line), which was reported in previous sediment and MPs studies (Waldschläger & Schüttrumpf, 2019b; Yu, Yao, et al., 2022). Approximately 70% of the data points, enclosed within a black elliptical boundary in Figure 4-4a, clustered around the best-fit line

[$\tau_c/\tau_{cs,50} = 0.075(D_n/D_{50})^{0.62}$], with a coefficient of determination $R^2 = 0.78$. However, it was also observed that the power law did not apply to all the MP cases, with approximately 30% of the data points scattered below the fit line (enclosed within a red elliptical boundary in Figure 4-4a). The scatter of the data in Figure 4-4a could be attributed to the varying densities of MPs in the dataset which ranged from 1008 to 1400 kg/m^3. To account for the impact of the density of MPs, the relative density of MPs, $(\rho_p - \rho)/\rho$, is commonly used (Waldschläger & Schüttrumpf, 2019b; Yu, Yao, et al., 2022). It was found that the data points with $(\rho_p - \rho)/\rho \geq 0.11$ are enclosed within the black elliptical boundary, while the data points with $(\rho_p - \rho)/\rho < 0.11$ fall within the red elliptical boundary. Therefore, $\tau_c/\tau_{cs,50}$ may be influenced by both D_n/D_{50} and $(\rho_p - \rho)/\rho$.

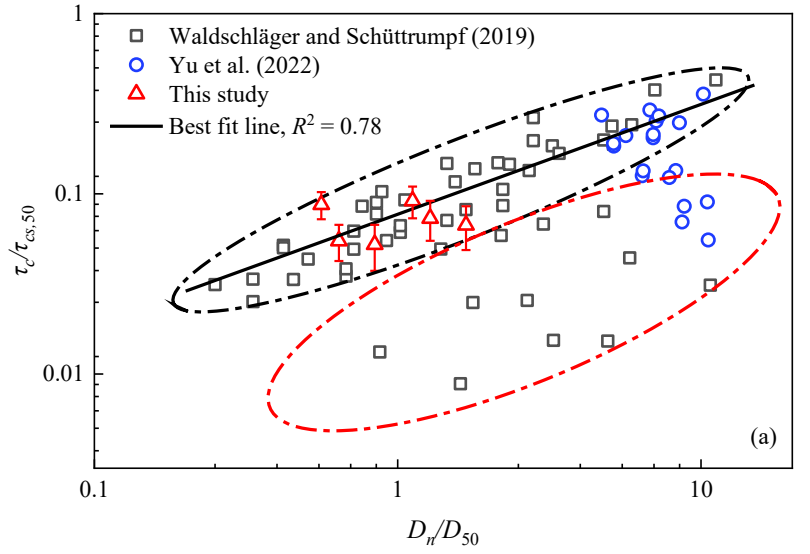
Waldschläger and Schüttrumpf (2019)
Yu et al. (2022)
This study
Best fit line, R^2 = 0.78
$\tau_c/\tau_{cs,50}$
D_n/D_{50}
(a)

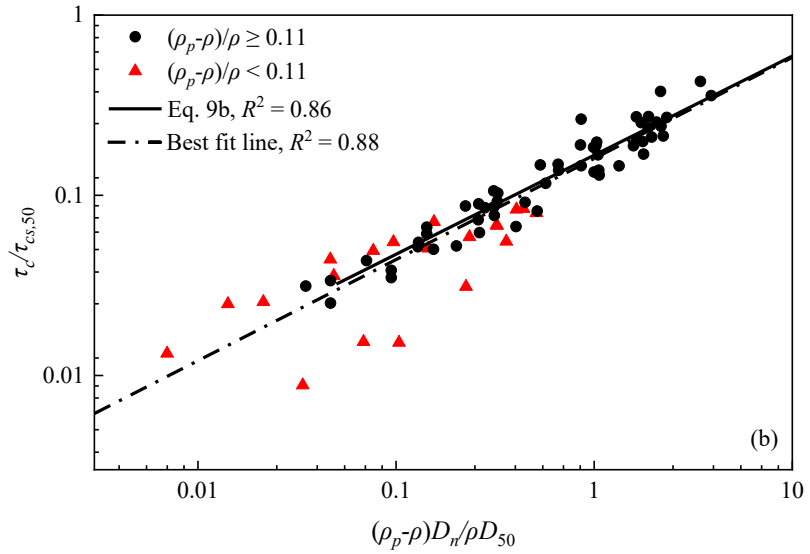
$(\rho_p-\rho)/\rho \geq 0.11$
$(\rho_p-\rho)/\rho < 0.11$
Eq. 9b, R^2 = 0.86
Best fit line, R^2 = 0.88
$\tau_c/\tau_{cs,50}$
$(\rho_p-\rho)D_n/\rho D_{50}$
(b)

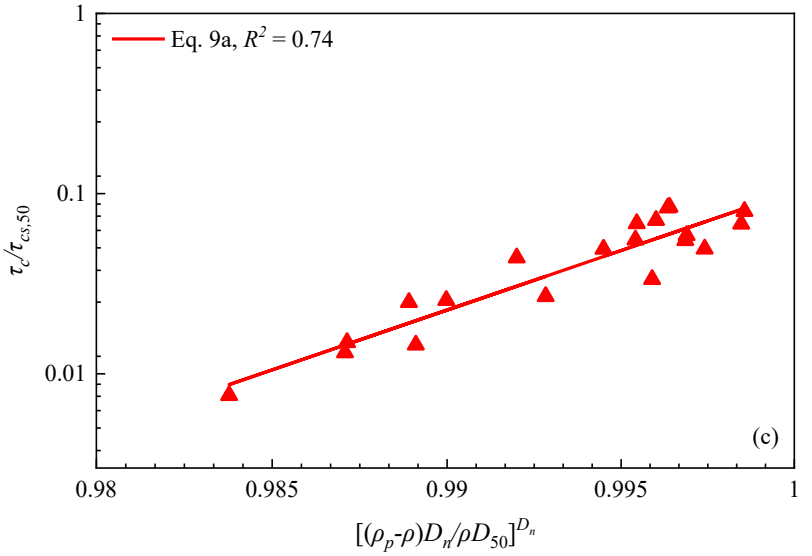
Eq. 9a, R^2 = 0.74
$\tau_c/\tau_{cs,50}$
$[(\rho_p-\rho)D_n/\rho D_{50}]^{D_n}$
(c)

Figure 4-4 The ratio of the critical shear stress of MPs to the critical shear stress of bed grains $\tau_c/\tau_{cs,50}$ versus the normalized MP properties: D_n/D_{50} (a); $(\rho_p - \rho)D_n/\rho D_{50}$ (b); and $[(\rho_p - \rho)D_n/\rho D_{50}]^{Dn}$ (c). The data points with $(\rho_p - \rho)/\rho < 0.11$ are enclosed within a red elliptical boundary, while those with $(\rho_p - \rho)/\rho \geq 0.11$ are enclosed within a black elliptical boundary. The black line in (a) denotes the best fit equation between $\tau_c/\tau_{cs,50}$ and D_n/D_{50} for $(\rho_p - \rho)/\rho \geq 0.11$. The dash-dotted line in (b) denotes the best fit equation between $\tau_c/\tau_{cs,50}$ and $(\rho_p - \rho)D_n/\rho D_{50}$ for the entire range of relative densities of MPs.

This hypothesis was confirmed by conducting a multivariable linear regression on $\tau_c/\tau_{cs,50}$, D_n/D_{50}, and $(\rho_p - \rho)/\rho$. The regression results indicated a strong dependence of $\tau_c/\tau_{cs,50}$ on D_n/D_{50} and $(\rho_p - \rho)/\rho$, with a high statistical significance (*P-values* < 0.001). The relationship between $\tau_c/\tau_{cs,50}$ and $(\rho_p - \rho)D_n/\rho D_{50}$ plotted in Figure 4-4b shows a clear power law relationship with $R^2 = 0.88$ and an exponent of 0.57 (dash-dotted best fit line). However, despite a high R^2 value, using the best fit power law does not provide accurate estimates of τ_c for some of the lower density data. The average relative error of the best fit power law equation when applied to data with $(\rho_p - \rho)/\rho < 0.11$ is 55.4% which is rather high. Therefore, it might be possible to reduce the error by fitting a modified power law equation to the data points with $(\rho_p - \rho)/\rho < 0.11$. Previous sediment studies have proposed that the exponent is a function of the nominal diameter (Shvidchenko et al., 2001; Wilcock & Crowe, 2003) and this may also be the case for low density MPs. Figure 4-4c displays a plot of $\tau_c/\tau_{cs,50}$ versus $[(\rho_p - \rho)D_n/\rho D_{50}]^{Dn}$, along with a best fit power law equation for predicting $\tau_c/\tau_{cs,50}$ ($R^2 = 0.74$) that reduces the average relative error significantly to 21.7%.

Therefore, the proposed new equations for predicting τ_c are given by:

$$\begin{cases} \dfrac{\tau_c}{\tau_{cs,50}} = 0.103\left[\dfrac{(\rho_p-\rho)D_n}{\rho D_{50}}\right]^{150.98D_n} & \dfrac{(\rho_p-\rho)}{\rho} < 0.11 \quad \text{(4-9a)} \\ \dfrac{\tau_c}{\tau_{cs,50}} = 0.166\left[\dfrac{(\rho_p-\rho)D_n}{\rho D_{50}}\right]^{0.562} & \dfrac{(\rho_p-\rho)}{\rho} \geq 0.11 \quad \text{(4-9b)} \end{cases}$$

Eq. 4-9a has $R^2 = 0.74$ (Figure 4-4c) and Eq. 4-9b has $R^2 = 0.86$ (Figure 4-4b). Eqs. 4-9a-b perform better in predicting τ_c compared to Eq. 4-4 from the previous MP study (Waldschläger & Schüttrumpf, 2019b). The average relative errors for Eqs. 4-9a-b are 21.7% and 15.8%, respectively; while the relative error for Eq. 4-4 is 35.8% for $(\rho_p - \rho)/\rho < 0.11$, and 24.4% for $(\rho_p - \rho)/\rho \geq 0.11$. Note that in Eq. 4-4, a different dimensionless form of the relative density of MPs, $(\rho_p - \rho)/(\rho_s - \rho)$, was used. Eqs. 4-9a-b can be also expressed in the form of $(\rho_p - \rho)/(\rho_s - \rho)$ since $(\rho_p - \rho)/(\rho_s - \rho) = (\rho_p - \rho)/1.65\rho$. One possible reason for the larger errors in Eq. 4-4 is that a linear relationship between $\tau_c/\tau_{cs,50}$ and $(\rho_p - \rho)/(\rho_s - \rho)$ was assumed, which may not be the case as shown in Figure 4-4b&c. Eqs. 4-9a-b can be applied with confidence to predict τ_c for MPs with various shapes (CSF = 0.2-1.0) and a wide range of ρ_p = 1008-1400 kg/m^3 and D_n = 0.75-5.04 mm moving on a rough bed with D_{50} = 0.5-5.0 mm. However, in the case of riverbeds with D_{50} values beyond the studied range or complex conditions such as widely graded bed grain size distributions or cohesive beds, the exponents in Eqs. 4-9a-b should be re-evaluated (Frings, 2008; Gomez, 1994; McCarron et al., 2019).

Eqs. 4-9a-b shows that $\tau_c/\tau_{cs,50}$ is positively correlated with $(\rho_p - \rho)D_n/\rho D_{50}$, but it only accounts for the sheltering effects in a simplistic way via the relative density and the ratio D_n/D_{50}. Including the exposure (ΔH), hiddenness (ΔZ), and longitudinal exposure (ΔX) to account for the sheltering effects might be a better approach. Therefore, an alternative method that employs these measures

to predict the mobilization of MPs, that is based on the critical depth-averaged velocity U_c, was developed.

4.4.2. Exposure (ΔH), hiddenness (ΔZ), and longitudinal exposure (ΔX)

Figure 4-5a shows the probability density of ΔH from all six bead-MPs mixtures, within the range of 0-1.2, corresponding to MPs being fully hidden or exposed. All the mixtures had an upper limit of $\Delta H > 1$, reflecting the irregularity of MP shapes. Similar results were observed for ΔZ and ΔX, which were also fitted with normal distributions (Figure 4-5b&c). Statistical analysis showed that the mean values of ΔH, ΔZ, and ΔX had no statistically significant differences across the mixtures based on ANOVA and t-test results (*P-values* > 0.05).

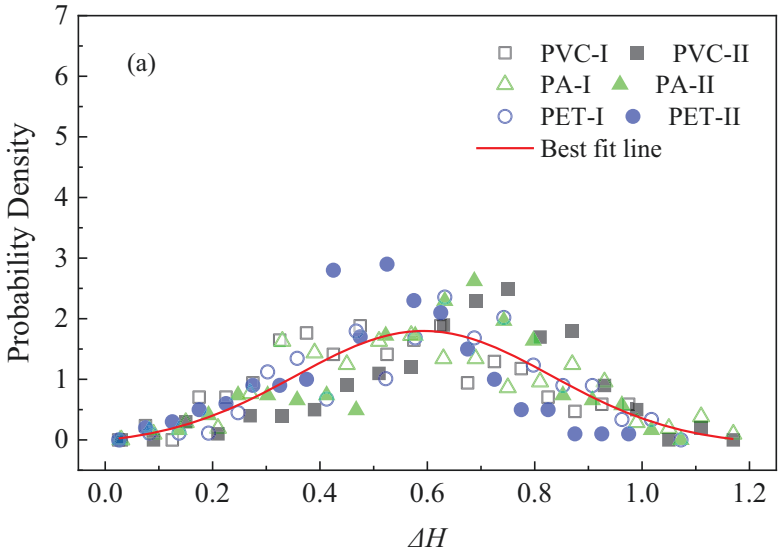
(a)
PVC-I
PVC-II
PA-I
PA-II
PET-I
PET-II
Best fit line
Probability Density
ΔH

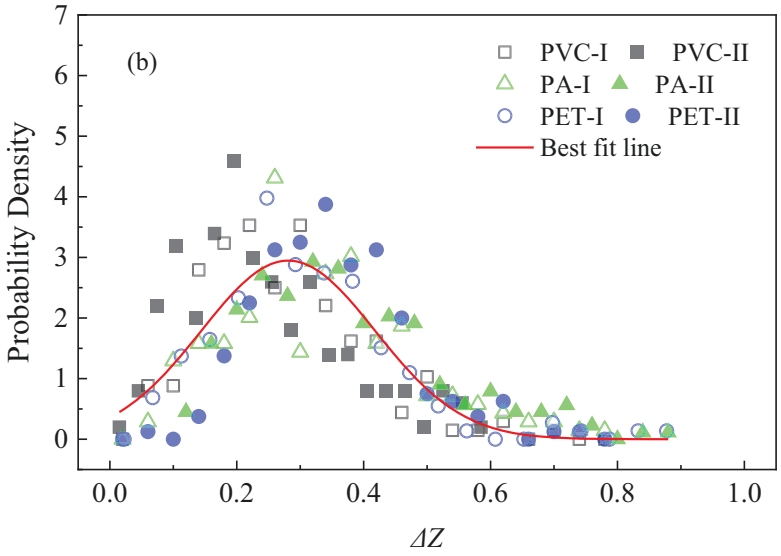
(b)
PVC-I
PVC-II
PA-I
PA-II
PET-I
PET-II
Best fit line
Probability Density
ΔZ

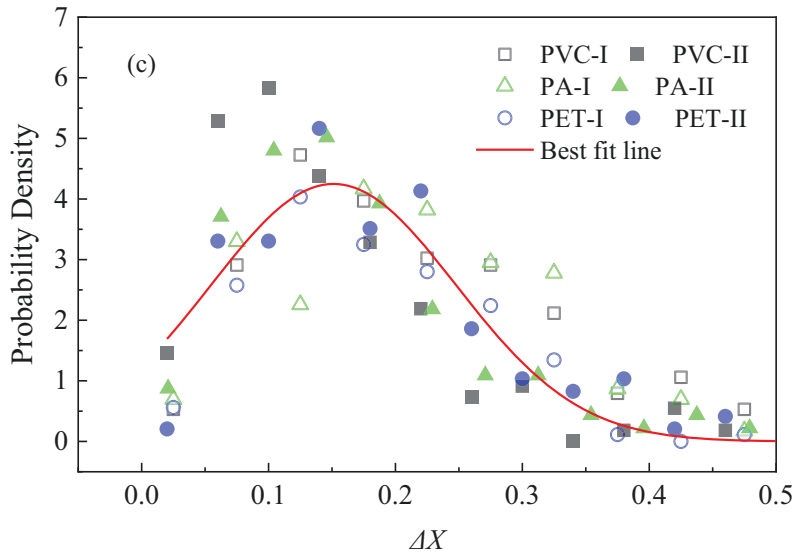
(c)
PVC-I
PVC-II
PA-I
PA-II
PET-I
PET-II
Best fit line
Probability Density
ΔX

Figure 4-5 The probability densities of ΔH (a), ΔZ (b), and ΔX (c) data for all six mixtures, and the red lines are fitted normal distributions.

The normal PDFs for ΔH, ΔZ, and ΔX, with R^2 values of 0.72, 0.75, and 0.77, respectively are given by:

$$f(\Delta H) = \frac{1.03}{0.45\sqrt{\frac{\pi}{2}}} e^{\left[-2\left(\frac{\Delta H - 0.60}{0.45}\right)^2\right]} \qquad (0 < \Delta H < 1.2) \tag{4-10a}$$

$$f(\Delta Z) = \frac{1.01}{0.27\sqrt{\frac{\pi}{2}}} e^{\left[-2\left(\frac{\Delta Z - 0.28}{0.27}\right)^2\right]} \qquad (0 < \Delta Z < 0.9) \tag{4-10b}$$

$$f(\Delta X) = \frac{1.03}{0.19\sqrt{\frac{\pi}{2}}} e^{\left[-2\left(\frac{\Delta X - 0.16}{0.19}\right)^2\right]} \qquad (0 < \Delta X < 0.5) \tag{4-10c}$$

These results show that the hiddenness and exposure of MPs tend to follow normal distributions, similar to sediments (He & Han, 1982; Kirchner et al., 1990). One potential explanation for this phenomenon is that MPs and sediments are distributed in discrete clusters on the surface of bed grains. As a result, the distributions of ΔH, ΔZ, and ΔX may follow the central limit theorem and normal distributions for a large sample size.

4.4.3. Estimation of the critical depth-averaged velocity of MPs

A force analysis of MPs was conducted first to obtain the critical depth-averaged velocity U_c. The shape of a MP particle is assumed to be spherical. MPs with ΔH or ΔZ values > 0, on the verge of mobilization, are acted upon by three forces as shown in Figure 4-1a: the drag force F_D, the lift force F_L, and the submerged weight W. Paintal (1971) posited that the hydrodynamic forces acting

on a particle are related to the degree of hiddenness of the particle. They assumed that there are linear relationships between F_D and ΔH, as well as F_L and ΔH (Paintal, 1971). Therefore, taking ΔH into consideration, F_D and F_L acting on a MP particle can be written as:

$$F_D = \frac{C_D \rho}{2} u_b^2 \frac{\pi D_n^2}{4} \Delta H \tag{4-11a}$$

$$F_L = \frac{C_L \rho}{2} u_b^2 \frac{\pi D_n^2}{4} \Delta H \tag{4-11b}$$

where C_L is the lift coefficient and it is assumed to be 0.88 C_D (Armanini & Gregoretti, 2005). Using a numerical simulation, Bai et al. (2013) reported that C_D of spherical particles was primarily influenced by ΔX, and C_D can be expressed as:

$$C_D = -1.31 + 23.23\Delta X - 70.04\Delta X^2 + 67.34\Delta X^3 \tag{4-12}$$

Assuming F_D and F_L act horizontally and vertically at points that are a distance of $D_n/6$ from the particle center (Bai et al., 2013), summing moments around point O in Figure 4-1a provides the following equation:

$$F_D\left(\frac{1}{6}+\frac{1}{2}\cos\theta\right)D_n + F_L\left(\frac{1}{6}+\frac{1}{2}\sin\theta\right)D_n - W(\frac{1}{2}\sin\theta)D_n = 0 \tag{4-13}$$

where $\cos(\theta) = 1 - 2\Delta Z$ and $\sin(\theta) = 2(\Delta Z - \Delta Z^2)^{0.5}$, which are valid under the assumptions that the MP particles are spherical and uniform in size (Bai et al., 2013). By combining Eqs. 4-11a-b, 4-12, and 4-13, describing $\cos(\theta)$ and $\sin(\theta)$ as functions of ΔZ, the near-bed velocity can be expressed in this analytic form:

$$u_b^2 = \frac{8gD_n(\frac{\rho_p}{\rho}-1)(\Delta Z-\Delta Z^2)^{0.5}}{C_D\Delta H(4-6\Delta Z)+C_L\Delta H(1+6(\Delta Z-\Delta Z^2)^{0.5})} \tag{4-14}$$

Compared with u_b, the critical depth-averaged flow velocity U_c is more easily measurable and suitable for engineering applications (Cheng et al., 2022). Cheng et al. (2022) found that the relationship between U_c and u_b can be expressed as:

$$\frac{U_c}{u_b} = \frac{\frac{1}{h}\int_0^h\left[\left(u_{*c}y/\nu\right)^{-3}+\left(2.5\ln\left(1+y/y_o\right)\right)^{-3}\right]^{-1/3}dy}{\left[\left(u_{*c}y_b/\nu\right)^{-3}+\left(2.5\ln\left(1+y_b/y_o\right)\right)^{-3}\right]^{-1/3}} \tag{4-15}$$

where y_b is the height above the bed where u_b acts and y_o the hydrodynamic roughness height is given by:

$$y_o = 0.11\frac{\nu}{u_{*c}} + 0.033D_{50}\left[1-\exp\left(-0.04\frac{D_{50}u_{*c}}{\nu}\right)\right] \tag{4-16}$$

The near-bed flow velocity u_b was assumed to act at $2D_n/3$ above the bed surface and then $y_b = 2D_n/3$ (Bai et al., 2013). To calculate U_c using the new method, Eqs. 4-12 and 4-14 should be combined to obtain u_b. In this study, only the expected values of ΔH, ΔZ, and ΔX, were used to quantify the average impact of the sheltering effects in Eq. 4-14 to better evaluate the new method against measurements of U_c. The expected values of ΔH (0.58), ΔZ (0.28), and ΔX (0.16) can be obtained by integrating their respective PDFs (Eqs. 4-10a-c). This approach is commonly used in practical applications of sediment studies (Armanini & Gregoretti, 2005; Bai et al., 2013; Baker, 1980). Finally, u_b, h, y_b, y_o, ν and u_{*c} were substituted into Eq. 4-15 to obtain U_c.

Figure 4-6 compares the performance of the proposed new method and sediment methods (Eqs. 4-5, 4-6, and Eq. 4-7) (Bai et al., 2013; Baker, 1980) in predicting U_c values for MPs. The U_c values predicted using Eq. 4-15 are consistently close to the observed values and all the data points are within the ±15% error lines. The new method has a low relative error (7.4%) and *RMSE* (8.9%) which indicates that the new method provides accurate predictions of U_c for the selected MPs. As a comparison, the sediment method proposed by Baker (1980) (Eqs. 4-5 and 4-6) has a higher relative error (28.1%) and *RMSE* (35.3%). This may be because Baker (1980) only considered θ, which can be expressed as a function of ΔZ, and this may not fully account for the sheltering effects for MPs. In addition, C_d derived from MP settling was considered in Eq. 4-5, which may not accurately represent the near-bed movement of MPs under the sheltering effects. Eq. 4-7 proposed by Bai et al. (2013) underestimates U_c for MPs by 31% on average, which is expected because this semi-empirical formula developed for sediments is not applicable to MPs and it only accounts for ΔZ and ΔX.

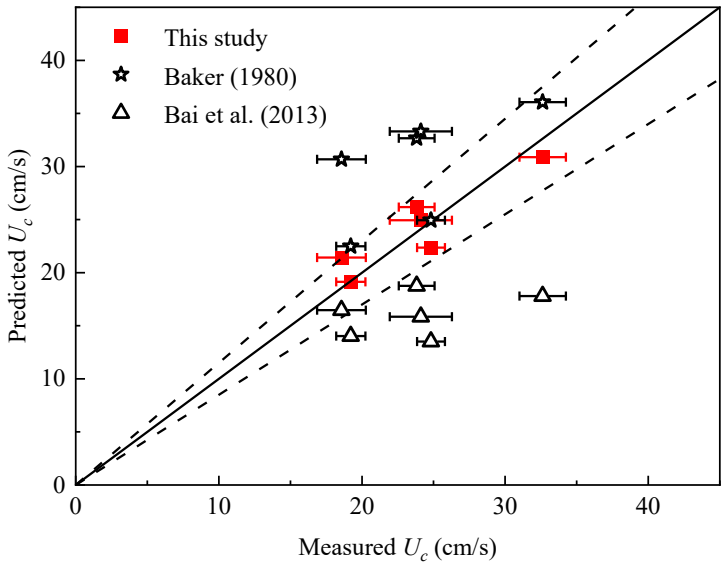

Figure 4-6 Comparisons of the experimentally observed and predicted U_c with the new method for MPs and sediment methods (Baker, 1980; Bai et al., 2013). The solid line indicates the cases where

the prediction matches perfectly with the experimental data. The dashed lines represent the ±15% error lines. The error bars indicate +/- the standard deviation of the observed U_c values.

The proposed factors (ΔH, ΔZ, and ΔX) for quantifying the sheltering effects and the method for estimating U_c have been shown to be accurate under the idealized conditions in this study, which involve MPs with limited ranges of particle properties (ρ_p = 1.2-1.4 g/cm^3, D_n = 2.8-4.2 mm, and CSF = 0.7-0.9) and on a fixed uniform bed with D_{50} = 2.5-5.0 mm. Further investigations are needed to examine and improve their applicability to more realistic scenarios in natural rivers. These scenarios may involve riverbeds with complex bed characteristics, such as non-uniform beds or cohesive beds, and/or the presence of MPs with physical properties outside the studied range [e.g., MPs with elongated or flexible shapes, or bio-filmed MPs (Kaiser et al., 2017; Zhou et al., 2020)].

Specifically, in scenarios with complex bed characteristics, while ΔH, ΔZ, and ΔX are expected to still be the appropriate parameters for quantifying the sheltering effects (Kirchner et al., 1990; Xu et al., 2008), the PDFs and expected values measured in this study may not be representative. Additionally, alternative measures should be explored for MPs with specific shapes, such as fiber-like MPs, ΔH, ΔZ, and ΔX may not be appropriate. Furthermore, although the proposed method for estimating U_c was shown to be accurate for the idealized and limited range of conditions by assuming C_d and C_l as functions of ΔX, further investigations on the estimation of C_d and C_l are needed. Currently, there is a lack of experimental or theoretical investigations on the methods for predicting C_d and C_l for the near-bed movement of MPs under more realistic scenarios. In addition, the analysis of forces and moments should be repeated for more complex scenarios. For example, MPs embedded or trapped within cohesive beds may require stronger flow conditions for mobilization (Grabowski et al., 2011), requiring additional forces to account for the adhesion

between MPs and bed materials. Lastly, current techniques and experimental setups employed to measure the sheltering effects and U_c values can be refined. For instance, the use of glass beads as a substitute for natural sediment in this study may overlook potential differences in roughness characteristics in these two cases.

The goal of this study was to investigate the mobilization of MPs on rough bed open channels including the sheltering effects. A power law relationship between τ_c and MP properties (size and density) was found, and a new formula for estimating τ_c was proposed (Eq. 4-9), which reduced the average relative error from 27.4% to 17.4%. Additionally, ΔH, ΔZ, and ΔX were introduced to explicitly quantify the sheltering effects, and a new semi-empirical method for estimating U_c was proposed (Eqs. 4-14, 4-15, and 4-16). The method for estimating U_c provides an alternative to the method for estimating τ_c that relies solely on empirical relations to investigate the initiation of MP mobilizations.

5. Continuous near-bed movements of microplastics in open channel flows: statistical analysis[4]

5.1. Introduction

Microplastics (MPs) are typically defined as plastic particles < 5 mm in nominal diameter, and they are ubiquitous and persistent in aquatic environments (Galloway et al., 2017). Their detrimental effects on aquatic environments and widespread distribution have garnered substantial attention in recent years (Chubarenko et al., 2016; Galloway et al., 2017; Van Melkebeke et al., 2020). To better understand and predict the distribution of MPs and to effectively plan and execute cleanup efforts, it is essential to develop a comprehensive understanding of the mechanisms governing microplastic (MP) transport in water bodies. Despite being a crucial mode of transport, near-bed transport (i.e., bedload transport) of MPs has only received limited attention.

Previous studies on the near-bed transport of MPs have primarily focused on determining the threshold conditions under which MP mobilization occurs, emphasizing the combined influence of MP properties and bed roughness (Waldschläger & Schüttrumpf, 2019b; Yu et al., 2023; Yu, Yao, et al., 2022). Empirical formulas have been proposed to predict the critical shear stresses required to mobilize MPs with various shapes (spherical, cubic, cylindrical, etc.), densities (ρ_p, 1008-1400 kg/m^3), and sizes (D_n, 0.75-5.04 mm) on beds with different median bed grain sizes (D_{50}, 0.5-5.0 mm) (Waldschläger & Schüttrumpf, 2019b; Yu et al., 2023; Yu, Yao, et al., 2022). These previous studies provide valuable insights for exploring empirical methods to quantify the

[4] The content of this chapter has been submitted as a journal manuscript: Yu, Z., Loewen, M., Zhou, Y., Guo, Z., Baki, A., & Zhang, W. (2024). Continuous Near-bed Movements of Microplastics in Open Channel Flows: Statistical Analysis. *Environmental Science & Technology*, Under Review.

bedload transport rate of MPs (Lajeunesse et al., 2010; Yu et al., 2023; Yu, Yao, et al., 2022). However, it should be noted that previous research has only investigated the deterministic properties of MP movements. Considering near-bed flow turbulence, bed morphology irregularities, and the randomness of particle-bed interactions, it is essential to account for the stochastic nature of MP movements to achieve a comprehensive understanding of MP transport and gain insights into establishing a robust and rigorous framework for MP transport. Therefore, a detailed statistical description of MP movements is needed; however, no experimental investigations have yet been conducted on this topic.

This study focused on a simplified scenario in which millimeter-sized MPs (D_n = 0.28-0.42 cm) with a range of relative densities (ρ_p/ρ -1, where ρ is the density of the ambient fluid) between 0.2 and 0.4 were continuously transported over a uniform, fixed rough bed without resting or suspension. A total of nine different combinations of equivalent bed grain roughnesses (k_s) and mean flow velocity were considered. The ratio of k_s/D_n ranges from 0.12 to 0.88. Particle tracking velocimetry was employed to investigate the statistical behavior of MP movement. This study specifically examined the influence of MP properties (D_n, ρ_p, and particle shape), k_s, and mean flow velocity (U) on the ensemble mean and standard deviation of MP streamwise velocity. Additionally, the study explored the diffusive properties of MPs during continuous movement.

5.2. Literature review

Given the lack of research on the statistical behavior of MPs in continuous movements, extrapolating insights from previous sediment studies is a useful approach. The analogy between bedload MPs and sediments in their initiation of motion and settling behavior has been frequently discussed in recent studies, potentially due to the similar range of studied particle sizes (Yu et al.,

2023; Yu, Yao, et al., 2022). This similarity may also contribute to analogous bedload transport mechanisms (Waldschläger et al., 2022; Yu et al., 2023). The continuous transport of bedload sediments and their statistical ensemble behavior are commonly analyzed within a one-dimensional framework, focusing on the streamwise direction, as they predominantly travel downstream (Cheng & Emadzadeh, 2014; Fan et al., 2017; Martin et al., 2012).

For particles continuously moving on a smooth bed, their ensemble mean streamwise velocity ($\langle v_x \rangle$) can be estimated as the near-bed flow velocity at a representative height (on the order of particle size) above the bed (Cheng & Emadzadeh, 2014; Julien & Bounvilay, 2013). For rough bed cases, $\langle v_x \rangle$ is commonly estimated using the following form (Fan et al., 2014; Heyman et al., 2016; Martin et al., 2012):

$$\langle v_x \rangle = a\left(u_* - b\right) \tag{5-1}$$

where u_* is the bed shear velocity; and a and b (m/s) are empirical parameters that implicitly account for the viscous effects of the fluid on near-bed particle motions. In sediment studies, the parameter a can range from 3-35 depending on the near-bed flow conditions and bed features (Fan et al., 2014; Heyman et al., 2016; Martin et al., 2012). For fixed beds, the observed a values are generally larger compared to mobile beds. One of the reasons is that fixed beds are commonly constructed by gluing particles of a specific diameter to a rigid plane boundary, which reduces the influence of variations in bed geometry, such as ripples and dunes, compared to mobile beds. As a result, there is less friction and consequently less impediment to particle movements (Lajeunesse et al., 2010). The parameter b represents the intercept of the linear fit with the abscissa axis and is frequently compared with the critical shear velocity required to initiate particle mobilization u_{*c} (Lajeunesse et al., 2010; Martin et al., 2012). For fixed beds, b is found to be smaller than u_{*c}, and

b can be interpreted as the threshold shear velocity for disentrainment, i.e., the shear velocity at which particles initially in motion come to a halt (Martin et al., 2012).

To explicitly quantify the impacts of ρ_p, D_n, u_*, and k_s on $\langle v_x \rangle$, Julien and Bounvilay (2013) (Julien & Bounvilay, 2013) measured the mean velocities of sediments, glass marbles, and steel balls in continuous motion on smooth and rough beds, and performed a dimensional analysis. They suggested that $\langle v_x \rangle$ can be estimated with:

$$\frac{\langle v_x \rangle}{V_s} = 11.5\Theta_p^{0.95} D_*^{0.21} \left(\frac{k_s}{D_n}\right)^{-0.36} \left(\frac{\rho_p}{\rho} - 1\right)^{-0.28} \tag{5-2}$$

where V_s (= $[(\rho_p/\rho - 1)gD_n]^{0.5}$) is a characteristic velocity which represents a velocity scale that quantifies the combined effect of particle density and size. It is also commonly referred to as an approximation of the terminal settling velocity of sediments under turbulent conditions (Ancey, 2020); Θ_p is the particle Shields parameter, defined as u_*^2/V_s^2; D_* is the dimensionless particle diameter, defined as $D_n[(\rho_p/\rho - 1)g/\nu^2]^{1/3}$, where ν is the kinematic viscosity of the fluid; and k_s is assumed to be D_{50}. Eq. (5-2 is valid for $0.04 < k_s/D_n < 1.0$ and $2.5 < \rho_p/\rho < 8.0$. Alternatively, to account explicitly for the impacts of ρ_p, D_n, u_*, and k_s on $\langle v_x \rangle$, a one-dimensional force analysis can be applied. Using this approach and literature data, Cheng (2014) (Cheng & Emadzadeh, 2014) proposed an equation for $\langle v_x \rangle$:

$$\frac{\langle v_x \rangle}{V_s} = 13.0\sqrt{\Theta_p} - 1.5\left(\frac{k_s}{D_n}\right)^{0.6} \tag{5-3}$$

For rigid bed cases where $k_s < D_n$, Eq. (5-3) is valid for D_n = 2.4-29.3 mm, ρ_p = 2.6-8.0 g/cm^3, and k_s = 1.2-3.4 mm.

The stochastic nature of MP movements could result in time-dependent streamwise diffusion of MPs as they travel downstream. To investigate the diffusive properties of MPs, insights can be drawn from sediment studies regarding bedload diffusion (Martin et al., 2012; Nikora et al., 2002). The classic Einstein–Smoluchowski equation, originally proposed to describe the motion of Brownian particles in one dimension, has been commonly adapted to characterize streamwise bedload diffusion (Fathel et al., 2016). Specifically, this diffusion process was quantified by the growth of the streamwise mean squared displacements of bedload particles [$\sigma(\tau)^2$] over a given time interval defined as:

$$\sigma(\tau)^2 = \left\langle [d_x(\tau) - \langle d_x(\tau) \rangle]^2 \right\rangle \tag{5-4}$$

where $d_x(\tau)$ [$= x(t + \tau) - x(t)$] is the streamwise displacement of a single particle over the time interval τ; $x(t)$ is the position of a particle at time t; the angle bracket represents the ensemble average over all particles (Fathel et al., 2016). For experimental observations, τ can range from the time interval between consecutive image frames (Δt) of the recorded video to the minimum time required for one particle to travel the entire length of the field of view (Martin et al., 2012). Identifying a diffusion regime relies on the value of the scaling diffusion exponent (γ) in the relationship $\sigma(\tau)^2 \propto \tau^{\gamma}$ (Fathel et al., 2016). Depending on the value of γ, the diffusion regime of particle streamwise movements can be classified as normal ($\gamma = 1.0$) or anomalous ($\gamma \neq 1.0$). In normal diffusion, the variance of particle displacement increases linearly with time, meaning that as time passes, particles spread out from their original position at a steady, constant rate. Anomalous diffusion can be further categorized into sub-diffusive ($\gamma < 1.0$), super-diffusive ($\gamma > 1.0$), and ballistic ($\gamma = 2.0$) (Martin et al., 2012; Nikora et al., 2002). In sub-diffusion, particles

spread more slowly compared to normal diffusion, and $\sigma(\tau)^2$ grows slower than linearly with time. In super-diffusion, particles spread faster, with $\sigma(\tau)^2$ growing faster than linearly.

In a typical bedload diffusion process, different diffusion regimes can emerge and change with the time scale (Nikora et al., 2002). Nikora et al. (2002) (Nikora et al., 2002) suggested that bedload diffusion is comprised of three ranges of scales: local, intermediate, and global. Specifically, the local range involves sediment trajectories between two consecutive collisions with the bed at short time scales, typically characterized by ballistic diffusion. This regime may arise from correlated particle motions driven by particle inertia. The global range covers sediment trajectories that include periods of particle resting at long time scales, typically associated with sub-diffusive sediment movements which indicates that sediments diffuse at a rate slower than linear over time. The intermediate range lies between local and global ranges, involving multiple sediment-bed collisions at medium time scales. The diffusion behavior in this range can vary, exhibiting either normal or anomalous characteristics.

5.3. Methodology

5.3.1. MP properties

MPs made of Polymethyl methacrylate (PMMA), Polyvinyl chloride (PVC), and Polyethylene terephthalate (PET) were selected for testing based on previous research on benthic sampling of MPs in aquatic environments (Kabir et al., 2022; Yang et al., 2021). The MPs were uniform in size with a range of D_n = 0.32-0.42 cm (Table 5-1). The densities of PMMA, PVC, and PET range from 1.20 to 1.40 g/cm^3, determined using the titration method. The values of D_* and V_s of PMMA, PVC, and PET range from 40 to 56 and 7.85 to 10.53 cm/s, respectively. The shape of MPs was quantified using Corey's shape factor (*csf*), defined as $l_c/(l_a l_b)^{1/2}$, where l_a, l_b, and l_c represent the

lengths of the longest, intermediate, and shortest sides of a particle, respectively (Yu, Yao, et al., 2022). The values of *csf* for PMMA, PVC, and PET ranged from 0.58 to 0.89 (Table 5-1).

Table 5-1 Summary of the MP properties. The density and nominal diameter of microplastics are denoted by ρ_p and D_n, respectively. D_* represents the dimensionless particle diameter. V_s indicates the characteristic velocity. *csf* represents Corey's shape factor.

Type	ρ_p (g/cm^3)	D_n (cm)	D_*	V_s (cm/s)	*csf*
PMMA	1.20 ± 0.01	0.32 ± 0.02	39.83	7.85	0.76
PVC	1.24 ± 0.01	0.42 ± 0.03	56.46	10.00	0.89
PVC	1.24 ± 0.01	0.34 ± 0.03	45.11	8.94	0.58
PET	1.40 ± 0.01	0.28 ± 0.02	44.57	10.53	0.72

5.3.2. Experimental setup and instrumentation

The experiments used the same recirculating flume as in our previous studies (Yu et al., 2023; Yu, Yao, et al., 2022), which was 7.50 m long, 0.75 m wide, and 0.50 m deep with a 0.2% slope (Figure 5-1). Flow was generated by a pump with a variable frequency drive, capable of a maximum flow rate of 150 L/s with a resolution of 1.31 L/s. Flow rates were measured using a magnetic flow meter (*Foxboro IMT25-SEATB10K-BG*). At the upstream end of the flume, a flow straightener was installed to reduce lateral velocities and make the velocity distribution more uniform.

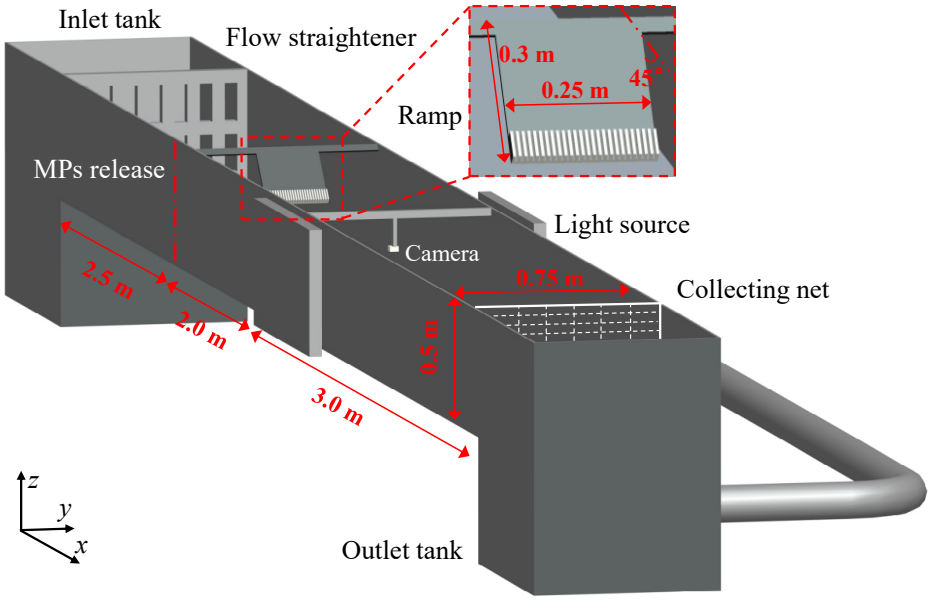

Figure 5-1 Sketch of the experimental setup.

The observational area for MP particle tracking was 2.0 m long and 0.75 m wide, located 4.5 m downstream of the flume inlet. The flow depth was kept constant at H = 31.0 ± 0.3 cm using an adjustable tailgate. Three mean flow velocities (35, 40, and 50 cm/s) were selected, resulting in the Reynolds number Re (= UH/ν) ranging from 1.05×10^5 to 1.51×10^5 and the Froude number Fr [= $U/(gH)^{0.5}$] ranging from 0.20 to 0.28, indicating fully turbulent and subcritical flow conditions. Fixed rough beds with three equivalent bed grain roughness conditions were used: k_s = 0.5, 1.0, and 2.5 mm. Experiments were conducted for each type of MP using nine different flow conditions labeled R1-R9, corresponding to different combinations of U and k_s, as outlined in Table 5-2. The shear velocities u_* for each flow condition were estimated using the turbulent kinetic energy method, as described in detail in our previous study (Yu et al., 2023). The values of u_* for all nine flow conditions exceeded the reported critical flow conditions necessary to initiate the movements of MPs with similar physical properties on beds with comparable roughnesses (Yu et al., 2023). For the nine flow conditions, the roughness Reynolds number k_s^+ (= u_*k_s/ν) ranged from 8 to 63,

which is below the fully rough limit of 70 (Dey, 2014); therefore the beds can be characterized as transitionally rough. Preliminary tests were conducted to confirm the occurrence of continuous near-bed movements of MPs for different experimental cases.

Table 5-2 Summary of experimental (bed and flow) conditions for each type of MPs. The bed roughness is denoted by k_s. U represents the ambient flow velocity. Re indicates Reynolds number. Fr indicates Frode number. u_* represents the shear velocity.

Flow condition	k_s **(mm)**	U **(cm/s)**	***Re***	***Fr***	***u**** **(cm/s)**
R1	0.5	35	1.05×10^5	0.20	1.67
R2	0.5	40	1.21×10^5	0.23	1.91
R3	0.5	50	1.51×10^5	0.28	2.22
R4	1.0	35	1.05×10^5	0.20	1.78
R5	1.0	40	1.21×10^5	0.23	2.05
R6	1.0	50	1.51×10^5	0.28	2.38
R7	2.5	35	1.05×10^5	0.20	1.97
R8	2.5	40	1.21×10^5	0.23	2.18
R9	2.5	50	1.51×10^5	0.28	2.52

To propel MPs into the flow, a 0.3 m long and 0.25 m wide plexiglass ramp (Figure 5-1) was installed at the top of the flume. The ramp was partitioned into 25 evenly spaced slots and was angled at 45 degrees from the free surface. The lower end of the ramp extended approximately 5 cm below the water surface and was positioned 2.0 m upstream from the observational area. A plexiglass barrier plate was used to temporarily block the lower end of the ramp to hold MPs stationary on the ramp prior to their release. Preliminary tests showed that the release location was sufficiently upstream to ensure continuous near-bed movement of MPs before they passed through the observational area.

A GoPro camera (*Hero 8*) with an image resolution of 2704 pixels ×1520 pixels and a frame rate of 60 Hz was used to record the movements of MPs in the observational area. The camera was mounted looking vertically downward at the center of the observational area with the lens submerged approximately 1 cm below the water surface to eliminate reflections and refraction from water-surface undulations. To provide contrast between the MPs and the black bed surface, two quartz halogen lights (*QL-1000*) were placed on both sides of the flume to provide illumination.

Camera calibration was carried out to correct lens distortions and other misalignments during the imaging process before conducting experiments. The calibration process followed the steps provided in the open-source program *Gyroflow* (https://gyroflow.xyz/). It required capturing 60 seconds of video of a 32.0 cm × 21.0 cm calibration chessboard positioned underwater at various locations within the field of view. Specifically, this involved aligning the edge of the image frame with the chessboard edge and matching the corners of the chessboard with the image frame corners, respectively. The captured frames were then imported into *Gyroflow* to generate a calibration profile for correcting images during pre-processing. The calibration accuracy was acceptable with a mean reprojection error of ~0.5 pixels (Shortis, 2015). The calibration tests confirmed that the camera placement effectively captured a sequence of clear images of MP motion with a field of view of approximately 40.0 cm × 23.0 cm.

5.3.3. Experimental procedures

A total of 360 experimental tests were performed, which included 36 (4 × 9) experimental cases of different MPs and flow conditions, with at least 10 repeats for each case. A consistent experimental procedure was followed in each case. First, MPs of a specific type were immersed in water for a duration of 3 hours to reduce surface tension and eliminate air bubbles from the particle

surfaces. The designated flow velocity was then set by adjusting the variable frequency drive of the pump. MPs were then placed in each of the 25 channels on the plexiglass plate, and upon removal of the barrier plate, the particles were released simultaneously into the flow. MP movements on the bed within the observational area were then recorded for a duration of ~3 seconds until all particles moved out of the field of view. The release of MPs and the recording of their movements were repeated at least 10 times, yielding over 1800 frames of MP movements. This resulted in a dataset comparable in size to previous sediment tracking experiments (over 1300 frames per case) (Shim & Duan, 2019; Shim & Duan, 2017). Moreover, the range of the maximum value of the surface concentration of moving MPs (= cD_n^2, where c is the number of moving MPs per unit bed area) varied from 0.002 to 0.004. The low surface concentration ($<< 1$) indicates that interactions between MPs in motion were negligible (Seizilles et al., 2014).

5.3.4. Image processing

Figure 5-2 shows the key steps of the image processing procedures, applied to analyze the MP movements for each case. First, the raw video from each test was processed using the calibration profile created in *Gyroflow*. Next, *Adobe Premiere Pro 2022* was used to extract a series of consecutive images from the processed video. ImageJ was then used to convert the images to grayscale and subtract the average background intensities. The plugin in *ImageJ*, *Trackmate*, was employed to identify MPs in each frame of the image sequence using the Laplacian of Gaussian algorithms (Tinevez et al., 2017). The detected MPs in each frame were then matched and linked together into tracks using the Linear Assignment Problem tracker algorithms included in *Trackmate* (Tinevez et al., 2017). Using the outputs of time-evolved streamwise and cross-stream displacements with a time step of $\Delta t = 0.0167$s, the corresponding instantaneous streamwise and cross-stream particle velocities (v_x, v_y) were computed:

$$\begin{cases} v_x = [x(t+\Delta t) - x(t)]/\Delta t \\ v_y = [y(t+\Delta t) - y(t)]/\Delta t \end{cases} \tag{5-5}$$

where $y(t)$ is the cross-stream spatial coordinate at time t. For each case, the ensemble means of streamwise particle velocity ($\langle v_x \rangle$) and standard deviations [$\langle \delta(v_x) \rangle$] were calculated by considering all instantaneous velocity data from repeated tests. The direction of MP motion was described by the instantaneous orientation angle, θ, defined as $\tan^{-1}(v_y/v_x)$.

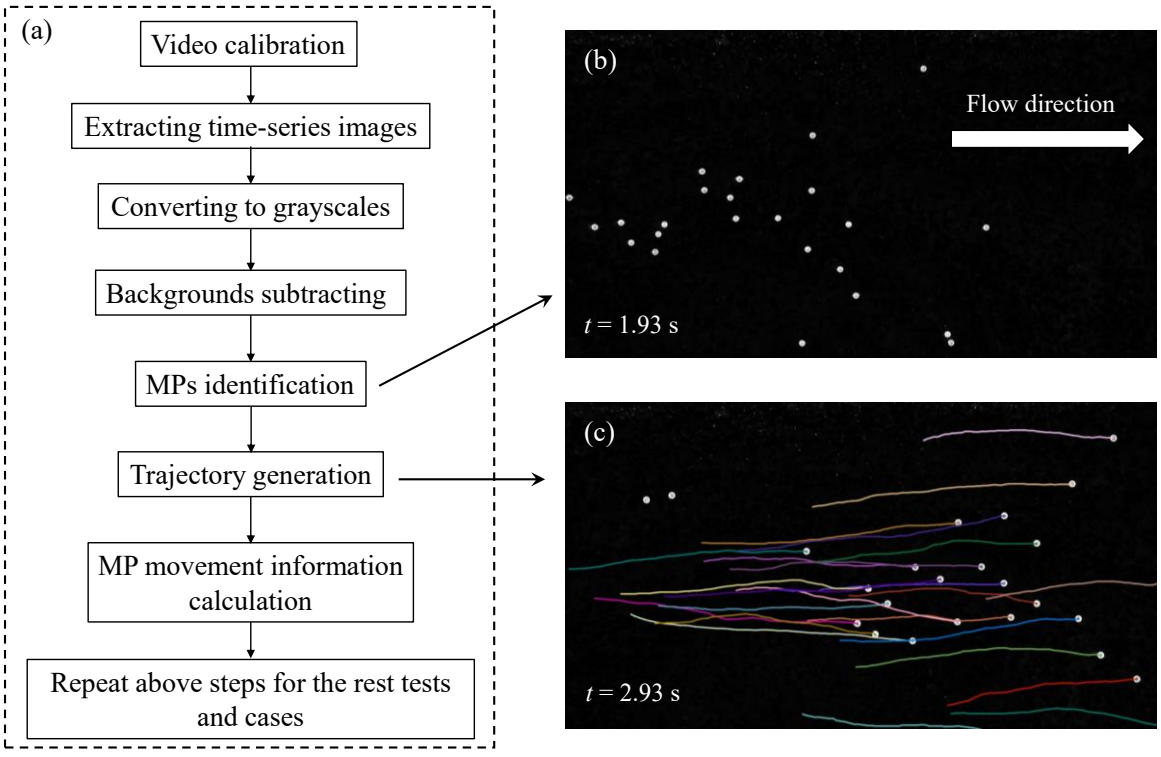

Figure 5-2 (a) Flowchart of the image processing procedure applied to each case. (b) A processed image from a sample test of PET in R1 after the "MPs identification" step. (c) A processed image from the same sample test after the "trajectory generation" step. The white dots indicate the identified MPs and the colored lines represent their respective trajectories over a time interval of 1 s.

5.3.5. Error and uncertainty analysis

The primary source of error in applying particle tracking velocimetry to measure near-bed particle motions is uncertainty in locating the particle centroid during tracking (Ashley et al., 2020; Campagnol et al., 2015). The position of the particle centroid was tracked to within one pixel using *Trackmate*. Combining the reprojection error during calibration, the uncertainty in position determination can be assumed reasonably as ~1.1 pixels (Campagnol et al., 2015). This results in an estimated uncertainty of 0.98 cm/s in instantaneous particle velocity. Using error propagation, the range of magnitude of uncertainty in the ensemble mean velocity of a single particle can be calculated, which varied from 0.06 cm/s for the largest sample values of 263 (PET in R7) to 0.11 cm/s for the smallest sample values of 81 (PMMA in R3). The centroid localization error was therefore neglected in further analysis because it is small in magnitude and unlikely to bias the mean particle velocity measurements. Other sources of error commonly detected in a particle tracking velocimetry system can be low signal-to-noise ratio and overlapping particles (Ahmadi et al., 2019), which were negligible in the current experimental setup. The signal-to-noise ratio was enhanced by applying uniform light sources and subtracting the average background intensities. The error associated with overlapping particles was negligible due to the low surface concentration of MPs in each case.

5.4. Results and discussion

5.4.1. Probability distribution and ensemble mean of MP velocities

Figure 5-3a shows the probability distributions of θ for all 36 cases (represented by open squares). These distributions are approximately symmetric around $\theta = 0°$. The ensemble mean of θ varies from -0.26° to 0.26°, with a standard deviation ranging from 6.25° to 12.68° across all cases. For

clarity, the raw θ data for each MP type were combined into a single dataset, and the distribution of θ for each MP type across all conditions R1-R9 is shown separately. The ensemble mean of θ for different MP types ranges from -0.0044° to 0.017°, with a standard deviation ranging from 8.79° to 10.27°, indicating predominantly streamwise MP movements. Thus, the continuous movements of different MP types were assumed to be approximately one-dimensional in the streamwise direction.

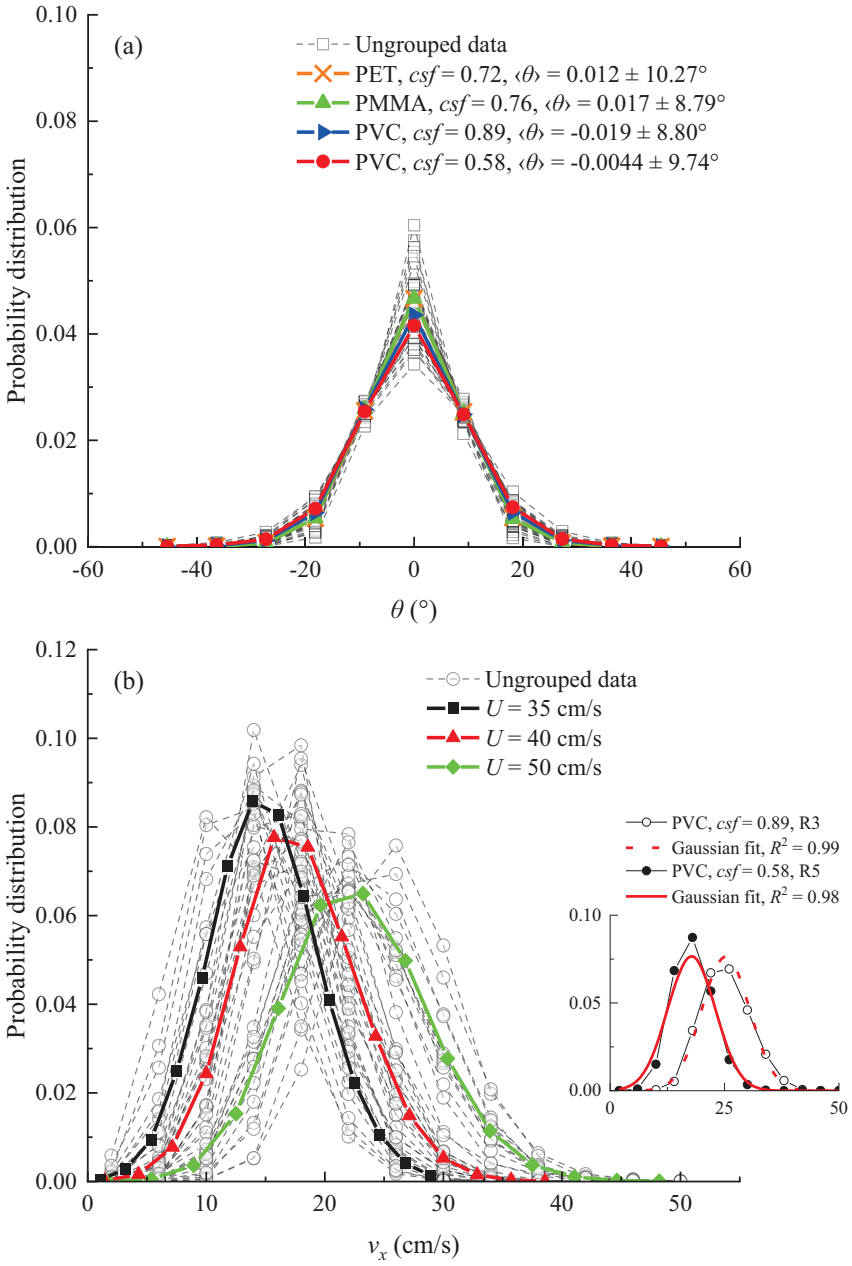

Figure 5-3 (a) Probability density distributions of the orientation angle, θ, for different types of MPs, shown with various colors: PET (orange), PMMA (green), PVC with $csf = 0.89$ (blue), and PVC with $csf = 0.58$ (red). Open squares represent ungrouped data of θ for all 36 cases. (b) Probability density distributions of the instantaneous streamwise MP velocity, v_x, for different flow velocities, indicated with different colors: $U = 35$ cm/s (black), 40 cm/s (red), and 50 cm/s (green). Open circles represent ungrouped data of v_x for all 36 cases. The inset shows Gaussian fits for PVC with $csf = 0.89$ in R3 and PVC with $csf = 0.58$ in R5.

Figure 5-3b shows the probability distributions of v_x for all 36 cases (represented by open circles). These distributions exhibit significant dispersion across different cases, characterized by variations in their modes and widths. These variations were quantified by computing $\langle v_x \rangle$ and $\langle \delta(v_x) \rangle$ for the 36 cases and these values are listed in Table 5-3. Furthermore, the experimental distributions of v_x appear to be normally distributed in all cases. The equation for a normal distribution of v_x is given by:

$$f(v_x) = \frac{1}{\langle \delta(v_x) \rangle \sqrt{2\pi}} e^{-\frac{1}{2}\left[\frac{v_x - \langle v_x \rangle}{\langle \delta(v_x) \rangle}\right]^2} \tag{5-6}$$

Fitting Eq. 6 to the experimental data resulted in R^2 values ranging from 0.97 to 0.99. For clarity, the inset of Figure 5-3b presents two examples of Gaussian fits: one for PVC with csf = 0.89 in R3 (R^2 = 0.99, represented by open circles) and another for PVC with csf = 0.58 in R5 (R^2 = 0.98, represented by solid circles).

The impact of the ambient flow velocity U on shaping the distributions of v_x is evident. The distributions in Figure 3b exhibit thin tails, which is expected given that the highest v_x is unlikely to exceed the flow velocity (Roseberry et al., 2012). The normal distributions of v_x align with previous observations of the continuous movements of sediments (Martin et al., 2012; Shim & Duan, 2019). This may be primarily attributed to the same fully turbulent flow conditions reported in the sediment studies in which the range of Re was 4800 to 1.8×10^4 (Martin et al., 2012)·(Shim & Duan, 2019). Three v_x distribution profiles obtained by combining all of the data at the same U into a single dataset (colored dots) are also compared in Figure 3b. As U increases, both $\langle v_x \rangle$ and $\langle \delta(v_x) \rangle$ increase, with the mode shifting and the width of the distribution broadening. Specifically, $\langle v_x \rangle$ increases from 14.94 to 22.66 cm/s, and $\langle \delta(v_x) \rangle$ increases from 4.59 to 5.90 cm/s.

The shear velocity u_* can be used to quantify variations in k_s and U. Figure 4a presents the relationship between $\langle v_x \rangle$ and u_* for all experimental cases, revealing a general increasing trend. This trend becomes more pronounced when considering data with the same k_s. Grouping the data points based on k_s values results in three distinct datasets: R1-R3 with k_s = 0.5 mm (red data points in Figure 4a), R4-R6 with k_s = 1.0 mm (green), and R7-R9 with k_s = 2.5 mm (purple). Each of these datasets is well represented by a linear fit, with corresponding R^2 values of 0.94, 0.90, and 0.87, respectively. The positive slope of the linear fit for each dataset indicates that MPs move more slowly at lower flow velocities (U). Additionally, the similar slopes but differing intercepts of the linear fits indicate that MPs tend to move more slowly on rougher beds for a given U. Recall that in the linear fits of $\langle v_x \rangle$ versus u_*, the intercept on the x-axis represents the disentrainment threshold for MPs. Figure 4a shows that the intercept of the linear fit for each grouped dataset increases as k_s increases, indicating that MPs tend to have a higher disentrainment threshold on a rougher bed. Furthermore, note that within each grouped dataset with the same k_s, there is a noticeable scatter for individual cases. This scatter is likely due to the varying physical properties of MPs, as the disentrainment threshold varies for MPs with different physical properties moving across rough beds with different k_s. These 12 disentrainment thresholds (four types of MPs moving on rough beds with three different k_s), i.e., the parameter b in Eq. (5-1), were obtained via linear regression and compared in Figure 4b with the corresponding u_{*c} values determined in our previous study (Yu et al., 2023).

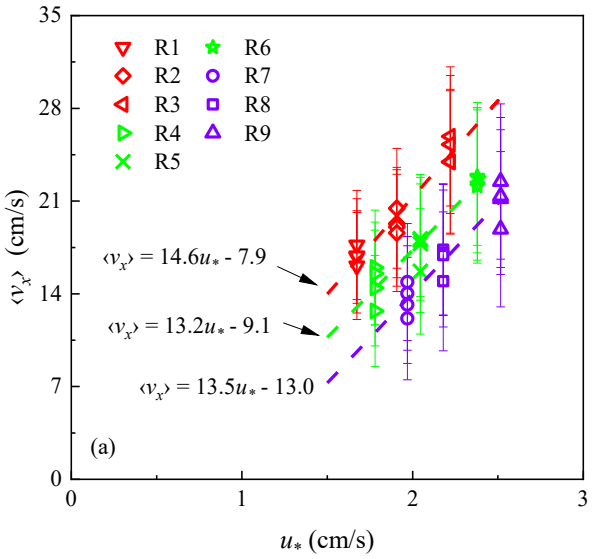
R1
R2
R3
R4
R5
R6
R7
R8
R9
⟨v_x⟩ = 14.6u_* - 7.9
⟨v_x⟩ = 13.2u_* - 9.1
⟨v_x⟩ = 13.5u_* - 13.0
(a)
⟨v_x⟩ (cm/s)
u_* (cm/s)

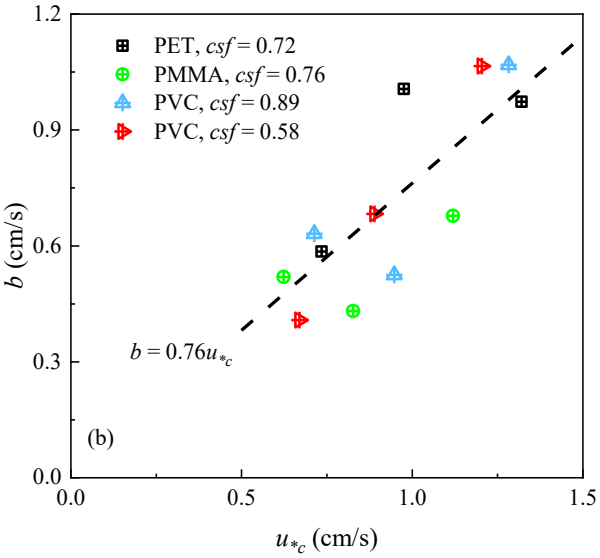
PET, csf = 0.72
PMMA, csf = 0.76
PVC, csf = 0.89
PVC, csf = 0.58
$b = 0.76u_{*c}$
(b)
b (cm/s)
u_{*c} (cm/s)

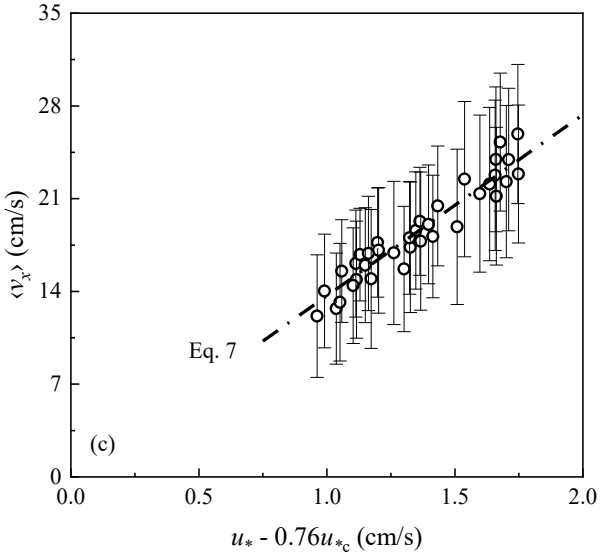
Eq. 7
(c)
⟨v_x⟩ (cm/s)
u_* - 0.76u_{*c} (cm/s)

Figure 5-4 (a) The mean streamwise MP velocity, $\langle v_x \rangle$, versus the corresponding shear velocity, u_*, for all experimental cases. The error bars denote the standard deviation, $\langle \delta(v_x) \rangle$. The three colored dashed lines represent the best linear fits for the relationships between $\langle v_x \rangle$ and u_*, each line corresponding to a specific bed roughness condition: R1-R3 (red), R4-R6 (green), and R7-R9 (violet). (b) The parameter b in Eq. 1 versus the critical shear velocity of different types of MPs, u_{*c}, across various k_s. The black dashed line indicates the best linear fit. (c) $\langle v_x \rangle$ versus the corresponding values of $u_* - 0.76u_{*c}$. The dash-dotted line represents Eq. 7.

Figure 5-4b shows the value of b is smaller than u_{*c} on average, as indicated by the linear fit ($b = 0.76u_{*c}$) with a relative error of 17.8%. This result aligns with the previous results of the sediment movements (Fernandez Luque & Van Beek, 1976; Hu & Hui, 1996; Martin et al., 2012). The linear correlation equation between b and u_{*c} was used to estimate the value of the parameter a by fitting Eq. (5-1) with the observed $\langle v_x \rangle$ of all cases (Figure 4c). Eq. (5-1) is then revised for MPs as follows:

$$\langle v_x \rangle = 13.67\left(u_* - 0.76u_{*_c}\right) \tag{5-7}$$

Eq. (5-7) has a small relative error of 5.2%. The fitted parameter $a = 13.67$ is comparable to those reported in the fixed bed experiments of sediments. Specifically, a = 13.5-14.3 in Abbott and Francis (1977) and $a = 13.6$ in Martin et al. (2012). Eq. (5-7) is valid for $D_* = 40$-56, $csf = 0.7$-0.9, and $k_s = 0.5$-2.5 mm.

Table 5-3 Summary of the ensemble mean streamwise MP velocity ($\langle v_x \rangle$), the standard deviation of v_x [$\langle \delta(v_x) \rangle$], and the scaling diffusion exponent (γ) for nine different cases involving different types of MPs.

Case	Type	*csf*	$\langle v_x \rangle$ (cm/s)	$\langle \delta(v_x) \rangle$ (cm/s)	γ
R1	PMMA	0.76	17.69	4.12	1.72
R1	PVC	0.89	16.78	3.50	1.73
R1	PVC	0.58	16.87	4.31	1.73
R1	PET	0.72	16.11	4.04	1.71
R2	PMMA	0.76	20.45	4.52	1.73

R2	PVC	0.89	19.29	4.07	1.73
R2	PVC	0.58	19.06	4.49	1.74
R2	PET	0.72	18.60	4.43	1.69
R3	PMMA	0.76	25.88	5.25	1.77
R3	PVC	0.89	25.27	5.21	1.75
R3	PVC	0.58	23.95	5.38	1.72
R3	PET	0.72	23.97	5.47	1.69
R4	PMMA	0.76	15.98	4.33	1.70
R4	PVC	0.89	15.54	3.88	1.68
R4	PVC	0.58	14.44	4.36	1.72
R4	PET	0.72	12.70	4.19	1.67
R5	PMMA	0.76	18.15	4.63	1.67
R5	PVC	0.89	18.04	4.26	1.75
R5	PVC	0.58	17.79	5.21	1.69
R5	PET	0.72	15.69	4.73	1.76
R6	PMMA	0.76	22.86	5.21	1.63
R6	PVC	0.89	22.77	5.67	1.75
R6	PVC	0.58	22.28	5.75	1.60
R6	PET	0.72	22.10	5.78	1.69
R7	PMMA	0.76	14.89	4.42	1.62
R7	PVC	0.89	14.03	4.29	1.67
R7	PVC	0.58	13.18	4.44	1.61
R7	PET	0.72	12.13	4.63	1.61
R8	PMMA	0.76	17.33	4.92	1.73
R8	PVC	0.89	17.10	4.73	1.74
R8	PVC	0.58	16.91	5.41	1.72
R8	PET	0.72	14.94	5.25	1.66
R9	PMMA	0.76	21.19	5.20	1.66
R9	PVC	0.89	22.47	5.86	1.68
R9	PVC	0.58	21.38	5.93	1.61
R9	PET	0.72	18.87	5.86	1.58

Additionally, as shown in Eqs. (5-2) and (5-3), $\langle v_x \rangle$ can be normalized using the characteristic velocity V_s and be estimated explicitly as a function of the relative roughness height k_s/D_n and Θ_p. In Figure 5 $\langle v_x \rangle/V_s$ is plotted versus Θ_p for all 36 cases in this study, alongside data from the literature, including non-MPs moving on fixed rough beds with different k_s/D_n values (Abbott & Francis, 1977; Cheng & Emadzadeh, 2014; Julien & Bounvilay, 2013; Lee & Hsu, 1994; Martin et al., 2012) or mobile beds (Lajeunesse et al., 2010; Niño & García, 1998; Shim & Duan, 2019). In general, the values of $\langle v_x \rangle/V_s$ for MPs increase with Θ_p, which is consistent with the increasing trend observed for non-MPs moving on fixed beds with $k_s/D_n < 1$ in the study of Julien and Bounvilay (2013). Moreover, MPs have a higher $\langle v_x \rangle$ on average compared to non-MPs in that study (Julien & Bounvilay, 2013). Given that the D_* values for non-MPs (62-778) are larger than those for MPs (39.83-56.46) in this study, the higher average $\langle v_x \rangle$ for MPs can be attributed to the fact that lighter particles (indicated by a smaller D_* value) tend to move faster on fixed beds with $k_s/D_n < 1$. Furthermore, for fixed bed scenarios, $\langle v_x \rangle$ values for particles in cases with $k_s/D_n < 1$ are higher on average than for those in cases with $k_s/D_n = 1$, indicating that increased relative bed roughness hinders particle movement, as previously discussed for MPs in Figure 5-4. It is also evident that $\langle v_x \rangle$ for mobile bed cases is smaller than that for fixed beds, as previously noted.

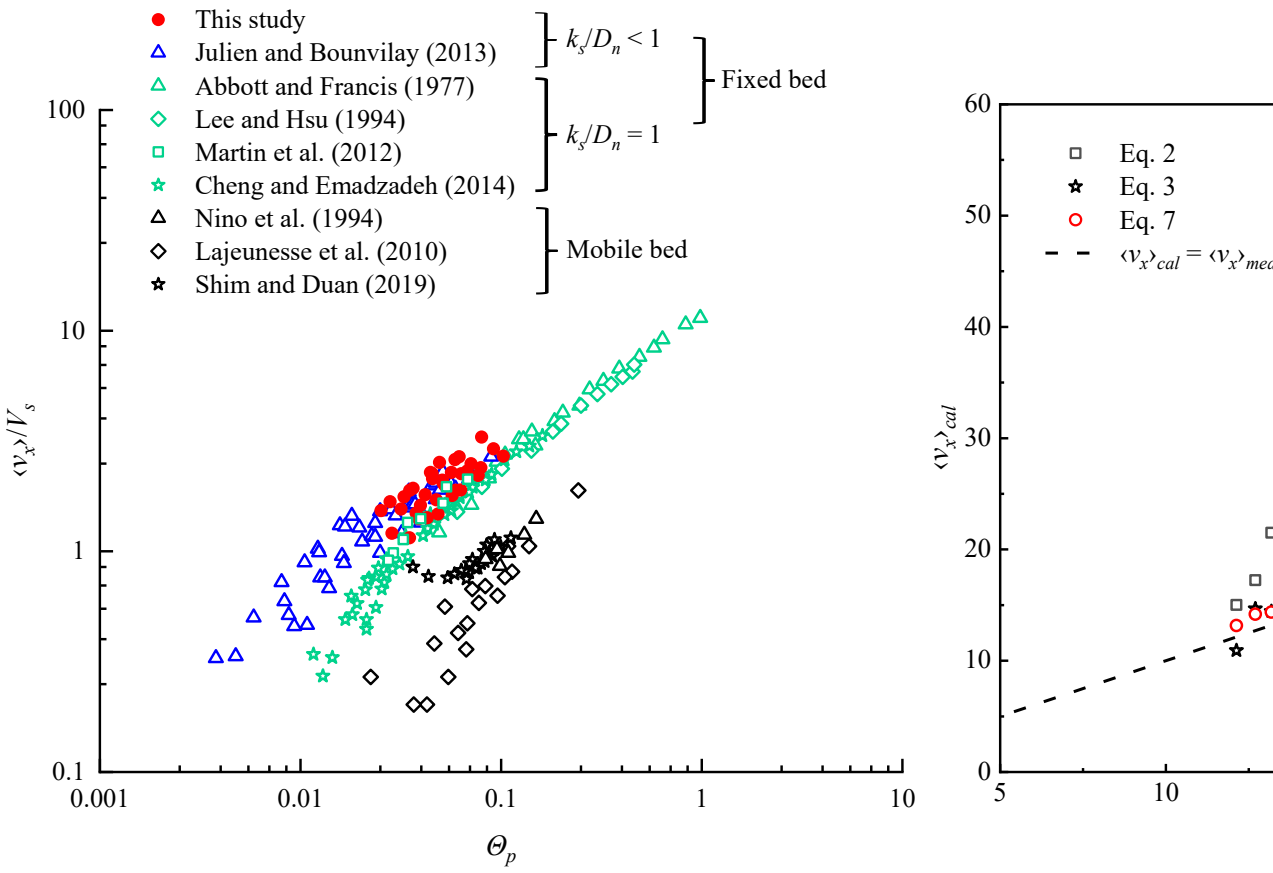

Figure 5-5 Comparison of the normalized $\langle v_x \rangle$ against the particle Shields parameter Θ_p for MPs moving on fixed rough beds with the relative roughness height $k_s/D_n < 1$ and non-MPs moving on fixed rough beds or mobile beds. Note that only part of the sediment data points in Julien and Bounvilay (2013) were plotted since detailed information was unavailable for the calculations of Θ_p for their full dataset.

Figure 5-6 compares the predicted values of $\langle v_x \rangle$ using Eqs. (5-2), (5-3), and (5-7) with the measured values. Eq. (5-2) overestimates $\langle v_x \rangle$, with a high relative error of 67.5%. This is likely because Eq. (5-2) was derived using a dataset with a wide range of k_s/D_n (0.04-1), where approximately 40% of the k_s/D_n values were lower than the smallest k_s/D_n value of 0.12 reported in this study ($k_s/D_n \approx 0.12$-0.88). Eqs. (5-3) and (5-7) had much smaller relative errors of 6.5% and 5.2%, respectively. Eq. (5-7) is recommended due to its relatively low error and its potential to accurately predict $\langle v_x \rangle$ for MPs with a wider range of physical properties, particularly as prediction

methods for MP mobilization thresholds continue to develop. Specifically, when predicting ‹v_x› for MPs with low *csf* values, such as fibers or films in continuous motion, Eq. (5-3) derived from a one-dimensional force analysis of a spherical particle may not be suitable. In contrast, Eq. (5-7) offers a clearer physical interpretation by describing the mean MP velocity as the difference between the flow velocity and the disentrainment threshold, where the influence of shape can be more easily considered.

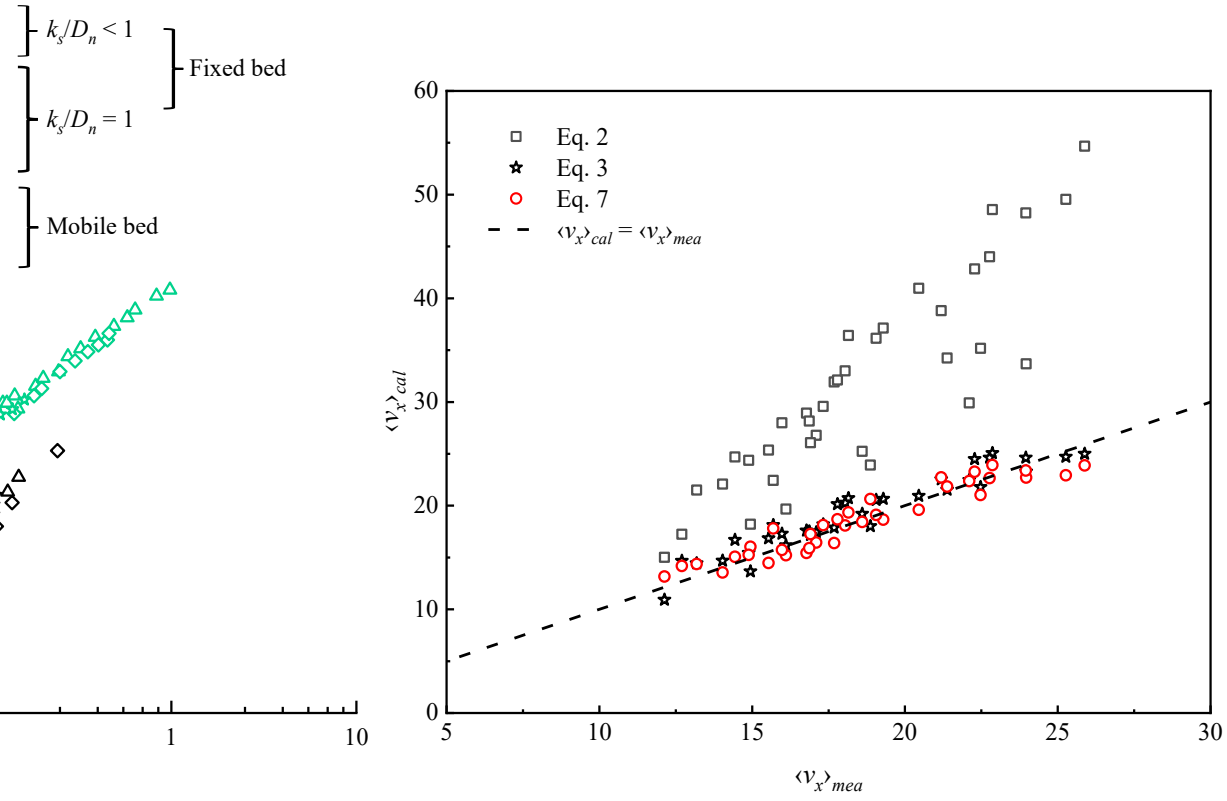

Figure 5-6 Comparison of the measured ‹v_x› values of MPs of cases R1-R9 (‹v_x›$_{mea}$) against the calculated ‹v_x› values (‹v_x›$_{cal}$) using the previous formulas for non-MPs (Eqs. 5-2 and 5-3) and the proposed formula for MPs (Eq. 5-7). The dashed line represents ‹v_x›$_{mea}$ = ‹v_x›$_{cal}$.

5.4.2. Standard deviations of MP velocities

The variability in the width of v_x distributions for different cases is investigated by assessing the impact of experimental conditions and MP properties on ‹$\delta(v_x)$›. It is logical to expect that ‹$\delta(v_x)$›

can also be normalized by V_s and related to Θ_p, similar to $\langle v_x \rangle$. In Figure 5-7, Θ_p is plotted versus $\langle \delta(v_x) \rangle / V_s$ and a semi-logarithmic relationship is evident between these two dimensionless variables. A linear regression produced the following equation with a R^2 value of 0.92:

$$\frac{\delta\langle v_x \rangle}{V_s} = 0.25 \ln(\Theta_p) + 1.28 \tag{5-8}$$

The relative error for Eq. (5-8) is 4.3%. Eq. (5-8) indicates that the width of the v_x distribution increases with the increase of Θ_p. For the same type of MPs, $\langle \delta(v_x) \rangle$ increases with the increase of u_*, since $\Theta_p = u_*^2/V_s^2$. This is because an increase in u_* likely intensifies the frequency and vigor of collisions between MP particles and the underlying bed, thus leading to higher fluctuations in v_x (Lajeunesse et al., 2010; Ninto & Garcia, 1996). Moreover, Eq. (5-8) is applicable to MPs within the studied ranges of physical properties (D_n = 0.32-0.42 cm; ρ_p = 1.20-1.40 g/cm^3; and *csf* = 0.58-0.89) under the experimental conditions considered (U = 35-50 cm/s and k_s = 0.5-2.5 mm). Eq. (5-8) can serve as an additional validation for future numerical model development or be combined with Eq. (5-7) to provide initial estimates for MP transport models that assume a normal distribution for v_x.

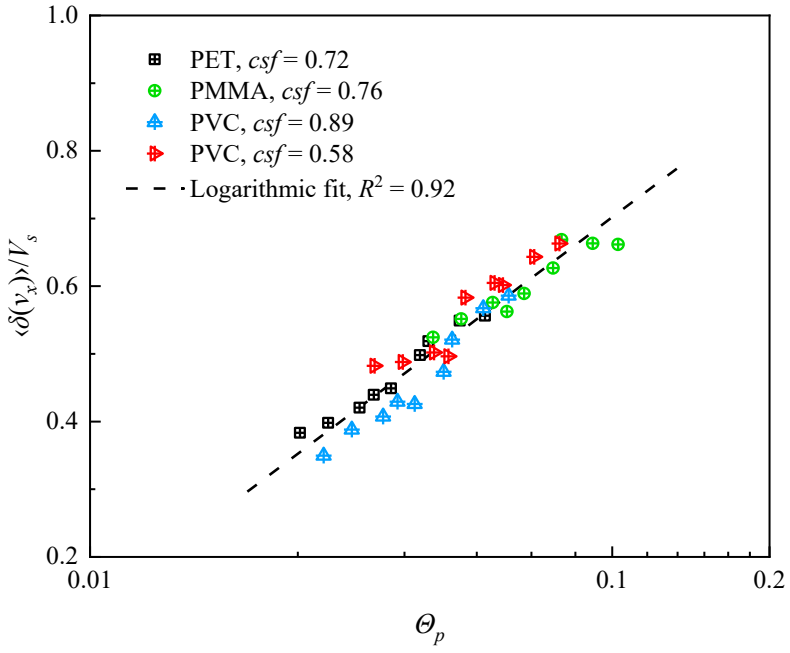

Figure 5-7 The normalized standard deviation, $\langle\delta(v_x)\rangle/V_s$, for different types of MPs as a function of the particle Shields parameter, Θ_p. The dashed line indicates the best logarithmic fit.

5.4.3. MP diffusion

Following a previous study on bedload sediment diffusion (Nikora et al., 2002), the normalized growth of the variance of displacements $[\sigma(\tau)^2/D_n^2]$, and the normalized time interval ($\tau u_*/D_n$) were introduced. Figure 5-8a-c show the power law relationship between these normalized parameters for all cases. For clarity, the data points corresponding to different bed roughnesses were organized into three subplots. For each experimental case, the value of γ was obtained via fitting Eq. (5-4) and was provided in Table 5-3. The values of γ vary from 1.58 to 1.77 for the different MP types, falling within the range of 1.0-2.0 (also shown in Figure 5-8a-c). These results show that the diffusion processes of MPs conducting continuous movements were super-diffusive over a range of $\tau u_*/D_n \approx$ 0.06-10.0. The reported γ values of 1.58-1.77 are comparable to those for continuous

sediment movements, 1.40-1.74 (Martin et al., 2012; Nikora et al., 2002), indicating that MPs and sediments share similarities in their diffusion processes.

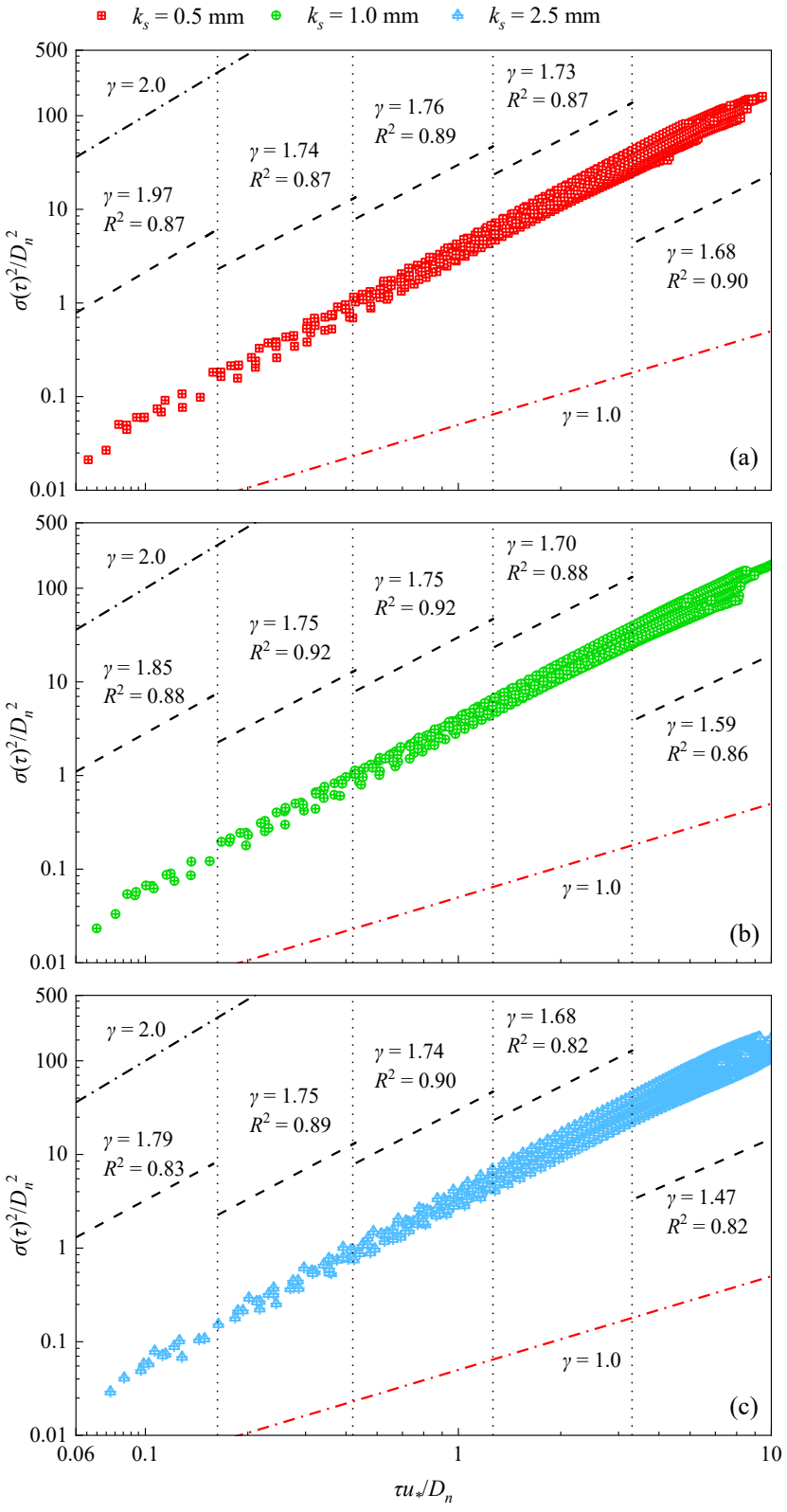
k_s = 0.5 mm
k_s = 1.0 mm
k_s = 2.5 mm
$\sigma(\tau)^2/D_n^2$
$\tau u_*/D_n$
γ = 2.0
γ = 1.97
R² = 0.87
γ = 1.74
R² = 0.87
γ = 1.76
R² = 0.89
γ = 1.73
R² = 0.87
γ = 1.68
R² = 0.90
γ = 1.0
(a)
γ = 2.0
γ = 1.85
R² = 0.88
γ = 1.75
R² = 0.92
γ = 1.75
R² = 0.92
γ = 1.70
R² = 0.88
γ = 1.59
R² = 0.86
γ = 1.0
(b)
γ = 2.0
γ = 1.79
R² = 0.83
γ = 1.75
R² = 0.89
γ = 1.74
R² = 0.90
γ = 1.68
R² = 0.82
γ = 1.47
R² = 0.82
γ = 1.0
(c)

Figure 5-8 The evolution of the normalized variance of MP streamwise displacement, $\sigma(\tau)^2/D_n^2$, for different bed roughnesses, k_s, over a dimensionless time span of $\tau u_*/D_n \approx 10$. The subplots (a), (b), and (c) correspond to k_s = 0.5 (R1-R3), 1.0 (R4-R6), and 2.5 mm (R7-R9), respectively. The dimensionless time span is divided into five logarithmically equal bins, marked by four dotted lines representing the bin boundaries ($\tau u_*/D_n$ = 0.17, 0.46, 1.29, and 3.59). Within each bin, a black dashed line represents a power law fit to the data points. The black and red dash-dotted lines illustrate the relationships $\sigma(\tau)^2/D_n^2 \sim (\tau u_*/D_n)^2$ and $\sigma(\tau)^2/D_n^2 \sim \tau u_*/D$, respectively.

The impact of experimental conditions and MP properties on the variations in γ was then investigated by performing a multiple regression analysis with k_s, U, ρ_p, D_n, and *csf* as independent variables. The result showed that only k_s has a statistically significant effect on γ (p-value = $5.45\times10^{-4} < 0.05$). As k_s varied from 0.5 to 1.0 to 2.5 mm, average γ values varied from 1.73 to 1.69 to 1.66, respectively. This suggests that MPs diffuse slightly more slowly over rougher beds in the streamwise direction for the range of $\tau u_*/D_n$ values observed, 0.06 to 10.0.

To further explore potential variations in the diffusion regime over time, the observed dimensionless time span for each bed roughness condition was divided into five logarithmically equal bins. The data points within each bin were fitted, resulting in 15 γ values, each characterizing a diffusion process within a specific period of $\tau u_*/D_n$ for each k_s value. Analysis of the data plotted in Figure 5-8a-c showed that γ decreases with increasing $\tau u_*/D_n$ for the same k_s. Specifically, γ decreased by 14.7% from 1.97 to 1.68 in Figure 5-8a; by 14.1% from 1.85 to 1.59 in Figure 5-8b; and by 17.9% from 1.79 to 1.47 in Figure 5-8c. This decreasing trend between γ and $\tau u_*/D_n$ for the same bed roughness aligns with the numerical simulation results from Martin et al. (2012), where particle inertia plays a dominant role in streamwise diffusion processes for sediments in continuous movements. It indicates that variations in γ for MPs could also be linked to particle inertia. Specifically, the observed decrease in γ as $\tau u_*/D_n$ increases for MPs may be due to the gradual loss of particle inertia over time, resulting in a decrease in γ. Besides, although variables such as U, ρ_p,

D_n, and *csf* did not have a significant impact on γ in this study, their potential influence cannot be ruled out. Future research could explore the effects of these variables by examining a wider range of MP properties and experimental conditions. Furthermore, there is a need to investigate the diffusion process of mixtures of MPs with varying physical properties, as Martin et al. (2012) indicated that particle heterogeneity can affect the diffusive behavior.

5.5. Conclusion

In summary, this study presents, for the first time, a statistical analysis of the continuous near-bed movements of MPs with various physical properties (D_n = 0.32-0.42 cm; ρ_p = 1.20-1.40 g/cm^3; and *csf* = 0.58-0.89) under different experimental conditions. The findings contribute to the groundwork for the future development of MP bedload transport models and offer additional validation for modeling MP transport. Specifically, this study proposes a new formula [Eq. (5-7)] for predicting the ensemble mean streamwise velocity of MPs with low relative errors (5.2%), which takes into account bed shear velocity and critical shear velocity. The study also provides a description of the standard deviation of the streamwise MP velocity by including the particle Shields parameter [Eq. (5-8)]. Furthermore, the study highlights the stochastic nature of MP movements, identifying a normal distribution in streamwise MP velocity and super-diffusive behavior influenced by particle inertia. It indicates that accurately modeling the time-dependent transport rate of MPs requires accounting for both advection and diffusion processes, for which fractional advection-diffusion equations or random walk models may be suitable.

6. Statistical description of intermittent microplastic movements in rough bed flows[5]

6.1. Introduction

Microplastics (MPs), defined as plastics with a size less than 5 mm (Yu, Yao, et al., 2022), have emerged as one of the significant contaminants in aquatic systems. This recognition arises from their ubiquity, persistence (Thompson, 2015), capacity to carry other pollutants (Padervand et al., 2020), and potential toxicity to both human and aquatic organisms (Smith et al., 2018). Understanding the impact of microplastic (MP) pollution on marine and freshwater systems requires knowledge of the spatial and temporal distributions of MPs. This, in turn, requires an in-depth understanding of MP transport mechanisms, particularly in open channel flows, as rivers serve as major conduits for transferring MPs from terrestrial to aquatic environments such as lakes and oceans (Meijer et al., 2021).

MPs are characterized by a diversity of physical properties, including size, shape, and density. Based on the density of MPs (ρ_p) relative to that of the ambient fluid (ρ), MP transport in open channel flows can involve the movement of buoyant ($\rho_p < 1$ g/cm^3), neutrally buoyant ($\rho_p \approx 1$ g/cm^3), and negatively buoyant MPs ($\rho_p > 1$ g/cm^3). A recent study reported the retention of negatively buoyant MPs along the Rhône River in France (Mennekes & Nowack, 2023). The observation raises questions about the transport mechanisms that lead to the wide distribution of negatively buoyant MPs along the river. However, no clear explanations can be provided given the current lack of knowledge regarding the motion of negatively buoyant MP. Specifically, recent

[5] The content of this chapter is being prepared and will be submitted as a journal manuscript.

studies of negatively buoyant MPs have mainly focused on MP settling (Yu, Yao, et al., 2022) and the initiation of MP mobilization (Yu et al., 2023; Yu, Yao, et al., 2022), while research into near-bed movements (also referred to as bedload movements in this study) of negatively buoyant MPs after the initiation of transport remains in its infancy.

The observation of MP retention along the Rhône River indicates that most of the negatively buoyant MPs are transported discontinuously. It is important to recognize that bedload MPs can also move intermittently, alternating between resting and moving states (Campagnol et al., 2015). This intermittency is particularly pronounced under hydrodynamic conditions near the threshold for MP mobilization (Campagnol et al., 2015). As a result, MPs can exhibit stochastic behavior both temporally and spatially, influenced by near-bed turbulence, complex fluid-particle interactions, and particle-bed collisions (Campagnol et al., 2015). Negatively buoyant MPs vary in size, density, and shape and the potential impacts of each of these independent variables further complicate research into MP movements and should be considered. To date, there are no experimental studies on the bedload movement of MPs with varying physical properties, while accounting for the intermittency and stochastic nature of their movement.

To address this gap, a series of tracking experiments were conducted for three types of MPs under hydrodynamic conditions near their respective mobilization thresholds. Given the stochastic nature of MP intermittent movement, this study presents a probabilistic description of the key kinematic variables that are critical for the future development and validation of bedload MP transport models. These variables include MP velocity, hop length, and the associated hop duration of complete hop events.

6.2. Literature review

Research on the intermittent movements of MPs may benefit from the relevant concepts and results of sediments, a field that has been developing for decades (Ancey, 2020). This section briefly reviews recent findings related to key kinematic parameters in sediment studies since no intermittent movement studies have been reported on MPs. Note that the bedload transport problem is commonly idealized as a streamwise transport process, where uniform-sized sediments are transported under equilibrium conditions with the rates of entrainment and disentrainment equal (Wu et al., 2020). This simplification is applicable throughout this section.

The probability density distribution of the streamwise particle velocity (v_x) plays a crucial role in describing both the transport rate and particle diffusion (Furbish et al., 2012). This distribution is typically investigated experimentally using particle tracking velocimetry. Experimental evidence suggests that under subcritical flow conditions, the distribution of v_x tends to be an exponential probability density function (PDF) (Fathel et al., 2015; Lajeunesse et al., 2010; Roseberry et al., 2012), which can be approximated by:

$$f_p(v_x \geq 0) = \frac{1}{\langle v_x \rangle} e^{-v_x / \langle v_x \rangle} \tag{6-1}$$

where the angle brackets denote the ensemble mean. Under supercritical flow conditions, the distribution of v_x tends to be Gaussian (Ancey & Heyman, 2014; Heyman et al., 2016). Ancey and Heyman (2014) described the velocity evolution of a bedload particle as a mean-reverting process and suggested that v_x can be described by a truncated Gaussian distribution as follows:

$$f_p(v_x \geq 0) = \sqrt{\frac{2}{\pi}} \frac{\eta}{1 + erf\left(\frac{\eta}{\sqrt{2}} v_m\right)} e^{\left[-\eta^2 \frac{(v_x - v_m)^2}{2}\right]} \tag{6-2}$$

where η and v_m are fitted parameters, and *erf* is the error function.

The difference in the distributions of v_x under different types of flows can be linked to the presence of different sediment transport regimes. These regimes were identified through a relationship between the streamwise hop length (L_x) and hop duration (T_{tr}), where L_x is the streamwise displacement of a particle from the start of its movement until it comes to rest, and T_{tr} is the time the particle spends during the hop (Wu et al., 2020; Wu et al., 2021). Wu et al. (2021) applied a nonlinear transformation to map v_x to a scaled velocity within the diffusion equation to describe the distribution of v_x (Wu et al., 2021). This transformation enables the derivation of this relationship between L_x and T_{tr}:

$$L_x(T_{tr}) = \langle v_x \rangle T_{tr} + 4\langle v_x \rangle \sum_{n=1}^{\infty} \frac{1 - e^{-D\beta_n^2 T_{tr}/2}}{D\beta_n^3} \cos(\beta_n) Si(\beta_n) \tag{6-3}$$

where n is the counting variable, D is the diffusion coefficient (s^{-1}), and *Si* is the sine integral function. D could be estimated through a trial-and-error process using the experimental data for L_x, T_{tr}, and ‹v_x›. Eq. (6-3) indicates that $L_x \propto T_{tr}$ for $T_{tr} > 1/D$, which corresponds to the Taylor dispersion regime, and the hops within this regime are defined as "long hops" (Wu et al., 2021). For $T_{tr} < 0.1/D$, $L_x \propto T_{tr}^{1.5}$, which is referred to as the initial regime. The regime with $1/D > T_{tr} > 0.1/D$ is referred to as the transition regime, where the scaling exponent of the L_x and T_{tr} relationship > 1.5, typically ~5/3. Hops within the initial and transition regimes are defined as "short hops" (Wu et al., 2021). For example, if $D = 1.0$ s^{-1}, when $T_{tr} > 1.0$ s, $L_x \propto T_{tr}$; when $T_{tr} < 0.1$ s, $L_x \propto T_{tr}^{1.5}$; and when $0.1 \text{ s} \leq T_{tr} \leq 1.0$ s, $L_x \propto T_{tr}^{\sim 5/3}$. The mix of short and long hops leads to

an exponential-like distribution of v_x, while long hops alone result in a Gaussian-like distribution (Wu et al., 2021). Wu et al. (2021) reported that the distribution of T_{tr} can be expressed analytically as (Wu et al., 2021):

$$f_p(T_{tr} > 0) = \frac{1}{\langle T_{tr} \rangle} e^{-T_{tr}/\langle T_{tr} \rangle} \tag{6-4}$$

Based on Eqs. (6-3) and (6-4), Wu et al. (2021) proposed an explicit estimation of the distribution of L_x for long hops:

$$f_p(L_x > 0) = \frac{1}{\langle v_x \rangle \langle T_{tr} \rangle} e^{-L_x/\langle v_x \rangle \langle T_{tr} \rangle} \tag{6-5}$$

6.3. Methodology

6.3.1. MP properties, experimental conditions, and setup

Three types of MPs were used in this study: Polyamide (PA), Polyvinyl chloride (PVC), and Polyethylene terephthalate (PET) particles. The nominal diameters D_n and the particle density ρ_p of the selected MPs range from 0.28 to 0.42 cm, and from 1.20 to 1.40 g/cm^3, respectively. The dimensionless particle diameter D_*, defined as $\left[\frac{(\rho_p - \rho)g}{\rho \upsilon^2}\right]^{1/3} D_n$, ranges from 39.32 to 55.59. The shape of MPs was quantified by the Corey's shape factor (*CSF*), which is defined as $c/(ab)^{1/2}$ (where a, b, and c are the lengths of the longest, intermediate, and shortest sides of a particle, respectively) (Yu, Yang, & Zhang, 2022). The *csf* values for PA, PVC, and PET fall within the range of 0.66 to 0.89. Detailed MP properties information is listed in Table 6-1.

Table 6-1 Summary of MP properties and hydrodynamic conditions. D_n is the nominal diameter, ρ_p is the MP density, *CSF* is the Corey's shape factor, D_* is the dimensionless particle size, U_c is the critical flow velocity for MPs, U is the flow velocity, *Re* is the Reynolds number, *Fr* is the Froude number, u_* is the shear velocity, and k_s^+ is the roughness Reynolds number.

Case	Material	D_n (cm)	ρ_p (g/cm^3)	*CSF*	D_*	U_c (cm/s)	U (cm/s)	*Re* (×10^4)	*Fr*	u_* (cm/s)	k_s^+
1	PA	0.32	1.20	0.66	39.32	10.59	12.18	5.15	0.059	0.54	2.63
2	PVC	0.42	1.25	0.89	55.59	13.56	15.60	6.60	0.076	0.68	3.32
3	PET	0.28	1.41	0.74	43.70	14.83	15.58	6.59	0.075	0.67	3.26
4	PET	0.28	1.41	0.74	43.70	14.83	17.06	7.22	0.083	0.73	3.55

Experiments were conducted in a 7.50 m long, 0.75 m wide, and 0.50 m deep recirculating flume with a 0.2% slope. A sketch of the flume and detailed configuration information can be found in Chapter 5. The longitudinal flow direction was defined as the x coordinate and y and z as the cross stream and vertical directions, respectively. The water depth was held constant at $H = 43.5 \pm 0.5$ cm for all experiments. A fixed rough bed with a roughness (k_s) of 0.5 mm, previously utilized for examining MP continuous movements (Chapter 5), was used to maintain consistency. The use of a fixed bed implies that the potential influences of bedforms, as well as the burial and reappearance of MPs, were ignored for the sake of simplification. Flow velocities (U) were set at values slightly greater than the critical flow velocities (U_c) required for initiating the movement of PA, PET, and PVC on a fixed rough bed with $k_s = 0.5$ mm (Yu, Yao, et al., 2022). Measurements were conducted for the following four cases: PA, PET, and PVC with the flow velocity set to $U/U_c = 1.15$ and PET with $U/U_c = 1.05$, which were labeled cases 1-4 (see Table 6-1). The Reynolds number *Re* ($= UH/\nu$) ranged from 5.15×10^4 to 7.22×10^4 and the Froude number *Fr* ($= U/(gH)^{0.5}$) from 0.059 to 0.083, which resulted in fully turbulent and subcritical flows for all cases. The shear velocities u_* for each

flow condition were estimated using the turbulent kinetic energy method, as described in detail in a previous study (Yu, Yao, et al., 2022). In all cases, the roughness Reynolds number k_s^+ (= $u_* k_s/\nu$) ranged from 2.63 to 3.55, which is below the transitionally rough limit of 5 (Dey, 2014), and therefore the beds can be characterized as hydraulicly smooth. Preliminary tests confirmed the occurrence of intermittent near-bed movements of MPs in all cases. The flow parameters described above are all listed in Table 6-1.

For consistency, this study employed the same experimental setup for particle tracking as was used in a previous study (Chapter 5) on continuous MP movements, including the light source (*QL-1000*), camera model (*GoPro Hero 8*), and MP releasing ramp, as described in Chapter 5. Images with a resolution of 2704 pixels ×1520 pixels were recorded at a frequency of 30 fps. To eliminate reflections and refractions due to water-surface undulations, the camera was pointing vertically downward at the central observation area with the lens ~20 cm below the water surface. The field of view covered an area of 30.0 cm × 17.0 cm. In preparation for the experiments, the camera was calibrated, following the procedure outlined in Chapter 5. The mean reprojection error was ~0.7 pixels (< 1.0 pixel) which is an acceptable accuracy (Shortis, 2015).

6.3.2. Experimental procedures and image processing

This study included 80 experimental tests, including 4 different experimental cases, with 20 repetitions per case. Consistent experimental procedures were strictly followed in each test. First, the variable frequency drive of the pump was adjusted to achieve the target flow velocity. Once the flow reached a stable state, 25 MPs of a certain type were simultaneously released 3.54 cm underwater, 2.50 m downstream from the flume entrance, and their movements within the field of view were recorded for a duration of 35 s. Throughout this duration, the majority of the MPs

exhibited alternating states of rest and motion. After the recording concluded, any remaining MPs within the field of view were flushed out to clear the area. This procedure was repeated for each of the 80 tests.

A series of consecutive raw images was extracted from the recorded image sequences. The extracted images were converted to grayscale and the average background intensity was subtracted using *ImageJ*. The plugin in *ImageJ* (*Trackmate* (Tinevez et al., 2017)) was used to identify MPs in each frame of the image sequence, match the detected MPs across frames, and generate tracks. Figure 6-1a presents the trajectories of three tracked MP particles obtained from one of the Case 2 recordings. The generated trajectories were then analyzed to determine the variables of interest. The instantaneous particle velocities in the streamwise and cross-stream direction (v_x, v_y) were computed by dividing the streamwise and cross-stream displacements by the time interval of Δt = 1/30 s. To determine hop length and hop duration from the obtained trajectories, it was first necessary to define a "hop". This study adopted a binary approach to MP intermittent movements, classifying MPs as either "in motion" or "at rest" at any given moment, represented by the Boolean variable M (1 for motion, 0 for rest). A complete hop event for an MP particle was thus defined as an uninterrupted period of motion, characterized by transitions from a rest state to motion and back to rest.

To distinguish between the "in motion" and "at rest" states during MP intermittent movements, three thresholds were set. First, a streamwise particle velocity of 0.20 cm/s was selected and confirmed visually to be generally effective for distinguishing between these states. Therefore, a MP particle was considered to be at rest (M = 0) when v_x < 0.20 cm/s, otherwise in motion (M = 1). However, applying this velocity threshold alone occasionally resulted in brief (1-3 frames) "in

motion" states within a long period of rest, or a brief "at rest" state between two long periods of motion. These brief events required further evaluation.

In experimental studies of sediments, temporal or spatial thresholds were commonly proposed to identify and exclude impulsive events of motion or rest that have negligible contributions to net sediment transport (Cecchetto et al., 2018; Liu et al., 2019). Assuming the filtering of impulsive events was suitable for MP transport, this study adopted explicit temporal and spatial thresholds from a sediment study (Cecchetto et al., 2018) for MPs. Specifically, if a MP particle performed a short hop with a net resultant displacement of less than one nominal diameter, the corresponding "in motion" states were considered impulsive and reclassified as "at rest". If a MP resting duration was shorter than 0.10 s, the corresponding "at rest" state was reclassified as "in motion". Note that applying these parametric thresholds may introduce errors to the variables of interest. Quantifying these errors is challenging due to the lack of theoretical knowledge of MP intermittent movements and the absence of direct numerical simulations capable of accurately determining the true temporal or spatial coordinates where MPs are at rest or in motion. Furthermore, there is no preference or universal threshold that can be applied (Hosseini-Sadabadi et al., 2019). Consequently, the thresholds used to distinguish between "in motion" and "at rest" states were specific to current experimental conditions and should be viewed as a temporary solution for accurately describing MP intermittent movements.

Figure 6-1b-d illustrates a complete hop event that occurred between 18.73-19.43 s within trajectory A (Figure 6-1a), along with its corresponding time evolutions of streamwise displacement, velocity, and Boolean variable. The number of complete hop events (N) varies from 279 (case 2) to 962 (case 3) across different cases (Table 6-2), which is comparable to those of the

previous sediment studies (N = 60 - 1421) (Ancey, 2020; Campagnol et al., 2015; Hosseini - Sadabadi et al., 2019; Liu et al., 2019).

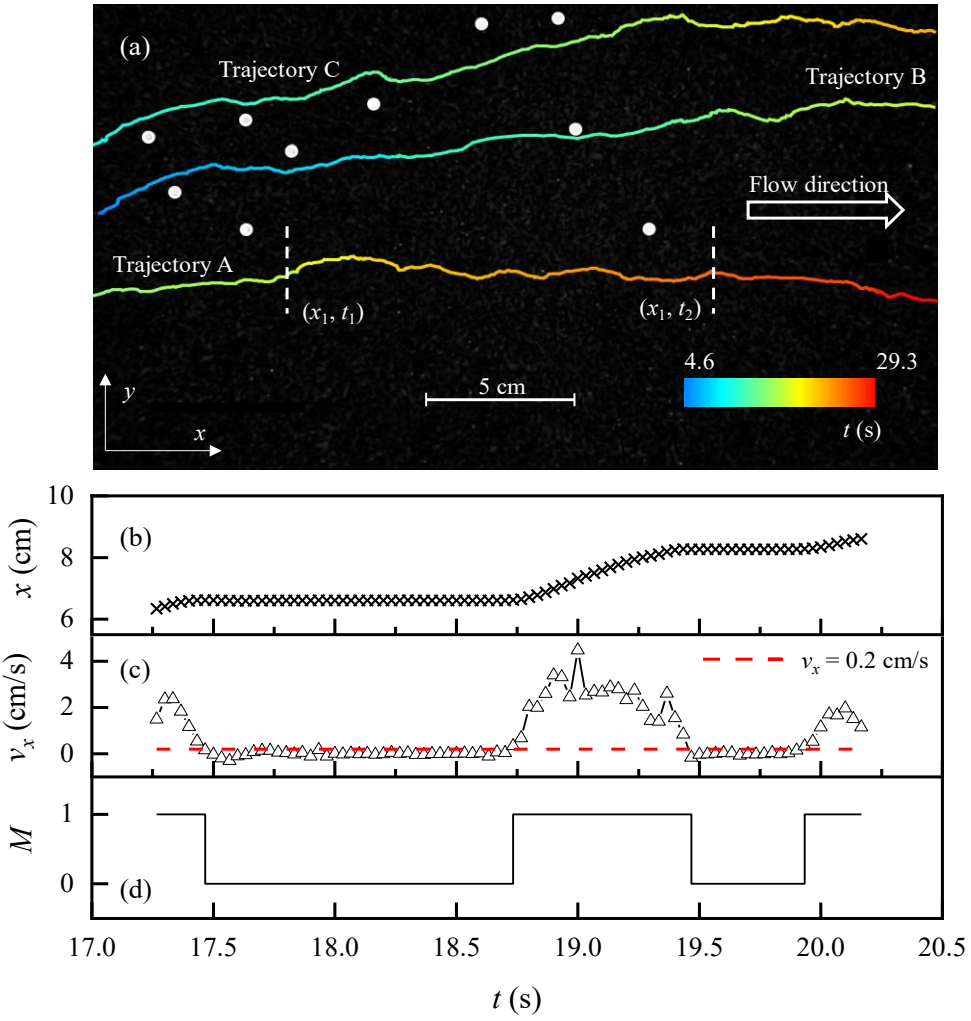

Figure 6-1 (a) Illustration of sampled trajectories (A, B, C) of three PET particles during a time interval spanning from 4.6 to 29.3 s, extracted from one of the repetitive tests of case 3. These trajectories are superimposed onto the frame at t = 29.3 s. The variation in color of the trajectories is representative of the time evolution. The white dots indicate the spatial coordinates of the remaining PET particles at the time instance t = 29.3 s. (b) The time series of the streamwise particle displacement (x) over a defined duration (from t_1 = 17.3 s to t_2 = 20.2 s, marked by two dashed lines) within trajectory A. (c) The corresponding time series of the streamwise particle velocity (v_x) and (d) the Boolean variable (M) over the same duration within trajectory A.

6.3.3. Error analysis

This study identified and assessed two main sources of errors. First, the determination of the centroids of MPs in *TrackMate* has a sub-pixel accuracy (commonly < 0.5 pixels) (Ashley et al., 2020). When combined with a reprojection error of approximately 0.7 pixels, a maximum uncertainty of two pixels in the determination of MP centroids can be reasonably assumed. This uncertainty corresponds to about 6% of a particle size and the measured shortest hop length. Consequently, it results in a maximum uncertainty of 0.05 mm/s for the ensemble mean velocity for all cases, which was obtained by considering the error propagation over the minimum sample size of v_x for case 4 (19044). The uncertainty associated with the MP centroid determination can be positive or negative and unlikely to bias the estimated mean velocity or hop length. The influence of this error on the primary findings of this study regarding both the relative magnitudes and shapes of the probability distributions of v_x, L_x, and T_{tr}, is considered minimal (Ashley et al., 2020; Liu et al., 2019).

Second, applying a binary view on MP intermittent movements in particle tracking experiments introduces a negative bias error in the observed hop durations. This bias occurs because, in this study, MPs were identified as "in motion" (M = 1) in the first image sampled after the actual initiation of mobilization and as "at rest" (M = 0) in the image sampled just prior to the actual cessation of mobilization. Assuming that the timing of the initiation and the timing of the cessation of mobilization within a given frame interval are each independently normally distributed, the most likely error for a single observed hop duration is approximately 1/30 s, which is considered acceptable (Ashley et al., 2020). Increasing the camera frequency can reduce the magnitude of this bias, while it will increase the uncertainty in particle velocity measurements. For example, increasing the frequency to 120 fps will increase the uncertainty in v_x from ~0.66 cm/s to ~2.66

cm/s. Therefore, the current camera frequency was chosen as a compromise to balance temporal resolution and measurement accuracy.

6.4. Results and discussion

Figure 6-2 illustrates the probability density distributions of the instantaneous orientation angle, θ, for different cases. The value of θ is calculated as $\tan^{-1}(v_y/v_x)$. All distributions follow a normal distribution and are approximately symmetric around $\theta = 0°$. The standard deviation of θ, denoted as $\sigma(\theta)$, is similar for different cases, with an average value of ~21 ° (see Table 6-2). This indicates that two-thirds of the tracked MPs deviated by less than ±21° from the streamwise direction, which is considered to be a fairly moderate spreading. It is reasonable to assume that the intermittent movements of MPs are predominantly in the streamwise direction. Furthermore, the ensemble means of streamwise MP acceleration for cases 1-4 are 0.043, 0.046, 0.14, and 0.10 cm/s^2, respectively. These values are close to zero, showing that external forces acting on MPs are minimal, which shows that the transport of MPs in each case can be considered in a state of equilibrium (Wu et al., 2020). Therefore, this study focuses on the idealized cases of uniform MPs being transported under equilibrium conditions and the streamwise MP transport processes are of particular interest.

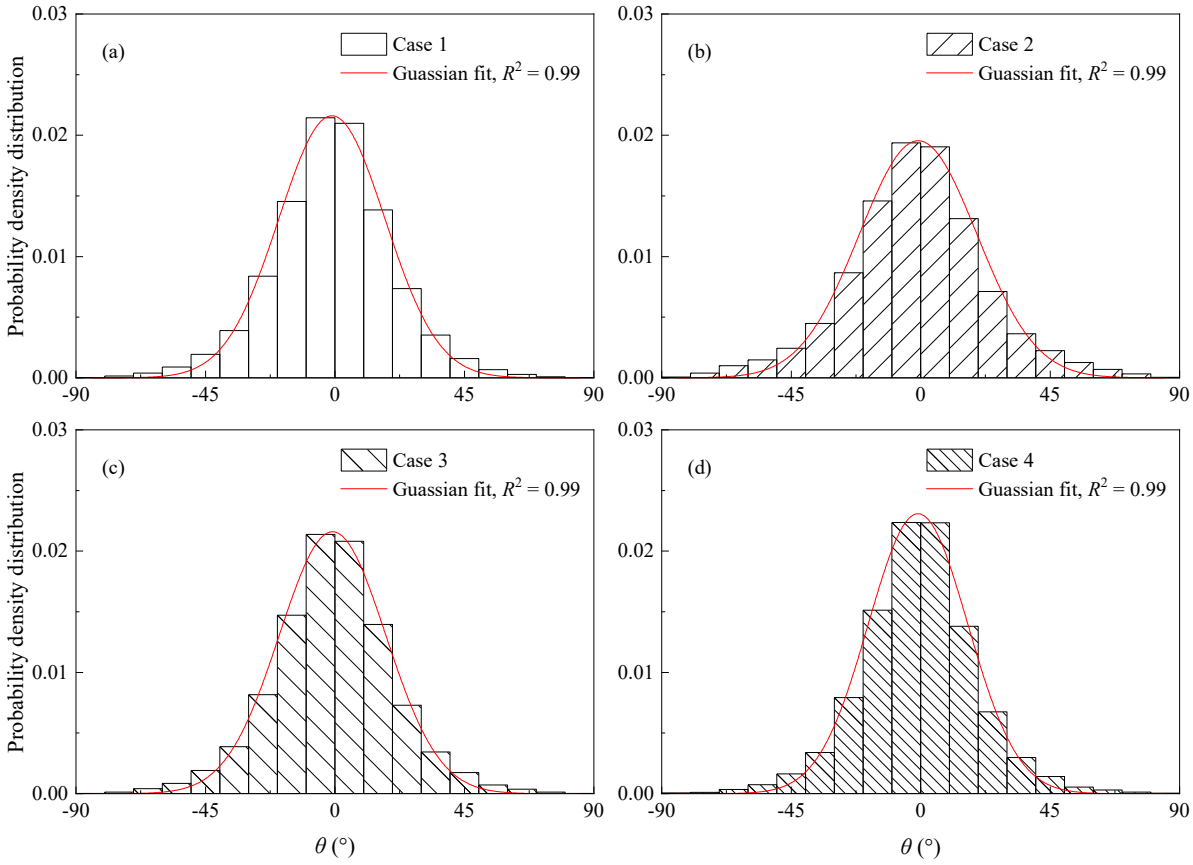

Figure 6-2 The probability density distributions of the orientation angles (θ) for (a) case 1, (b) case 2, (c) case 3, and (d) case 4. The red lines indicate the fitted *pdf*s.

Table 6-2 Statistical characteristics of the kinematic variables of cases 1-4.

Case	**Unit**	**1**	**2**	**3**	**4**
N		494	279	962	744
$\langle\theta\rangle$	°	-0.93	-0.88	-0.72	-0.88
$\sigma(\theta)$	°	20.42	23.46	20.62	19.62
$\langle v_x\rangle$	cm/s	1.96	3.15	2.44	2.86
η	s/cm	0.92	0.61	0.64	0.59
v_m	cm/s	1.79	3.13	2.18	2.58
$\langle v_x\rangle_{pre}$	cm/s	1.25	2.28	1.95	2.74
$\sigma(v_x)$	cm/s	1.01	1.51	1.35	1.55
$CV(v_x)$		0.52	0.48	0.55	0.54

$\langle L_x \rangle$	cm	4.61	7.17	3.47	4.96
$\sigma(L_x)$	cm	4.99	6.18	3.56	4.95
$CV(L_x)$		1.08	0.86	1.03	1.00
$\langle T_{tr} \rangle$	s	2.35	2.28	1.42	1.73
$\sigma(T_{tr})$	s	2.18	1.70	1.16	1.43
$CV(T_{tr})$		0.93	0.75	0.82	0.82
D	s^{-1}	0.81	0.96	1.19	0.93
T_c	s	0.090	0.071	0.059	0.068

6.4.1. MP velocity

Figure 6-3 presents the probability density distributions of v_x for cases 1-4. In each case, v_x follows a truncated Gaussian distribution and can be accurately modeled using Eq. (6-2). For all cases, the values of R^2 exceed 0.98. Table 6-2 lists the fitting parameters η and v_m from Eq. (6-2) for each case. The truncated Gaussian distribution is thin tailed, which is expected because particles typically do not move faster than the flow which limits the maximum v_x values that are attainable.

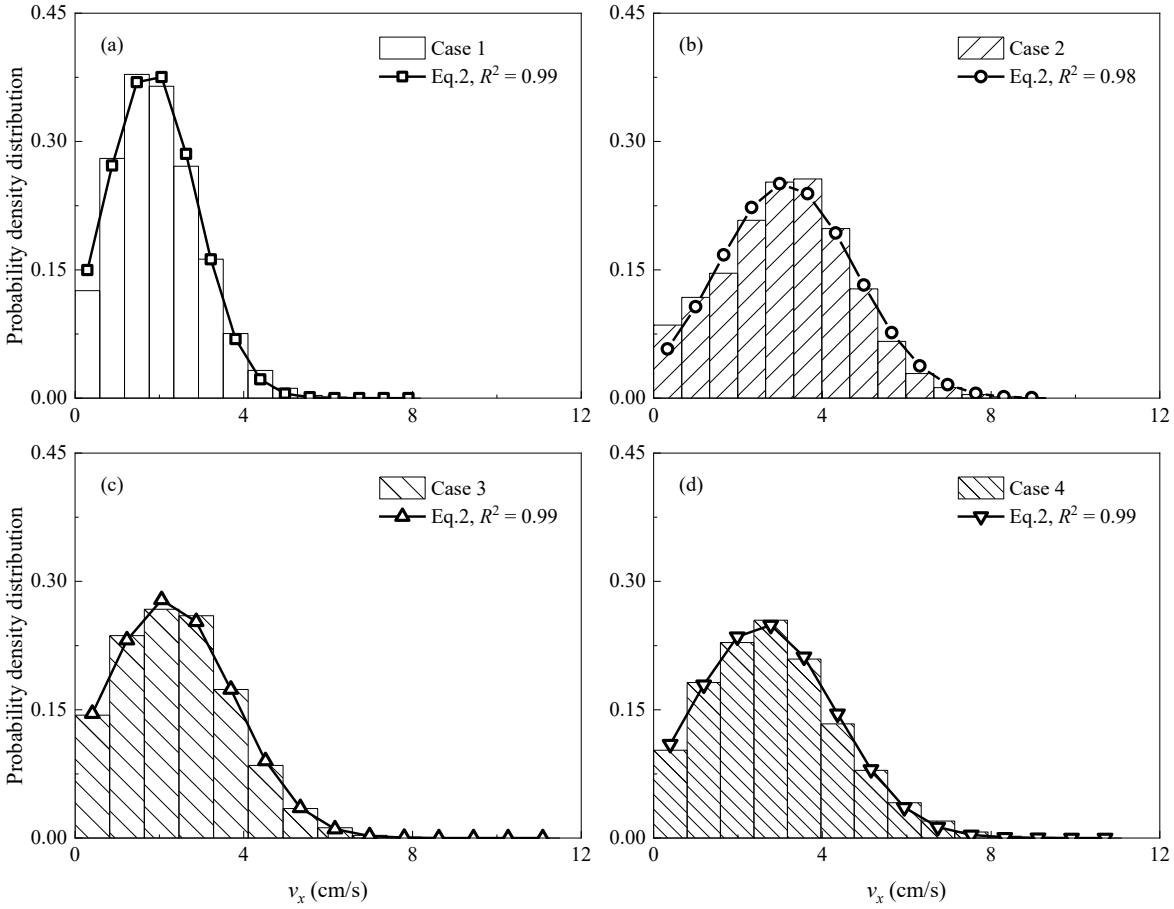

Figure 6-3 The probability density of the streamwise MP velocity (v_x) for (a) case 1, (b) case 2, (c) case 3, and (d) case 4. The datapoints along with the lines connecting them illustrate the fit of Eq. 6-2 for each case.

The presence of a truncated Gaussian distribution of v_x means that both its ensemble mean and standard deviation [$\sigma(v_x)$] are finite. To compare the measured values, the following formula previously proposed for continuously moving MPs (Chapter 5) was used to predict ‹v_x›:

$$\langle v_x \rangle = 13.67\left(u_* - 0.76u_{*_c}\right) \tag{6-6}$$

where u_{*c} is the critical shear velocity and can be estimated from Eq. 9 in Yu et al. (2023). The predicted values of ‹v_x›, ‹v_x›$_{pre}$, are presented in Table 6-2. Eq. (6-6) underestimates ‹v_x› for all

cases, which is expected considering that this equation was developed using v_x datasets that exhibited a Gaussian distribution without truncation. Some of the differences between predicted and observed v_x values can also be explained by the definition of the resting and motion states of MPs. Nevertheless, given that the magnitude of the relative error is small (21.97%), Eq. (6-6) is still considered to provide reasonable estimates of $\langle v_x \rangle$ for MPs conducting intermittent movements. Additionally, the standard deviations of v_x [$\sigma(v_x)$] range from 1.01 to 1.55 cm/s across different cases (Table 6-2). To compare the degree of variation of v_x, the coefficients of variation of v_x [$CV(v_x)$] were calculated and found to be similar across cases (Table 6-2). This similarity is likely due to the similar flow conditions (all near the threshold for initiation of mobilization) and the limited range of MP properties considered, which leads to comparable frequencies and intensities of collisions between the MPs and the underlying bed.

Notably, under the same subcritical flow conditions, v_x follows a truncated Gaussian distribution for MPs in this study, whereas v_x in sediment studies has commonly been reported to follow an exponential distribution (Wu et al., 2020). Before exploring the reasons behind this difference, it is crucial to first understand the presence of the truncated Gaussian distribution by examining the impact of long or short hops of MPs.

6.4.2. The hop length and hop duration of MPs

Figure 6-4 and Figure 6-5 present the probability density distributions of T_{tr} and L_x for all cases, respectively. These plots show that the distributions of both L_x and T_{tr} appear to be exponential. This is not unexpected because the values of $CV(L_x)$ = 0.86-1.08, and $CV(T_{tr})$ = 0.75-0.93 (Table 2) are close to 1.0, which is the theoretical coefficient of variation for an exponentially distributed variable. The exponential distributions given by Eqs. (6-4) and (6-5) are good fits to the observed

distributions with R^2 values ranging from 0.94 to 0.99. The exponential distributions of L_x and T_{tr} are consistent with previous studies regarding the intermittent movements of sediments (Fathel et al., 2015; Liu et al., 2019). Furthermore, as previously mentioned, the presence of an exponential distribution of L_x indicates that the majority of MPs perform long hops (Wu et al., 2021).

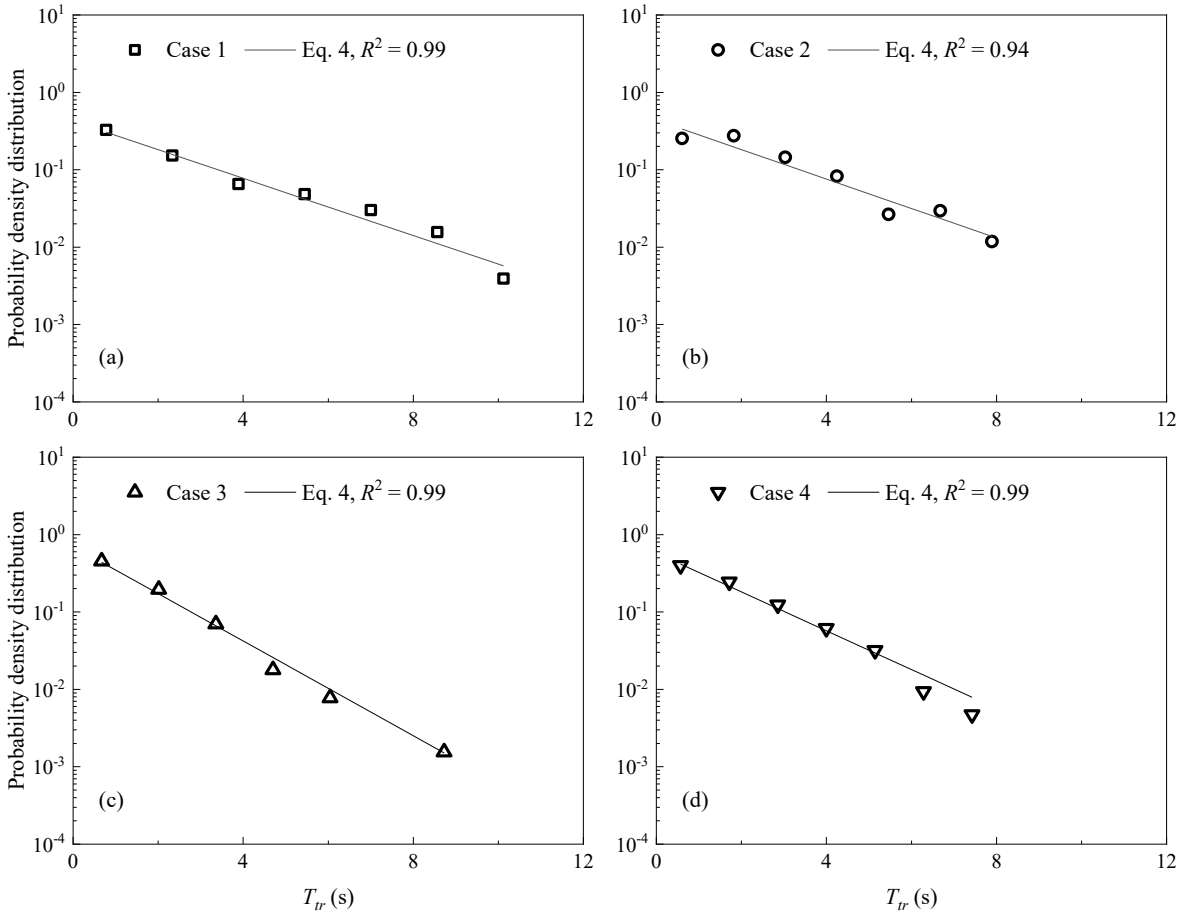

Figure 6-4 The probability density of the hop duration (T_{tr}) for (a) case 1, (b) case 2, (c) case 3, and (d) case 4. The black line represents Eq. 6-4.

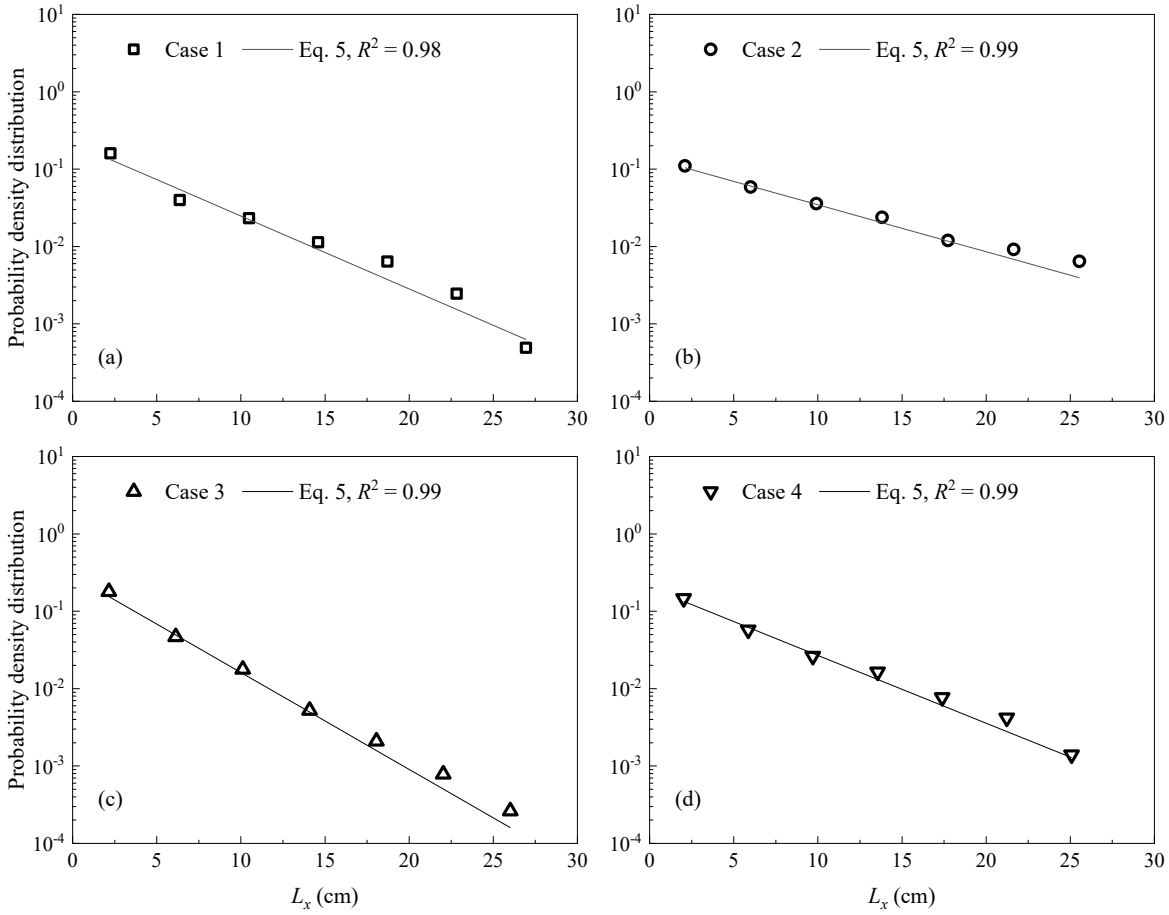

Figure 6-5 The probability density of the hop length (L_x) for (a) case 1, (b) case 2, (c) case 3, and (d) case 4. The black line represents Eq. 6-5.

To estimate the prevalence of long hop behavior, power law Eq. (6-3) was fitted to the measurements of L_x and T_{tr}. A log-log plot of L_x and T_{tr} in Figure 6-6 clearly shows that a power law relationship exists between these two variables. Eq. (6-3) was then fitted to the datapoints, and the value of D was obtained (Table 6-2). The corresponding values of R^2 are 0.92, 0.92, 0.88, and 0.89; the relative errors are 20.94%, 18.35%, 21.36%, and 20.76% for cases 1-4, respectively. The reciprocal of D, which marks the boundary between Taylor dispersion and the transition regime, ranges from 0.84 (case 3) to 1.24 s (case 1). The lower limit of the transition regime at $0.1/D$ therefore varies from 0.08 to 0.12. Figure 6-6 shows that all datapoints fall within the transition

and Taylor dispersion regimes. A significant percentage of the datapoints fall within the Taylor dispersion regime (59.11%, 74.55%, 60.29%, and 56.11% for cases 1-4, respectively), indicating prevalent long hop behavior. Furthermore, Figure 6-3 and Figure 6-6 together show that the presence of truncated Gaussian distribution of v_x can be attributed to a mix of short and long hops. This suggests that the transport of MPs in this study was occurring in both the transitional and Taylor dispersion regimes which results in short and long hops, respectively.

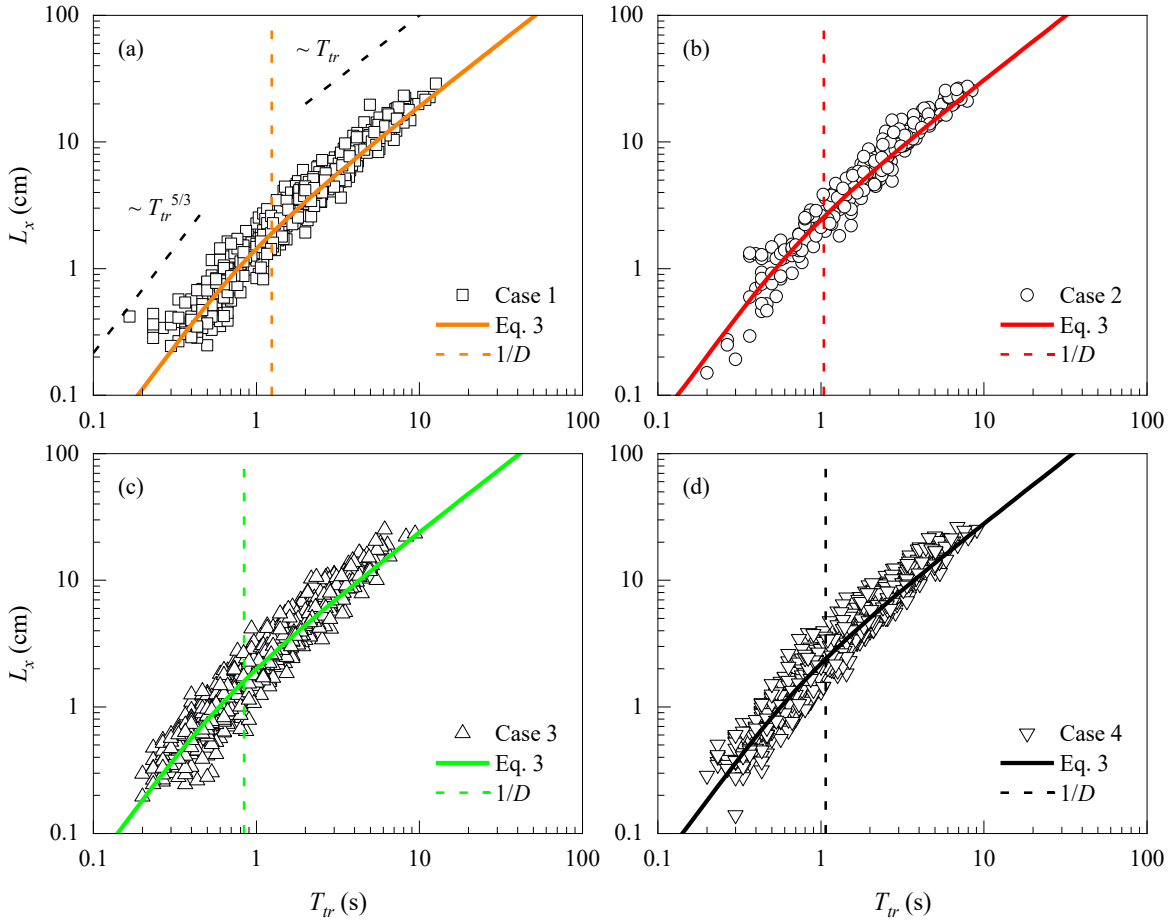

Figure 6-6 The relationships between the streamwise hop length (L_x) and the hop duration (T_{tr}) for (a) case 1, (b) case 2, (c) case 3, and (d) case 4. Each subplot illustrates the measured datapoints along with a colored solid line representing the fitted Eq. 6-3, and a vertical dashed line indicating the corresponding value of $1/D$. The black dashed lines in subplot (a) represent the slopes of $L_x \propto T_{tr}^{5/3}$ and $L_x \propto T_{tr}$, respectively.

As previously mentioned, numerical simulations of sediment transport indicated that the v_x distribution transitions from Gaussian, when considering only long hops, to exponential when both short and long hops are included. (Wu et al., 2020). To investigate if this is also the case the MPs used in this study, three characteristic time scales were set ($1/2D$, $1/D$, and $2/D$) to examine the effects of varying proportions of short and long hops. In each experimental case, filtering out hops with $T_{tr} \geq 1/2D$ removed all long hops, leaving only short hops, which constitute about 35% of the original short hop dataset. Filtering out hops with $T_{tr} \geq 1/D$ removed all long hops and retained all short hops in the original dataset. Filtering out hops with $T_{tr} \geq 2/D$ resulted in a mix of approximately 45% long hops and 55% short hops.

Figure 6-7 plots the v_x distribution for hops without any filtering (red open markers connected by lines) alongside the filtered hops based on the selected time scales across different cases. Comparing the v_x distributions of the unfiltered hops with $T_{tr} < 1/D$ and $2/D$, Figure 6-7 demonstrates that the mode of the distribution shifts leftward (indicating a decrease in the most likely value of v_x) as the proportion of long hops decreases. For hops with $T_{tr} < 1/2D$, the v_x distributions remain truncated Gaussian across all cases, with no exponential distributions observed. Therefore, Figure 6-7 shows that the presence of a truncated Gaussian distribution of v_x for MPs can also result from considering only short hops in the transitional regime. Furthermore, Figure 6-6 and Figure 6-7 indicate that the truncated Gaussian distribution may be an inherent characteristic of MPs moving intermittently on a fixed rough bed under flow conditions where $U/U_c \approx 1$.

There remains a question regarding the temporal or spatial scale at which the transition from a truncated Gaussian to an exponential distribution of v_x occurs for MPs. No clear answer can be provided in this study due to the absence of short hops within the initial regime (Figure 6-6).

Nevertheless, several avenues for future research are proposed. First, future experiments should track MP intermittent movements with higher spatial and temporal resolution, potentially using two or more spatially coupled high-speed cameras placed along the streamwise direction. This would allow for more accurate observation of short hops by reducing measurement errors in hop length and hop duration. Additionally, while the applied parametric thresholds for distinguishing between "in motion" and "at rest" states have kept measurement uncertainties within an acceptable range, as previously discussed, there is still a need to establish clear and universal thresholds for the intermittent movements of MPs with different physical properties. These thresholds would facilitate accurate observation of short hops on small time scales. Moreover, future experiments could explore weaker transport conditions than those used in this study or the use of mobile beds. Employing a mobile bed could be a key factor in the appearance of an exponential distribution of v_x for MPs. For example, Campagnol et al. (2015) reported an exponential distribution of v_x for Polybutylene terephthalate (PBT) with ρ_p = 1.27 g/cm^3 and D_n = 3.0 mm moving on a mobile bed under u_* = 2.0 cm/s.

Regardless of whether an exponential distribution of v_x for MPs is observed, it remains valuable to compare the dynamic characteristics of MPs and sediments exhibiting different types of v_x distributions under subcritical flow conditions. Such a comparison can be made using Lagrangian descriptions of their "in motion" states.

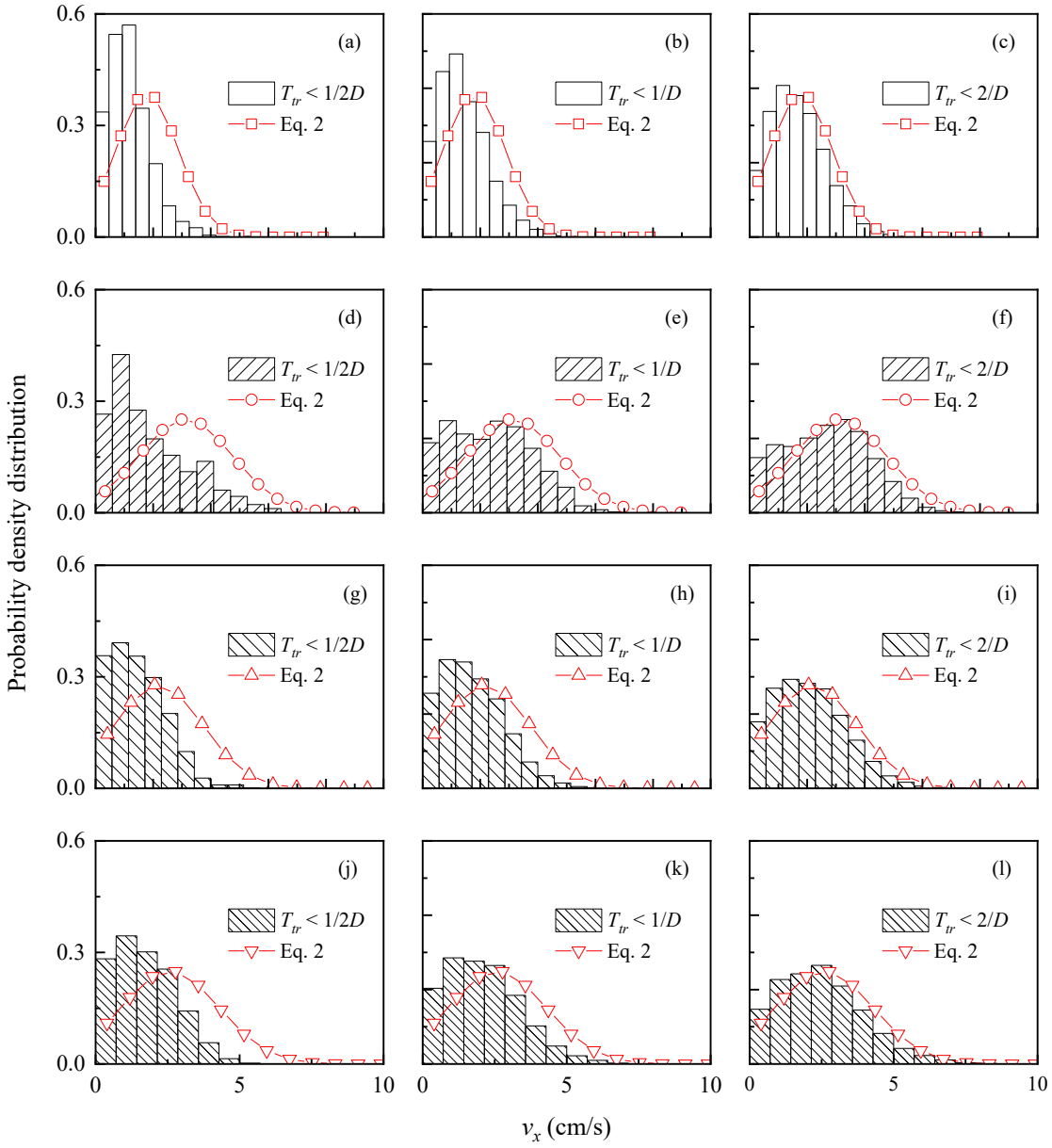

Figure 6-7 The distributions of v_x for MPs with hop durations of less than $1/2D$, $1/D$, and $2/D$ seconds for all cases are illustrated in subplots (a-c) for case 1, (d-f) for case 2, (g-i) for case 3, and (j-l) for case 4. In each subplot, lines connected by open markers depict the fit of Eq. 6-2 for each case, applied without data filtering.

6.4.3. Lagrangian description of moving MPs

The Lagrangian descriptions were developed by considering each single hop as an individual trajectory of a tracer. All tracers initiated their motion at $x = 0$ and at time $t_{pe} = 0$. Note that by definition t_{pe} is the time after the initiation of motion of a given MP particle. A dataset comprised of v_x values at different values of t_{pe} was assembled for each of the four cases. Note that detailed experimental trajectory data for sediments moving on fixed beds is scarce in the literature. To provide a comparison, alongside the cases examined in this study, data from the numerical study by Wu et al. (2020) of the time evolution of streamwise coordinates for sediments ($D_n = 0.05$ cm) moving under a flow shear velocity of 1.94 cm/s were collected, and the corresponding $\langle v_x \rangle_t$ values were calculated.

Figure 6-8a shows the variations of $\langle v_x \rangle_t$ as a function of t_{pe} for all cases in this study, along with the collected sediment data. In general, Figure 6-8a depicts two phases of MP and sediment movements. Initially, an accelerating phase in which $\langle v_x \rangle_t$ increased rapidly, followed by a quasi-steady phase wherein $\langle v_x \rangle_t$ stabilized at a constant value. Comparing the acceleration phase of MPs and sediments, Figure 6-8a shows that sediments reach a higher and approximately constant $\langle v_x \rangle_t$ faster than MPs in this study. This means that for the conditions in the Wu et al. (2020) simulations the sediment particles experienced on average a higher particle acceleration and achieved higher velocities compared to the MPs in this study. It is not unexpected because the sediments considered in Wu et al. (2020) are lighter (with $D_* = 12.64$) and were subjected to a stronger flow condition (represented by u_*) than MPs in this study ($D_* = 39.32$-55.59, $u_* = 0.51$-0.73 cm/s). As a result, the sediments experienced a higher driving force and exhibited greater particle acceleration on average compared to the MPs.

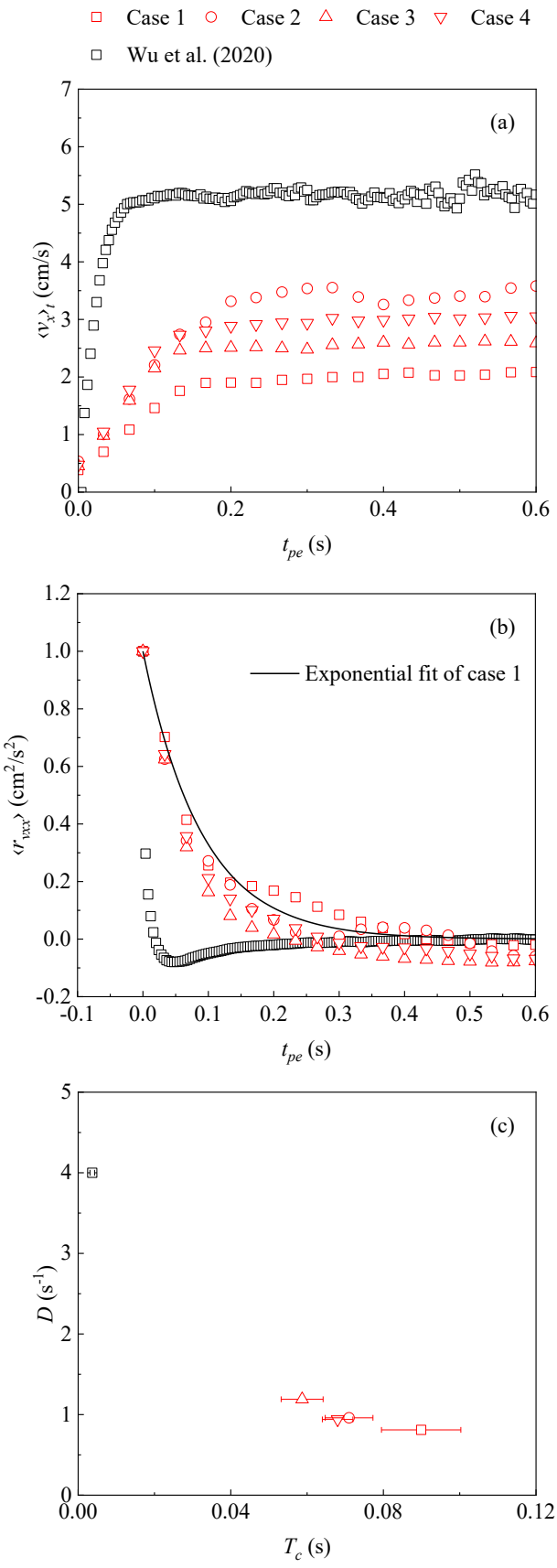
Case 1
Case 2
Case 3
Case 4
Wu et al. (2020)
(a)
$\langle v_x \rangle_t$ (cm/s)
t_{pe} (s)
(b)
Exponential fit of case 1
$\langle r_{vxx} \rangle$ (cm^2/s^2)
t_{pe} (s)
(c)
D (s^{-1})
T_c (s)

Figure 6-8 (a) The evolutions of the ensemble mean particle velocity, $\langle v_x \rangle_t$, with time, t_{pe}, for all four cases in this study and the numerical data for sediments in Wu et al. (2020). (b) The autocorrelations of the streamwise particle velocity, $\langle r_{vxx} \rangle$, for cases 1-4 and the numerical data. The black line represents an example of the exponential fit of case 1 with an exponent of 0.090. (c) The relationship of the diffusion coefficient, D, and the characteristic correlation time, T_c. The error bars represent the standard errors.

To further investigate the difference in the duration of the acceleration phase between MPs and sediments, the ensemble mean autocorrelation of v_x ($\langle r_{vxx} \rangle$) was calculated for all cases in this study, along with the numerical data from Wu et al. (2020). The v_x autocorrelation quantifies the degree of correlation between the values of v_x for a given time interval with the values of v_x at successive lagged time intervals (Martin et al., 2012; Pope, 2000). The value of r_{vxx} ranges from -1 to 1, and $r_{vxx} = 0$ represents a transition from uncorrelated ($r_{vxx} < 0$) to correlated motion ($0 < r_{vxx} \leq 1$) (Pope, 2000). The value of r_{vxx} at a given time lag for each case was computed as $\langle r_{vxx} \rangle$ for all tracers at that specific time lag, represented by t_{pe}.

Figure 6-8b compares the ensemble mean autocorrelations of v_x for MPs and sediments. For each case considered, $\langle r_{vxx} \rangle$ exhibits an exponential decay. The autocorrelation function for v_x can be described by e^{-t_{pe}/T_c}, where T_c is the characteristic correlation time scale, indicating the rate of autocorrelation decay (Martin et al., 2012). By applying an exponential fit to each case of MPs (an example of which is shown by the black line in Figure 6-8b), the T_c values were determined correspondingly and are 0.091, 0.071, 0.061 and 0.071 for cases 1-4, respectively (see Table 6-2). The T_c value for the sediment data is 0.0037 s, which is one order of magnitude smaller than that for MPs, highlighting a significantly faster decay in autocorrelation. A faster autocorrelation decay indicates a quicker loss of memory regarding the recent motions (Martin et al., 2012), which could be linked to a shorter acceleration phase (as seen in Figure 6-8a). In Eq. (6-3), the diffusion

coefficient D can be phenomenologically interpreted as a measure of how fast a particle can change its velocity during transport (Wu et al., 2020). Therefore, D and T_c could be correlated, and this relationship is shown in Figure 8c, where it is observed that an increase in T_c leads to a decrease in D.

Furthermore, the differences in characteristic correlation time scales among the different MP cases, as well as between MPs and sediments, can be attributed to differences in particle inertia. Particle inertia is related to the time required for a particle to respond to fluctuations in fluid drag (Martin et al., 2012). During the acceleration phase, the predominant forces acting on a particle include gravitational, lift, drag, and virtual mass forces. By performing a force balance of these forces, Oh and Tsai (2010) found that the particle response time (T_r) can estimated by:

$$T_r = \frac{\rho_p D_n^2}{18\mu(1+0.152Re_p^{0.5}+0.0151Re_p)} \tag{6-7}$$

where $Re_p = \rho D_n(U-\langle v_x \rangle)/\mu$ is the particle Reynolds number. For MPs in this study, T_r was estimated via Eq. (6-7) and found to be 0.079, 0.099, 0.065, and 0.062 s for cases 1-4, respectively. For sediments in Wu et al. (2020), T_r = 0.0078 s. These T_r values are comparable to the T_c values, indicating a significant impact of particle inertia on v_x autocorrelations.

Considering the correlation between the diffusion coefficient D and T_c shown in Figure 6-8c, D could be interpreted as a reflection of particle inertia, serving as a measure of how easily particles respond to flow drag. Specifically, compared to the numerical data of sediment, MPs in this study take longer to respond to flow drag, resulting in a prolonged acceleration phase before reaching a quasi-steady state for v_x. This extended acceleration phase is associated with the prevalence of long hops, which are characterized by a smaller diffusion coefficient. This suggests that MPs inherently

tend to perform longer hops due to their inertia. However, as previously discussed, given that various factors contribute to the prevalence of long hops and a truncated Gaussian v_x distribution in this study, the connection between D and particle inertia requires further validation through future experimental research.

6.5. Conclusions

A series of particle tracking experiments has been conducted to investigate the intermittent movements of angular-shaped MPs including PET, PVC, and PA, within a D_n range of 0.28-0.42 cm and a ρ_p range of 1.20-1.41 g/cm^3. Four different flow conditions were considered: three set at 1.15 times the critical flow velocity for each type of MP, and one at 1.05 times the critical flow velocity for PET. This study provided a statistical description of the key kinematic variables that describe MP movements for the first time, including MP velocity, hop length, and hop duration. The main findings can be summarized as follows:

1. Under subcritical flow conditions, the streamwise velocity of microplastics (MPs) followed a truncated Gaussian distribution. The mean velocity of MPs was predicted with reasonable accuracy using an existing formula (Eq. (5-7)) developed for continuous MP movements.

2. Both the hop length and hop durations follow exponential probability density distributions. The relationship between these two variables was well described by an analytical model previously applied to sediments [Eq. (6-3)]. A significant proportion of data falls within the Taylor dispersion regime where hop length varies linearly with hop duration.

3. A Lagrangian analysis of MP velocity reveals a two-phase movement pattern after the initiation of MP mobilization: an initial acceleration phase followed by a quasi-steady state

phase with approximately constant v_x. Compared to sediments, the selected MPs have a longer duration acceleration phase. Additionally, a negative relationship was identified between the diffusion coefficient in Eq. (6-3) and the characteristic correlation time scale, which describes the decay rate of velocity autocorrelation, as well as the particle response time associated with particle inertia. The diffusion coefficient can be thus interpreted as a measure of how easily particles respond to flow drag.

7. General conclusions and future research recommendations

7.1. General conclusions

Understanding the mechanisms of MP near-bed transport is crucial for developing a comprehensive description of MP transport and fate in aquatic environments, which has only been studied sporadically. This thesis investigates the impact of MP physical properties and flow conditions on key transport behaviors within the conceptualized MP near-bed transport process, including MP settling (Chapter 2), incipient motion of exposed (Chapter 3) and hidden MPs (Chapter 4), continuous movements (Chapter 5), and intermittent movements (Chapter 6). Specific conclusions have been made in each chapter, and general conclusions are provided herein:

1. In Chapter 2, it is suggested that both the particle sphericity and Corey's shape factor should be considered as shape descriptors when determining the drag coefficient associated with MP settling. Additionally, a new explicit model is proposed for estimating the drag coefficient and terminal settling velocity, applicable to the transitional regime.

2. Chapter 3 demonstrates the presence of a combined effect of bed roughness and MP properties on the incipient thresholds (flow velocity and critical shear stress) of exposed MPs. A new explicit formula for the critical shear velocity of incipient motion of exposed MPs is introduced, incorporating the dimensionless particle diameter and a new dimensionless parameter related to particle size, density, and shape.

3. In Chapter 4, a power-law relationship between critical shear stress and the density and size of hidden MPs is identified. A new empirical model for estimating critical shear stress, which implicitly considers the sheltering effect, is proposed. Furthermore, measures to

explicitly quantify the sheltering effects in MP mobilization are introduced, along with a semi-empirical method that incorporates these new measures for estimating the critical flow velocity.

4. Chapter 5 provides, for the first time, a statistical description of the continuous near-bed movements of MPs with various physical properties under different flow conditions. A new formula for predicting the ensemble mean streamwise velocity of MPs is proposed, accounting for the bed shear velocity and critical shear velocity. Additionally, a new formula for predicting the standard deviation of the streamwise MP velocity is provided, incorporating the particle Shields parameter. This chapter also finds a normal distribution in the streamwise MP velocity and reveals a super-diffusive behavior driven by particle inertia.

5. Chapter 6 presents a statistical analysis of key kinematic variables associated with the intermittent near-bed movements of MPs. It is found that the hop length and hop duration follow exponential distributions, while MP velocity follows a truncated Gaussian distribution. Furthermore, the presence of a truncated Gaussian distribution of MP velocity and a preference for longer hops are linked to particle inertia, suggesting that it is a fundamental characteristic of millimeter-sized MPs.

This thesis enhances our understanding of the transport of negatively buoyant MPs in open-channel flows by (a) introducing key concepts such as the sheltering effect in MP incipient motion and (b) presenting new equations for critical parameters such as the drag coefficient and ensemble mean MP velocity. The results of this thesis bring us closer to developing practical engineering solutions to key problems related to MP pollution in aquatic environments. For example, unanswered

questions remain about the transport of MPs in natural rivers and their distribution along and across the riverbed and in different aquatic regions. Given the limitations of localized sampling, such as funding constraints, numerical models offer an alternative solution. Insights into MP transport from a deterministic framework, such as incipient motion or settling in this thesis, can serve as a foundation for developing empirical equations in numerical models. Additionally, results from probabilistic frameworks, such as MP velocity distributions or MP hop length in this thesis, can help refine governing equations for MPs for improved accuracy of spatiotemporal predictions. Ultimately, the results in this thesis enhance our ability to assess the transport and extent of MP pollution, enabling the next-step development of site-specific mitigation and removal strategies.

7.2. Recommendations for future research

The transport mechanisms of MPs in natural flows are complex because they are influenced by a combination of physical and hydrological processes, including granular filtration, advective flow, and hyporheic exchange (Waldschläger et al., 2022). Additionally, the variability in plastic polymer characteristics, such as size, density, shape, surface roughness, and hydrophobicity, that play a key role in MP transport add to the complexity.

This thesis has made necessary simplifications to study key aspects of MP transport behavior, and as a result, the findings may be limited to specific flow conditions and MP characteristics, as discussed in Chapters 2–6. Site-specific conditions such as variations in flow and MP physical properties, can further restrict the broader applicability of the findings. These limitations pose challenges in applying the results to real-world MP transport in natural flows. For example, this investigation of incipient motion did not account for the influence of fluid density or salinity,

making the applicability of the proposed equations to environments like estuaries or salt marshes uncertain.

In conclusion, further research is necessary. Beyond the specific recommendations discussed in previous chapters, promising areas for future investigation include:

1. Effects of biofilm: Biofilm, composed of a variety of microorganisms, forms on the surface of MPs with a large surface-to-volume ratio, influencing MP properties such as density and stickiness. The impact of biofilm on the near-bed transport behavior of MPs has not been systematically studied and requires investigation. The results from this thesis on pristine MPs should be re-evaluated for biofilm-covered MPs.

2. Neutrally buoyant MPs: Neutrally buoyant MPs are suspended in the water column. Although much research has focused on their vertical distribution, their longitudinal and lateral distribution and transport have received less attention (Harris, 2020). Key transport behavior of suspended MPs requires future investigation, including aspects such as the threshold for initiation of suspension or re-suspension, diffusive behavior, and the development of mathematical models to describe the movements of suspended MPs with different polymer types.

3. Buoyant MPs: The floating ability of MPs could enhance the dispersal of MP pollution. While advancements have been made in modeling the transport of buoyant MPs in marine environments, crucial aspects of their transport in riverine environments remain unclear (Harris, 2020). Further research is needed to better understand the accumulation of floating MPs, their diffusion behavior, and the effects of river features, such as bends and riffles, on their movement and trapping.

Bibliography

Abbott, J., & Francis, J. R. D. (1977). Saltation and suspension trajectories of solid grains in a water stream. *Philosophical Transactions of the Royal Society of London. Series A, Mathematical and Physical Sciences*, *284*(1321), 225-254.

Acampora, H., Lyashevska, O., Van Franeker, J. A., & O'Connor, I. (2016). The use of beached bird surveys for marine plastic litter monitoring in Ireland. *Marine Environmental Research*, *120*, 122-129.

Aguirre-Pe, J., Olivero, M. L., & Moncada, A. T. (2003). Particle densimetric froude number for estimatingsediment transport. *Journa of Hydraulic Engineering*, *129*, 428-437.

Ahmadi, F., Ebrahimian, M., Sanders, R. S., & Ghaemi, S. (2019). Particle image and tracking velocimetry of solid-liquid turbulence in a horizontal channel flow. *International Journal of Multiphase Flow*, *112*, 83-99.

Akinwande, M. O., Dikko, H. G., & Samson, A. (2015). Variance inflation factor: as a condition for the inclusion of suppressor variable (s) in regression analysis. *Open Journal of Statistics*, *5*(07), 754.

Alcerreca, J. C., Silva, R., & Mendoza, E. (2013). Simple settling velocity formula for calcareous sand. *Journal of Hydraulic Research*, *51*(2), 215-219.

Ancey, C. (2020). Bedload transport: a walk between randomness and determinism. Part 1. The state of the art. *Journal of Hydraulic Research*, *58*(1), 1-17.

Ancey, C., Bigillon, F., Frey, P., Lanier, J., & Ducret, R. (2002). Saltating motion of a bead in a rapid water stream. *Physical Review. E, Statistical, nonlinear, and soft matter physics*, *66*, 036306.

Ancey, C., & Heyman, J. (2014). A microstructural approach to bed load transport: mean behaviour and fluctuations of particle transport rates. *Journal of Fluid Mechanics*, *744*, 129-168.

Armanini, A., & Gregoretti, C. (2005). Incipient sediment motion at high slopes in uniform flow condition. *Water Resources Research*, *41*(12).

Ashley, T. C., Mahon, R. C., Naqshband, S., Leary, K. C., & McElroy, B. (2020). Probability distributions of particle hop distance and travel time over equilibrium mobile bedforms. *Journal of Geophysical Research: Earth Surface*, *125*(7), e2020JF005647.

Avio, C. G., Gorbi, S., Milan, M., Benedetti, M., Fattorini, D., D'Errico, G., Pauletto, M., Bargelloni, L., & Regoli, F. (2015). Pollutants bioavailability and toxicological risk from microplastics to marine mussels. *Environmental Pollution*, *198*, 211-222.

Bai, Y., Wang, X., & Cao, Y. (2013). Incipient motion of non-uniform coarse grain of bedloadconsidering the impact of two-way exposure. *Science China Technological Sciences*, *56*, 1896-1905.

Baker, C. J. (1980). Theoretical approach to prediction of local scour around bridge piers. *Journal of Hydraulic Research*, *18*(1), 1-12.

Ballent, A., Pando, S., Purser, A., Juliano, M. F., & Thomsen, L. (2013). Modelled transport of benthic marine microplastic pollution in the Nazaré Canyon. *Biogeosciences*, *10*(12), 7957-7970.

Ballent, A., Purser, A., de Jesus Mendes, P., Pando, S., & Thomsen, L. (2012). Physical transport properties of marine microplastic pollution. *Biogeosciences Discussions*, *9*(12), 18755-18798.

Beheshti, A. A., & Ataie-Ashtiani, B. (2008). Analysis of threshold and incipient conditions for sediment movement. *Coastal Engineering*, *55*(5), 423-430.

Bergmann, M., Collard, F., Fabres, J., Gabrielsen, G. W., Provencher, J. F., Rochman, C. M., van Sebille, E., & Tekman, M. B. (2022). Plastic pollution in the Arctic. *Nature Reviews Earth & Environment*, *3*(5), 323-337.

Besseling, E., Quik, J. T., Sun, M., & Koelmans, A. A. (2017). Fate of nano-and microplastic in freshwater systems: A modeling study. *Environmental Pollution*, *220*, 540-548.

Biron, P. M., Robson, C., Lapointe, M. F., & Gaskin, S. J. (2004). Comparing different methods of bed shear stress estimates in simple and complex flow fields. *Earth Surface Processes and Landforms*, *29*(11), 1403-1415.

Bong, C. H., Lau, T. L., Ab, G. A., & Chan, N. W. (2016). Sediment deposit thickness and its effect on critical velocity for incipient motion. *Water Science and Technology*, *74*(8), 1876-1884.

Boskovic, N., Joksimovic, D., Perosevic-Bajceta, A., Pekovic, M., & Bajt, O. (2022). Distribution and characterization of microplastics in marine sediments from the Montenegrin coast. *Journal of Soils and Sediments*, *22*(11), 1-10.

Botterell, Z. L., Beaumont, N., Dorrington, T., Steinke, M., Thompson, R. C., & Lindeque, P. K. (2019). Bioavailability and effects of microplastics on marine zooplankton: A review. *Environmental Pollution*, *245*, 98-110.

Bravo, R., Ortiz, P., & Luis Pérez-Aparicio, J. (2018). Analytical and discrete solutions for the incipient motion of ellipsoidal sediment particles. *Journal of Hydraulic Research*, *56*(1), 29-43.

Brown, P. P., & Lawler, D. F. (2003). Sphere drag and settling velocity revisited. *Journal of Environmental Engineering*, *129*(3), 222-231.

Buffington, J. M., & Montgomery, D. R. (1997). A systematic analysis of eight decades of incipient motion studies, with special reference to gravel-bedded rivers. *Water Resources Research*, *33*(8), 1993-2029.

Campagnol, J., Radice, A., Ballio, F., & Nikora, V. (2015). Particle motion and diffusion at weak bed load: accounting for unsteadiness effects of entrainment and disentrainment. *Journal of Hydraulic Research*, *53*(5), 633-648.

Cao, Z., Pender, G., & Meng, J. (2006). Explicit formulation of the shields diagram for incipient motion of sediment. *Journal of Hydraulic Engineering*, *132*(10), 1097-1099.

Cecchetto, M., Tregnaghi, M., Bottacin-Busolin, A., Tait, S., Cotterle, L., & Marion, A. (2018). Diffusive regimes of the motion of bed load particles in open channel flows at low transport stages. *Water Resources Research*, *54*(11), 8674-8691.

Cheng, H., & Castro, I. P. (2002). Near wall flow over urban-like roughness. *Boundary-layer Meteorology*, *104*(2), 229-259.

Cheng, N. (1997). Simplified settling velocity formula for sediment particle. *Journal of Hydraulic Engineering*, *123*(2), 149-152.

Cheng, N. (2009). Comparison of formulas for drag coefficient and settling velocity of spherical particles. *Powder Technology*, *189*(3), 395-398.

Cheng, N., & Emadzadeh, A. (2014). Average velocity of solitary coarse grain in flows over smooth and rough beds. *Journal of Hydraulic Engineering*, *140*(6).

Cheng, N., Xu, P., Lu, Y., & Wei, M. (2022). Validation of bagnold's approximation of critical near-bed flow velocity for incipient sediment motion as particle settling velocity. *Journal of Hydraulic Engineering*, *148*(10), 06022012.

Chien, S. (1994). Settling velocity of irregularly shaped particles. *SPE Drilling & Completion*, *9*(04), 281-289.

Choi, S., & Kwak, S. (2001). Theoretical and probabilistic analyses of incipient motion of sediment particles. *KSCE Journal of Civil Engineering*, *5*(1), 59-65.

Chubarenko, I., Bagaev, A., Zobkov, M., & Esiukova, E. (2016). On some physical and dynamical properties of microplastic particles in marine environment. *Marine Pollution Bulletin*, *108*(1-2), 105-112.

Clift, R., & Gauvin, W. (1971). Motion of entrained particles in gas streams. *The Canadian Journal of Chemical Engineering*, *49*(4), 439-448.

Critchell, K., & Lambrechts, J. (2016). Modelling accumulation of marine plastics in the coastal zone; what are the dominant physical processes? *Estuarine, Coastal and Shelf science*, *171*, 111-122.

Dellino, P., Mele, D., Bonasia, R., Braia, G., La Volpe, L., & Sulpizio, R. (2005). The analysis of the influence of pumice shape on its terminal velocity. *Geophysical Research Letters*, *32*(21).

Dey, S. (2014). Fluvial hydrodynamics: hydrodynamic and sediment transport phenomena. In. Springer-Verlag.

Dey, S., & Ali, S. Z. (2017). Mechanics of sediment transport particle scale ofentrainment to continuum scale of bedload flux. *Journal of Engineering Mechanics*, *143*(11), 04017127.

Dioguardi, F., & Mele, D. (2015). A new shape dependent drag correlation formula for non-spherical rough particles. Experiments and results. *Powder Technology*, *277*, 222-230.

Dioguardi, F., Mele, D., & Dellino, P. (2018). A new one-equation model of fluid drag for irregularly shaped particles valid over a wide range of Reynolds number. *Journal of Geophysical Research: Solid Earth*, *123*(1), 144-156.

Drummond, J. D., Schneidewind, U., Li, A., Hoellein, T. J., Krause, S., & Packman, A. I. (2022). Microplastic accumulation in riverbed sediment via hyporheic exchange from headwaters to mainstems. *Science Advances*, *8*(2), eabi9305.

Duan, Z., Zhao, S., Zhao, L., Duan, X., Xie, S., Zhang, H., Liu, Y., Peng, Y., Liu, C., & Wang, L. (2020). Microplastics in Yellow River Delta wetland: Occurrence, characteristics, human influences, and marker. *Environmental Pollution*, *258*, 113232.

Enders, K., Käppler, A., Biniasch, O., Feldens, P., Stollberg, N., Lange, X., Fischer, D., Eichhorn, K.-J., Pollehne, F., Oberbeckmann, S., & Labrenz, M. (2019). Tracing microplastics in aquatic environments based on sediment analogies. *Scientific Reports*, *9*(1).

Fan, N., Xie, Y., & Nie, R. (2017). Bed load transport for a mixture of particle sizes: Downstream sorting rather than anomalous diffusion. *Journal of Hydrology*, *553*, 26-34.

Fan, N., Zhong, D., Wu, B., Foufoula-Georgiou, E., & Guala, M. (2014). A mechanistic-stochastic formulation of bed load particle motions: From individual particle forces to the Fokker-Planck equation under low transport rates. *Journal of Geophysical Research: Earth Surface*, *119*(3), 464-482.

Fathel, S., Furbish, D., & Schmeeckle, M. (2016). Parsing anomalous versus normal diffusive behavior of bedload sediment particles. *Earth Surface Processes and Landforms*, *41*(12), 1797-1803.

Fathel, S. L., Furbish, D. J., & Schmeeckle, M. W. (2015). Experimental evidence of statistical ensemble behavior in bed load sediment transport. *Journal of Geophysical Research: Earth Surface*, *120*(11), 2298-2317.

Fernandez Luque, R., & Van Beek, R. (1976). Erosion and transport of bed-load sediment. *Journal of Hydraulic Research*, *14*(2), 127-144.

Francalanci, S., Paris, E., & Solari, L. (2021). On the prediction of settling velocity for plastic particles of different shapes. *Environmental Pollution*, *290*, 118068.

Frings, R. M. (2008). Downstream fining in large sand-bed rivers. *Earth-science Reviews*, *87*(1), 39-60.

Furbish, D. J., Roseberry, J. C., & Schmeeckle, M. W. (2012). A probabilistic description of the bed load sediment flux: 3. The particle velocity distribution and the diffusive flux. *Journal of Geophysical Research: Earth Surface*, *117*(F3).

Gabitto, J., & Tsouris, C. (2008). Drag coefficient and settling velocity for particles of cylindrical shape. *Powder Technology*, *183*(2), 314-322.

Galloway, T. S., Cole, M., & Lewis, C. (2017). Interactions of microplastic debris throughout the marine ecosystem. *Nature Ecology & Evolution*, *1*(5), 0116.

Gomez, B. (1994). Effects of particle shape and mobility on stable armor development. *Water Resources Research*, *30*(7), 2229-2239.

Goring, D. G., & Nikora, V. I. (2002). Despiking acoustic Doppler velocimeter data. *Journal of Hydraulic Engineering*, *128*(1), 117–126.

Grabowski, R. C., Droppo, I. G., & Wharton, G. (2011). Erodibility of cohesive sediment: The importance of sediment properties. *Earth-science Reviews*, *105*(3), 101-120.

Guo, J. (2002). Logarithmic matching and its applications in computational hydraulics and sediment transport. *Journal of Hydraulic Research*, *40*(5), 555-565.

Haider, A., & Levenspiel, O. (1989). Drag coefficient and terminal velocity of spherical and nonspherical particles. *Powder Technology*, *58*(1), 63-70.

Harris, P. T. (2020). The fate of microplastic in marine sedimentary environments; a review and synthesis. *Marine Pollution Bulletin*, *158*, 111398-111398.

He, B., Smith, M., Egodawatta, P., Ayoko, G. A., Rintoul, L., & Goonetilleke, A. (2021). Dispersal and transport of microplastics in river sediments. *Environmental Pollution*, *279*, 116884.

He, M., & Han, Q. (1982). Stochastic model of incipient sediment motion. *Journal of the Hydraulics Division*, *108*, 211-224.

Heyman, J., Bohorquez, P., & Ancey, C. (2016). Entrainment, motion, and deposition of coarse particles transported by water over a sloping mobile bed. *Journal of Geophysical Research: Earth Surface*, *121*(10), 1931-1952.

Hölzer, A., & Sommerfeld, M. (2008). New simple correlation formula for the drag coefficient of non-spherical particles. *Powder Technology*, *184*(3), 361-365.

Hosseini-Sadabadi, S. A., Radice, A., & Ballio, F. (2019). On reasons of the scatter of literature data for bed-load particle hops. *Water Resources Research*, *55*(2), 1698-1706.

Hu, C., & Hui, Y. (1996). Bed-load transport. I: Mechanical characteristics. *Journal of Hydraulic Engineering*, *122*(5), 245-254.

Hubert, M., & Kalman, H. (2003). Experimental determination of length-dependent saltation velocity in dilute flows. *Powder Technology*, *134*(1), 156-166.

Isachenko, I. (2020). Catching the variety: Obtaining the distribution of terminal velocities of microplastics particles in a stagnant fluid by a stochastic simulation. *Marine Pollution Bulletin*, *159*, 111464.

Julien, P. Y., & Bounvilay, B. (2013). Velocity of rolling bed load particles. *Journal of Hydraulic Engineering*, *139*(2), 177-186.

Kabir, A., Sekine, M., Imai, T., Yamamoto, K., Kanno, A., & Higuchi, T. (2022). Microplastics in the sediments of small-scale Japanese rivers: Abundance and distribution, characterization, sources-to-sink, and ecological risks. *Science of the Total Environment*, *812*, 152590.

Kaiser, D., Estelmann, A., Kowalski, N., Glockzin, M., & Waniek, J. J. (2019). Sinking velocity of sub-millimeter microplastic. *Marine Pollution Bulletin*, *139*, 214-220.

Kaiser, D., Kowalski, N., & Waniek, J. J. (2017). Effects of biofouling on the sinking behavior of microplastics. *Environmental Research Letters*, *12*(12), 124003.

Khatmullina, L., & Isachenko, I. (2017). Settling velocity of microplastic particles of regular shapes. *Marine Pollution Bulletin*, *114*(2), 871-880.

Kirchner, J. W., Dietrich, W. E., Iseya, F., & Ikeda, H. (1990). The variability of critical shear stress, friction angle, and grain protrusion in water-worked sediments. *Sedimentology*, *37*(4), 647-672.

Kowalski, N., Reichardt, A. M., & Waniek, J. J. (2016). Sinking rates of microplastics and potential implications of their alteration by physical, biological, and chemical factors. *Marine Pollution Bulletin*, *109*(1), 310-319.

Lajeunesse, E., Malverti, L., & Charru, F. (2010). Bed load transport in turbulent flow at the grain scale: Experiments and modeling. *Journal of Geophysical Research: Earth Surface*, *115*(F4).

Lee, H., & Hsu, I.-S. (1994). Investigation of saltating particle motions. *Journal of Hydraulic Engineering*, *120*(7), 831-845.

Liro, M., Emmerik, V. T., Wyzga, B., Liro, J., & Mikuś, P. (2020). Macroplastic storage and remobilization in rivers. *Water*, *12*(7), 2055.

Liu, M., Pelosi, A., & Guala, M. (2019). A statistical description of particle motion and rest regimes in open-channel flows under low bedload transport. *Journal of Geophysical Research: Earth Surface*, *124*(11), 2666-2688.

Maheswaran, B., Karmegam, N., Al-Ansari, M., Subbaiya, R., Al-Humaid, L., Sebastin Raj, J., & Govarthanan, M. (2022). Assessment, characterization, and quantification of microplastics from river sediments. *Chemosphere*, *298*, 134268-134268.

Marsh, N. A., Western, A. W., & Grayson, R. B. (2004). Comparison of methods for predicting incipient motion for sand beds. *Journal of Hydraulic Engineering*, *130*(7), 616-621.

Martin, R. L., Jerolmack, D. J., & Schumer, R. (2012). The physical basis for anomalous diffusion in bed load transport. *Journal of Geophysical Research: Earth Surface*, *117*(F1), F01018.

McCarron, C. J., Van Landeghem, K. J. J., Baas, J. H., Amoudry, L. O., & Malarkey, J. (2019). The hiding-exposure effect revisited; a method to calculate the mobility of bimodal sediment mixtures. *Marine Geology*, *410*, 22-31.

Meijer, L. J., Van Emmerik, T., Van Der Ent, R., Schmidt, C., & Lebreton, L. (2021). More than 1000 rivers account for 80% of global riverine plastic emissions into the ocean. *Science Advances*, *7*(18), eaaz5803.

Mennekes, D., & Nowack, B. (2023). Predicting microplastic masses in river networks with high spatial resolution at country level. *Nature Water*, *1*(6), 523-533.

Morét-Ferguson, S., Law, K. L., Proskurowski, G., Murphy, E. K., Peacock, E. E., & Reddy, C. M. (2010). The size, mass, and composition of plastic debris in the western North Atlantic Ocean. *Marine Pollution Bulletin*, *60*(10), 1873-1878.

Nava, V., Chandra, S., Aherne, J., Alfonso, M. B., Antão-Geraldes, A. M., Attermeyer, K., Bao, R., Bartrons, M., Berger, S. A., Biernaczyk, M., Bissen, R., Brookes, J. D., Brown, D., Cañedo-Argüelles, M., Canle, M., Capelli, C., Carballeira, R., Cereijo, J. L., Chawchai, S., . . . Leoni, B. (2023). Plastic debris in lakes and reservoirs. *Nature*, *619*(7969), 317-322.

Nikora, V., Habersack, H., Huber, T., & McEwan, I. (2002). On bed particle diffusion in gravel bed flows under weak bed load transport. *Water resources research*, *38*(6), 17-11-17-19.

Niño, Y., & García, M. (1998). Experiments on saltation of sand in water. *Journal of Hydraulic Engineering*, *124*(10), 1014-1025.

Ninto, Y., & Garcia, M. H. (1996). Experiments on particle—turbulence interactions in the near–wall region of an open channel flow: implications for sediment transport. *Journal of Fluid Mechanics*, *326*, 285-319.

Oh, J., & Tsai, C. W. (2010). A stochastic jump diffusion particle-tracking model (SJD-PTM) for sediment transport in open channel flows. *Water Resources Research*, *46*(10).

Padervand, M., Lichtfouse, E., Robert, D., & Wang, C. (2020). Removal of microplastics from the environment. A review. *Environmental Chemistry Letters*, *18*(3), 807-828.

Paintal, A. S. (1971). A stochastic model of bed load transport. *Journal of Hydraulic Research*, *9*(4), 527-554.

Paphitis, D. (2001). Sediment movement under unidirectional flows: an assessment of empirical threshold curves. *Coastal Engineering*, *43*(3), 227-245.

Pope, S. B. (2000). *Turbulent flows*. Cambridge University Press.

Rabinovich, E., & Kalman, H. (2009). Incipient motion of individual particles in horizontal particle–fluid systems: A. Experimental analysis. *Powder Technology*, *192*(3), 318-325.

Ranieri, G. (2008). Fall velocities of natural sediment particles: a simple mathematical presentation of the fall velocity. *Journal of Hydraulic Research*, *46*(sup1), 168-174.

Rao, A., & Kumar, B. (2009). Analytical Formulation of the Correction Factor Applied in Einstein and Barbarossa Equation (1952). *Journal of Hydrology and Hydromechanics*, *57*(1), 40-44.

Roseberry, J. C., Schmeeckle, M. W., & Furbish, D. J. (2012). A probabilistic description of the bed load sediment flux: 2. Particle activity and motions. *Journal of Geophysical Research*, *117*, F03032.

Saxby, J., Beckett, F., Cashman, K., Rust, A., & Tennant, E. (2018). The impact of particle shape on fall velocity: Implications for volcanic ash dispersion modelling. *Journal of Volcanology and Geothermal Research*, *362*, 32-48.

Schell, T., Rico, A., & Vighi, M. (2020). Occurrence, fate and fluxes of plastics and microplastics in terrestrial and freshwater ecosystems. In P. de Voogt (Ed.), *Reviews of environmental contamination and toxicology volume 250* (pp. 1-43). Springer International Publishing.

Schneider, C. A., Rasband, W. S., & Eliceiri, K. W. (2012). NIH Image to ImageJ: 25 years of image analysis. *Nature Methods*, *9*(7), 671-675.

Seizilles, G., Lajeunesse, E., Devauchelle, O., & Bak, M. (2014). Cross-stream diffusion in bedload transport. *Physics of Fluids*, *26*(1), 13302.

Shen, L., & Worrell, E. (2024). Plastic recycling. In *Handbook of recycling* (pp. 497-510). Elsevier.

Shim, J., & Duan, J. (2019). Experimental and theoretical study of bed load particle velocity. *Journal of Hydraulic Research*, *57*(1), 62-74.

Shim, J., & Duan, J. G. (2017). Experimental study of bed-load transport using particle motion tracking. *International Journal of Sediment Research*, *32*(1), 73-81.

Shortis, M. (2015). Calibration techniques for accurate measurements by underwater camera systems. *Sensors*, *15*(12), 30810-30826.

Shvidchenko, A. B., Pender, G., & Hoey, T. B. (2001). Critical shear stress for incipient motion of sand/gravel streambeds. *Water Resources Research*, *37*(8), 2273-2283.

Simoes, F. J. M. (2014). Shear velocity criterion for incipient motion of sediment. *Water Science and Engineering*, *7*(2), 183-193.

Smith, M., Love, D. C., Rochman, C. M., & Neff, R. A. (2018). Microplastics in seafood and the implications for human health. *Current Environmental Health Reports*, *5*, 375-386.

Song, X., Xu, Z., Li, G., Pang, Z., & Zhu, Z. (2017). A new model for predicting drag coefficient and settling velocity of spherical and non-spherical particle in Newtonian fluid. *Powder Technology*, *321*, 242-250.

Song, Z., Wu, T., Xu, F., & Li, R. (2008). A simple formula for predicting settling velocity of sediment particles. *Water Science and Engineering*, *1*(1), 37-43.

Strokal, M., Vriend, P., Bak, M. P., Kroeze, C., van Wijnen, J., & van Emmerik, T. (2023). River export of macro- and microplastics to seas by sources worldwide. *Nature Communications*, *14*(1), 4842.

Sutkar, P. R., Gadewar, R. D., & Dhulap, V. P. (2023). Recent trends in degradation of microplastics in the environment: A state-of-the-art review. *Journal of Hazardous Materials Advances*, *11*, 100343.

Thompson, C. E. L., Amos, C. L., Jones, T. E. R., & Chaplin, J. (2003). The manifestation of fluid-transmitted bed shear stress in a smooth annular flume-a comparison of methods. *Journal of Coastal Research*, *19*(4), 1094-1103.

Thompson, R. C. (2015). Microplastics in the marine environment: Sources, consequences and solutions. In M. Bergmann, L. Gutow, & M. Klages (Eds.), *Marine anthropogenic litter* (pp. 185-200). Springer International Publishing.

Tinevez, J. Y., Perry, N., Schindelin, J., Hoopes, G. M., Reynolds, G. D., Laplantine, E., Bednarek, S. Y., Shorte, S. L., & Eliceiri, K. W. (2017). TrackMate: An open and extensible platform for single-particle tracking. *Methods*, *115*, 80-90.

Tramoy, R., Gasperi, J., Colasse, L., & Tassin, B. (2020). Transfer dynamic of macroplastics in estuaries — New insights from the Seine estuary: Part 1. Long term dynamic based on date-prints on stranded debris. *Marine Pollution Bulletin*, *152*, 110894.

Uhlmann, M., & Doychev, T. (2014). Sedimentation of a dilute suspension of rigid spheres at intermediate Galileo numbers: the effect of clustering upon the particle motion. *Journal of Fluid Mechanics*, *752*, 310-348.

Van Melkebeke, M., Janssen, C., & De Meester, S. (2020). Characteristics and sinking behavior of typical microplastics including the potential effect of biofouling: implications for remediation. *Environmental Science & Technology*, *54*(14), 8668-8680.

Vidal, F., van der Marel, E. R., Kerr, R. W. F., McElroy, C., Schroeder, N., Mitchell, C., Rosetto, G., Chen, T. T. D., Bailey, R. M., Hepburn, C., Redgwell, C., & Williams, C. K. (2024). Designing a circular carbon and plastics economy for a sustainable future. *Nature*, *626*(7997), 45-57.

Waldschläger, K., Brückner, M. Z. M., Carney Almroth, B., Hackney, C. R., Adyel, T. M., Alimi, O. S., Belontz, S. L., Cowger, W., Doyle, D., Gray, A., Kane, I., Kooi, M., Kramer, M., Lechthaler, S., Michie, L., Nordam, T., Pohl, F., Russell, C., Thit, A., . . . Wu, N. (2022). Learning from natural sediments to tackle microplastics challenges: A multidisciplinary perspective. *Earth-science Reviews*, *228*, 104021.

Waldschläger, K., & Schüttrumpf, H. (2019a). Effects of particle properties on the settling and rise velocities of microplastics in freshwater under laboratory conditions. *Environmental Science & Technology*, *53*(4), 1958-1966.

Waldschläger, K., & Schüttrumpf, H. (2019b). Erosion Behavior of Different Microplastic Particles in Comparison to Natural Sediments. *Environment Science & Technology*, *53*(22), 13219-13227.

Wang, X., Ye, C., Wang, B., & Yan, X. (2016). Experimental study on velocity profiles with different roughness elements in a flume. *Acta Geophysica*, *63*(6), 1685-1705.

Wang, Y., Zhou, L., Wu, Y., & Yang, Q. (2018). New simple correlation formula for the drag coefficient of calcareous sand particles of highly irregular shape. *Powder Technology*, *326*, 379-392.

Wang, Z., Dou, M., Ren, P., Sun, B., Jia, R., & Zhou, Y. (2021). Settling velocity of irregularly shaped microplastics under steady and dynamic flow conditions. *Environmental Science and Pollution Research*, *28*(44), 62116-62132.

Wilcock, P. R. (1988). Methods for estimating the critical shear stress of individual fractions in mixed-size sediment. *Water Resources Research*, *24*, 1127-1135.

Wilcock, P. R. (1993). Critical shear stress of natural sediments. *Journal of Hydraulic Engineering*, *119*, 491-505.

Wilcock, P. R., & Crowe, J. C. (2003). Surface-based transport model for mixed-size sediment. *Journal of Hydraulic Engineering*, *129*(2), 120-128.

Wu, F., & Chou, Y. (2003). Rolling and lifting probabilities for sediment entrainment. *Journal of Hydraulic Engineering*, *129*(2), 110-119.

Wu, P., Huang, J., Zheng, Y., Yang, Y., Zhang, Y., He, F., Chen, H., Quan, G., Yan, J., Li, T., & Gao, B. (2019). Environmental occurrences, fate, and impacts of microplastics. *Ecotoxicology and Environmental Safety*, *184*, 109612.

Wu, Z., Furbish, D., & Foufoula-Georgiou, E. (2020). Generalization of hop distance-time scaling and particle velocity distributions via a two-regime formalism of bedload particle motions. *Water Resources Research*, *56*(1), e2019WR025116.

Wu, Z., Singh, A., Foufoula-Georgiou, E., Guala, M., Fu, X., & Wang, G. (2021). A velocity-variation-based formulation for bedload particle hops in rivers. *Journal of Fluid Mechanics*, *912*, A33.

Xu, H., Lu, J., & Liu, X. (2008). Non-uniform sediment incipient velocity. *International Journal of Sediment Research*, *23*(1), 69-75.

Yang, F., Liu, X., Yang, K., & Cao, S. (2009). Study on the angle of repose of nonuniform sediment. *Journal of Hydrodynamics*, *21*(5), 685-691.

Yang, G., Yu, Z., Baki, A. B. M., Yao, W., Ross, M., Chi, W., & Zhang, W. (2023). Settling behaviors of microplastic disks in water. *Marine Pollution Bulletin*, *188*, 114657.

Yang, L., Zhang, Y., Kang, S., Wang, Z., & Wu, C. (2021). Microplastics in freshwater sediment: A review on methods, occurrence, and sources. *Science of the Total Environment*, *754*, 141948.

Yang, Y., Gao, S., Wang, Y. P., Jia, J., Xiong, J., & Zhou, L. (2019). Revisiting the problem of sediment motion threshold. *Continental Shelf Research*, *187*, 103960.

Yu, Z., Loewen, M., Guo, S., Guo, Z., & Zhang, W. (2023). Investigation of the sheltering effects on the mobilization of microplastics in open-channel flow. *Environmental Science & Technology*, *57*(30), 11259-11266.

Yu, Z., Yang, G., & Zhang, W. (2022). A new model for the terminal settling velocity of microplastics. *Marine Pollution Bulletin*, *176*, 113449.

Yu, Z., Yao, W., Loewen, M., Li, X., & Zhang, W. (2022). Incipient motion of exposed microplastics in an open-channel flow. *Environmental Science & Technology*, *56*(20), 14498-14506.

Zhang, H. (2017). Transport of microplastics in coastal seas. *Estuarine, Coastal and Shelf Science*, *199*, 74-86.

Zhang, L., Liu, J., Xie, Y., Zhong, S., Yang, B., Lu, D., & Zhong, Q. (2020). Distribution of microplastics in surface water and sediments of Qin river in Beibu Gulf, China. *Science of the Total Environment*, *708*, 135176.

Zhou, Y., Yao, X., Gu, Y., Qian, D., Tang, Y., Zhang, Y., Zhu, D. Z., & Zhang, T. (2020). Biological effects on incipient motion behavior of sediments with different organic matter content. *Journal of Soils and Sediments*, *21*(1), 627-640.

Zhu, J., Zhang, Q., Li, Y., Tan, S., Kang, Z., Yu, X., Lan, W., Cai, L., Wang, J., & Shi, H. (2019). Microplastic pollution in the Maowei Sea, a typical mariculture bay of China. *Science of the Total Environment*, *658*, 62-68.

Zhu, X., Zeng, Y. H., & Huai, W. X. (2017). Settling velocity of non-spherical hydrochorous seeds. *Advances in Water Resources*, *103*, 99-107.

Appendices

A. A new model for the terminal settling velocity of microplastics

Table A-1 Summary of formulas for the drag coefficient (C_d).

Study	Eq.	Particles	Shape	Re_p range
Clift and Gauvin (1971)	(2-4)	/	$\Phi = 1.00$	Entire range
Song et al. (2008) & Chubarenko et al. (2016)	(2-5)	Sediments, MPs	$\Phi \approx 1.00$	$< 2 \times 10^5$
Cheng (2009)	(2-7)	/	$\Phi = 1.00$	$< 2 \times 10^5$
Alcerreca et al. (2012)	(2-10)	Sediments	$CSF = 0.11$ to 0.98	$0.30 \sim 454.30$
Song et al. (2017)	(2-8)	/	$\Phi = 0.47 \sim 1.00$	$10^{-3} \sim 10^2$
Waldschläger & Schüt rumpf (2019)	(2-9)	MPs	Pellets, fragments, fibers	/
This study	(2-16)	MPs	Spherical & non-spherical particles	$1 \sim 10^3$

Table A-2 Raw data for this study.

Source	Particle materials	Shape	Data points	$(\rho_s-\rho_f)/\rho$	*CSF*	*Φ*
Kowalski et al. (2016)	PS	Pellet	5	0.02~0.06	1.00	1.00
	PS	Cylinder	26	0.03~0.05	0.35	0.48
	PA	Nodular	62	0.11~0.14	0.49	0.52
	PMMA	Angular	73	0.16~0.19	0.60	0.60
	PET	Angular	75	0.35~0.39	0.34	0.40
	POM	Angular	68	0.38~0.42	0.11	0.23
	PVC	Nodular	54	0.52~0.56	0.34	0.36
Khatmullina & Isachenko (2017)	PCL	Pellet	37	0.13	0.95	1.00
	PCL	Cylinder	294*	0.13	0.92	\
	Nylon, FC & PE	Fiber	241	0.13~0.19	0.16~0.99	0.09~0.99
Waldschläger & Schüt rumpf (2019)	PET	Pellet, fragment, sphere & fiber	19*	\	\	\
	PVC	Pellet, fragment, sphere & fiber	16*	\	\	\
	PS	Pellet, fragment, sphere & fiber	12*	\	\	\
Van Melkebeke et al. (2020)	PET	Fragment	20	0.37	0.07~0.83	0.29~0.98
	PS	Fragment	20	0.05	0.04~0.11	0.30~0.59
	PVC	Fiber	18	0.43	0.02~0.16	0.21~0.66
	PE	Film	40*	0.20~0.28	0.01~0.06	0.06~0.37
Wang et al. (2021)	PS	Pellet	95*	0.04~0.12	\	1.00
Francalanci et al. (2021)	PVC	Pellet	38*	0.08~0.25	0.15~1.00	\
	PET	Pellet, fragment	70*	0.10~0.37	0.02~0.98	\
	ABS	Pellet	30*	0.04	0.59~0.81	\
	PS	Pellet	30*	0.03~0.04	0.42~0.95	\

Notes: PVC – polyvinyl chloride; PS – polystyrene; PA – polyamide; PMMA – polymethyl methacrylate; PET – polyethylene terephthalate; POM – polyoxymethylene; PCL – polycaprolactone; PE – polyethylene; FC – fluorocarbon.

* Data points were included in Fig. 2-1, but not used for developing the new C_d formula and w_s model in this study.

Table A-3 *P*-values and variance inflation factors (*VIF*) of the introduced variables (*CSF* and *Φ*) in the new C_d formula.

Variable	*P*-value	*VIF*
CSF	0.000	2.38
Φ	0.030	2.13

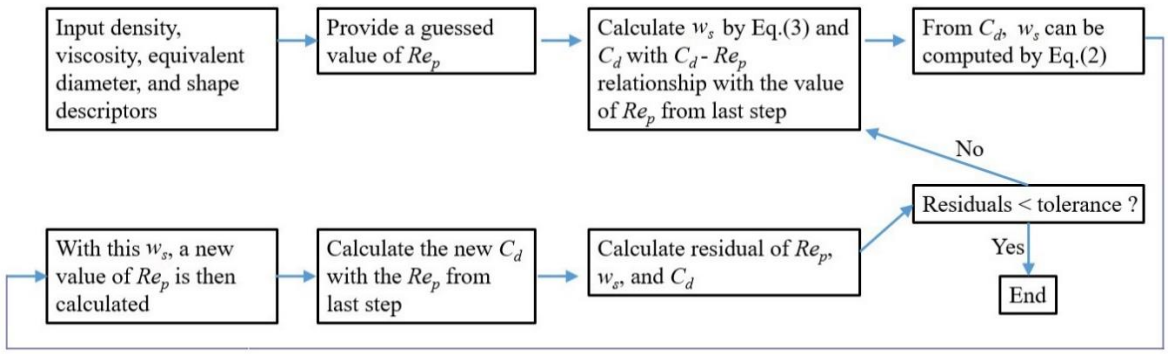

Figure A-1 Flow chart of the trial procedure for the calculation of Re_p, C_d, and w_s for MPs.

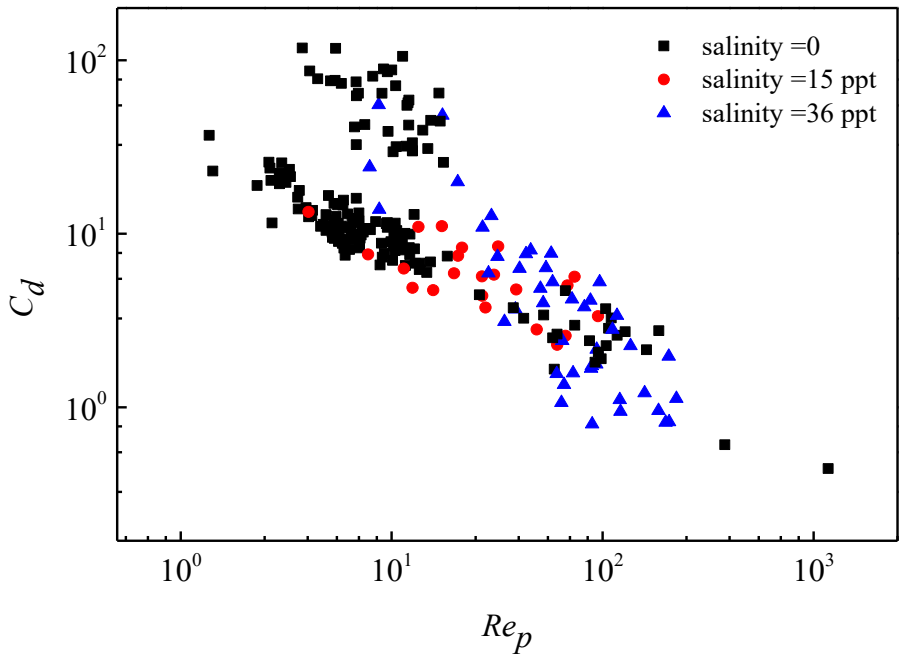

Figure A-2 The Re_p - C_d relationship for MPs settling in fluids of different salinities.

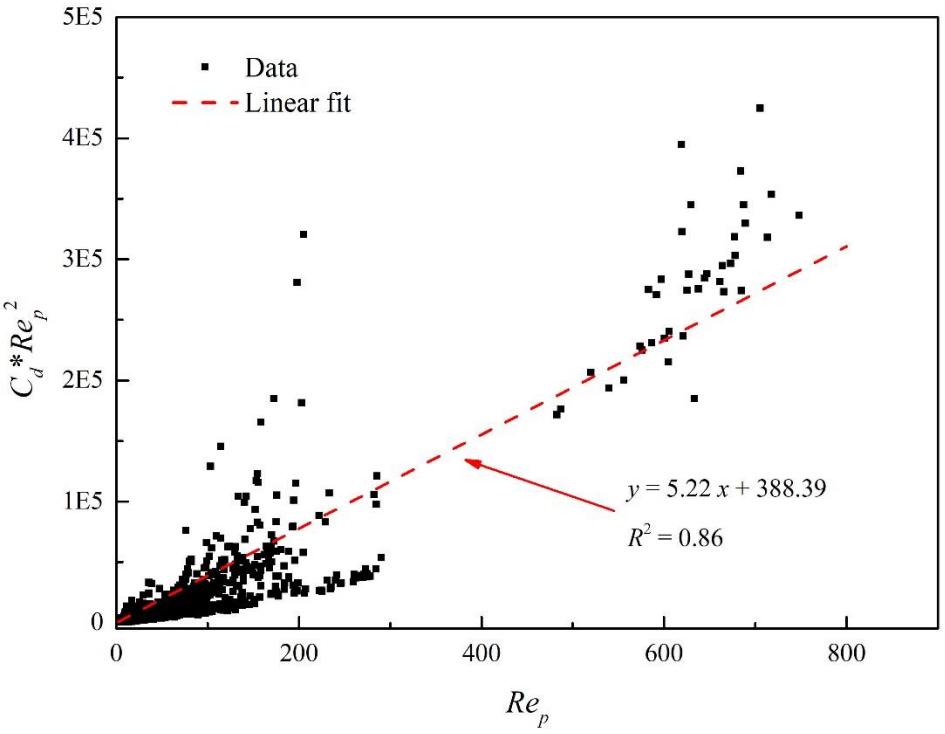

Figure A-3 The dependence of $C_dRe_p^2$ on Re_p. The black dots are 1,343 experimental data points of MPs filtered from the studies listed in Table A2. The red line is the linear approximation of all the data points with $R^2 = 0.86$.

B. The incipient motion of exposed microplastics in open-channel flow

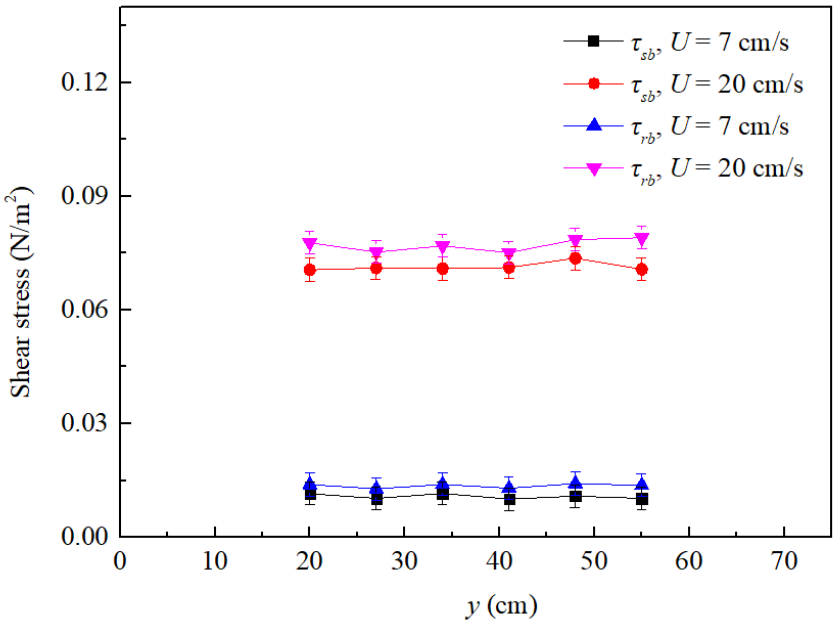

Figure B-1 Later distribution of shear stress along the width of the experimental area.

Table B-1 Regression statistics for U_i on the dependence of *CSF* for MPs. *P-values* < 0.05 indicate statistical significance.

MP materials	Bed condition	*P-value*
ABS	Smooth	2.03E-06
PC	Smooth	0.02
PMMA	Smooth	7.11E-06
PA	Smooth	1.21E-4
PVC	Smooth	3.06E-11
POM	Smooth	3.41E-05
PET	Smooth	6.71E-06
ABS	Rough	0.001
PC	Rough	0.131
PMMA	Rough	5.92E-06
PA	Rough	2.59E-05

PVC	Rough	1.94E-13
POM	Rough	1.77E-05
PET	Rough	2.93E-05

Table B-2 Regression statistics for Λ_c on the dependence of MP properties (D_n, *CSF*, and $\Delta\rho/\rho$) based on the data collected from both the present study and Waldschläger and Schüttrumpf (2019b). *P-values* < 0.05 indicate statistical significance. *VIF* quantifies the variance degree of the inflated parameters in a regression model. *VIF* value > 4 indicates that two or more parameters are correlated and no less than one of them is superfluous.

	D_n	*CSF*	$\Delta\rho/\rho$
P-value	0.01	0.02	3.94E-6
VIF	1.46	1.11	1.34

Table B-3 Fitted parameters for β_1 and β_2 and their lower and upper 95% confidence intervals for the proposed Λ_c formula.

Parameter	Value	Lower 95%confidence interval	Upper 95%confidence interval
β_1	-0.028	-0.037	-0.019
β_2	-0.126	-0.142	-0.110